Fall 2020

# Development of TI-DFTB: Transition Dipole Moment Calculations in a Time-Independent Density Functional Tight-Binding Framework

Megan Deshaye
*Western Washington University*, deshaye@wisc.edu

DEVELOPMENT OF TI-DFTB

TRANSITION DIPOLE MOMENT CALCULATIONS IN A TIME-INDEPENDENT

DENSITY FUNCTIONAL TIGHT-BINDING FRAMEWORK
By

MEGAN YVONNE DESHAYE

Accepted in Partial Completion
of the Requirements for the Degree
Master of Science

ADVISORY COMMITTEE

Dr. Tim Kowalczyk, Chair

Dr. Robert Berger

Dr. Elizabeth Raymond

WESTERN WASHINGTON UNIVERSITY
Graduate School

Dr. David Patrick, Dean

## MASTER'S THESIS

In presenting this thesis in partial fulfillment of the requirements for a master's degree at Western Washington University, I grant to Western Washington University the non-exclusive royalty-free right to archive, reproduce, distribute, and display the thesis in any and all forms, including electronic format, via any digital library mechanisms maintained by WWU.

I represent and warrant this is my original work, and does not infringe or violate any rights of others. I warrant that I have obtained written permissions from the owner of any third party copyrighted material included in these files.

I acknowledge that I retain ownership rights to the copyright of this work, including but not limited to the right to use all or part of this work in future works, such as articles or books.

Library users are granted permission for individual, research and non-commercial reproduction of this work for educational purposes only. Any further digital posting of this document requires specific permission from the author.

Any copying or publication of this thesis for commercial purposes, or for financial gain, is not allowed without my written permission.

Megan Yvonne Deshaye

Fall 2020

DEVELOPMENT OF TI-DFTB

TRANSITION DIPOLE MOMENT CALCULATIONS IN A TIME-INDEPENDENT

DENSITY FUNCTIONAL TIGHT-BINDING FRAMEWORK

A Thesis
Presented to
The Faculty of
Western Washington University

In Partial Fulfillment
Of the Requirements for the Degree
Master of Science

By
Megan Yvonne Deshaye
Fall 2020

## ABSTRACT

Here we discuss the development of a time-independent excited state computational method that consists of three augmentations to the semi-empirical electronic structure package, DFTB+ 19.1. The density functional based tight binding method (DFTB) is an approximation of Kohn-Sham (KS) density functional theory (DFT) wherein the energy functional is expanded to second order with respect to density fluctuations. Application of a $\Delta$ self-consistent field ($\Delta$SCF) approach within DFTB has allowed for the variationally optimized calculation of spin-purified excited state (ES) properties, and forms the foundation of our time-independent DFTB (TI-DFTB) framework. Selection of KS spin orbitals based on the character of the ES, and subsequent relaxation of these orbitals under non-Aufbau occupation constraints for both the singlet and triplet configuration is followed by application of the Ziegler sum rule to determine the time-independent spin purified ES of the system, its energy, and its optimized geometry. The maximum overlap method is an algorithmic restructuring of the typical DFTB variational charge optimization pathway, allowing differential relaxation pathways for difficult to converge molecules. Three variations of this approach have been implemented in DFTB+ 19.1, and are compatible with the time-independent ES method. The ground and excited electronic states resulting from a TI-DFTB calculation are made mutually orthogonal by a corresponding orbital transformation, thereby allowing calculation of transition properties like the transition dipole moment (TDM). Together these methods form a robust computational platform to investigate ES and transition information about chemical systems at low computational cost.

# ACKNOWLEDGMENT

# TABLE OF CONTENTS

# LIST OF TABLES

# LIST OF FIGURES

## Dedication

This thesis is dedicated to The Little Red Hen.

# Chapter One

# INTRODUCTION

## 1.1   The Climate Crisis

Global temperatures have risen in the last hundred years due in part to the burning of fossil fuels. The unearthing and burning of long hydrocarbon chains pollutes the atmosphere with low energy gas particles termed greenhouse gases, so named because these particles trap infrared radiation near the earth's crust. When infrared radiation is not allowed to exit the atmosphere, global temperatures rise.[1,2] This has resulted in and continues to perpetuate rising sea levels, diminished polar ice caps, reduced air quality, and receding terrestrial ecosystems.[3–5] The rising temperature affects many large scale ecological systems that directly affect human beings as well, including but not limited to crop failure, increased populations of disease spreading insects, hurricanes, forest fires, drought, and flooding.[6–8]

The climate dilemma has ushered in an era of policy making that seeks to limit large scale sources of atmospheric pollution, such as so called "carbon taxes." However, the perceived economic burden of these policies by both the private sector and the general public has led to a disbelief in this crisis.[9,10] Misinformation regarding climate change is a powerful weapon in the hands of politicians and corporate lobbyists, therefore a pervasive ignorance regarding this crisis has become rampant. Climate change is the core motivation for this work, therefore it is strongly suggested that the information and references provided above

are understood fully before proceeding.

Climate change has demanded technological progress in energy production that does not rely on carbon based fuel sources. Wind turbines and hydroelectric dams harness the kinetic energy of wind and water, and "bio-fuels" refine combustibles from agricultural staples like corn to reduce the need for deep oil drilling. Solar alternatives are an attractive replacement to fossil fuels as these materials and interfaces harness the radiative energy of the sun to induce excited states within an atomistic framework, releasing this useful energy without the harmful gases that are a byproduct of burning fuel.[11]

Photoactive materials are a significant area of investigation in the chemical sciences where photothermal, photocatalytic and photovoltaic pathways are considered. Notable advances have been made in organic photovoltaics, which when photoexcited by the sun release energy in the form of an electric current.[12–17] Sensitization of solar cells with organic dyes have increased the efficiency of these systems, allowing for broader absorption ranges.[18] Preservation of a fraction of the excitation energy from photoadsorption is exemplified by solar thermal fuels which photoisomerize to a higher energy conformation allowing for energy storage, and the subsequent relaxation of this excited state allows for the transformation of solar energy to useful thermal, chemical, or electrical work.[19–21] These are but a few examples of the burgeoning world of photochemistry and its relationship to clean energy alternatives.

## 1.2  The Role of Computation

The aforementioned solar devices depend on photon driven electron excitation within some photoactive chromophores. Absorption of a photon can promote an electron from a valence orbital to a virtual orbital as shown in Figure 1.1, and a quantum of energy is released upon relaxation back to the ground state. Depending on convention, the highest energy electron(s) in the ground state ($S_0$) valence orbitals occupy an energetic state called the highest occupied molecular orbital (HOMO) in organic compounds or the valence band in

semiconductors. The first excited state ($S_1$) often occupies a virtual orbital referred to as the lowest unoccupied molecular orbital (LUMO) in organic compounds or conduction band in semiconductors. The gap between these orbital energies is termed the HOMO-LUMO gap for organics, and the band gap for semiconductors. Vocabulary will adjust depending on the application, and the general ground state (GS) and excited state (ES) verbiage will be used when discussing computational methods.

The difference in energy between the highest energy valence orbital and the lowest energy virtual orbital determines the propensity of a molecular candidate to exhibit strong solar properties. This property in conjunction with the quantum yield is of great interest to experimentalists when designing materials for it is directly responsible for the efficiency of the photoactive device.[22,23] Furthermore, detailed understanding of the transition state of these materials can elucidate the energetic barrier for relaxation on the ES potential energy surface, and the energetic barrier for photoexcitation.[24] These properties are therefore highly important for solar applications and though are often simple enough to test experimentally
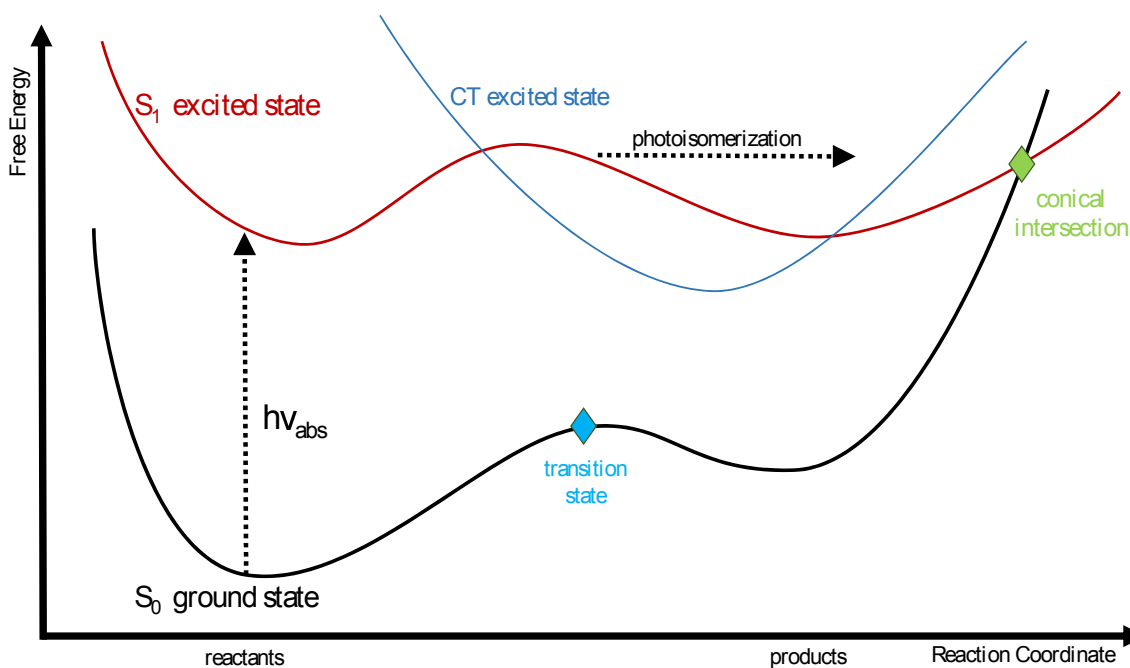


**Figure 1.1** Representative ground and excited-state potential energy surfaces of a typical organic chromophore.

3

after synthesis, it is computationally expensive to test theoretically.

Investigation into accessible computational methods capable of describing the excited-state (ES) potential energy surface in prospective solar materials is therefore highly justified, and an efficient and cost effective excited state electronic structure calculation method is in high demand.[25–27] Data driven materials vetting is made possible through a marrying of electronic structure theory and high throughput (HT) screening as is exemplified by the field of cheminformatics and its foundation in drug discovery.[28] These processes typically rely on classical methods (see section 2.2) or first principles based ground-state methods (see section 3.1) which can be used to predict ES descriptors given a proper functional (see subsection 3.1.1). However, these methods do not typically describe the ES potential energy surface nor do they correctly predict nonadiabatic electronic transitions which are imperative to predict excited state lifetimes, exciton diffusion, and electron mobility.

Computational methods for ES potential energy surface description currently exist, but are rarely used for screening molecular candidates before synthesis due to both the time and resource intensity of such calculations. Wavefunction based methods (see subsection 2.3.2) are often used for high accuracy virtual space description due to the exhaustively multireference nature of the methods. These levels of theory would not be a reasonable choice in a HT scenario due to their computational cost, or more specifically the high level of scaling. Perturbation based methods offer well defined ES potential energy surface but are again limited by computational cost in the light of HT photochemical screening. For example, time-dependent density functional theory (TD-DFT) is among the most popular methods for excited state calculations due to its relative efficiency,[29] but this method scales as $\mathcal{O}(N^3)$, or in a cubic manner with respect to number of molecular orbitals (MO). Additionally, this strategy breaks down near conical intersections therefore making its description of photochemistry questionable.[30–32] This is specifically limiting for photovoltaic applications,[33] where one would do better to use a higher level of theory and avoid this oversight, undermining HT screening efforts.

As it currently stands, in order to describe a compound with the accuracy required to derive multistate characteristics one incurs prohibitively long calculation times, not to mention the surrounding barriers of software paywalls, overly technical user interfaces, and overwhelming processing needs. There is therefore a division between experimentalists and computational predictions that relate to their work, and the current solution rests in collaboration between experimentalists and theorists who can incur heavier computational burdens. The purpose of this manuscript is to outline an electronic structure alternative that bridges the gap between experimentalists and photophysical descriptors that can expedite molecular design in the field of photochemistry.

## 1.3   TI-DFTB

Density functional tight-binding (DFTB, see section 3.2) is an approximation of full density functional theory (DFT, see section 3.1) that allows for fast ground-state calculations due to parameterization and a sparse matrix implementation.[34,35] Into this method hosted in DFTB+, and open source codebase,[36] we have integrated time-independent excited state capabilities modeled after $\Delta$SCF.[37] In this method the ES potential energy surface is approximated and self-consistently optimized under non-Aufbau orbital occupation constraints.[38] This allows for relaxation of the ES potential energy surface, and offers post calculation transition dipole moment definition. This value is theoretically related to photophysical relaxation pathways and can be used to determine ES lifetimes. This novel ES method is useful for structures in the hundreds of atoms, and can provide a platform for HT screening of organic chromophores. This method is desktop compatible due to low memory requirements, fast due to parameterization of the theoretical approach, and accessible to experimentalists due to its easy input structure and open sourced packaging.

## 1.4  Outline

The method developed in this thesis and described in the following text has the ability to fill a gap by providing fast approximate excited and transition state information, providing accessible molecular screening to scientists on the forefront of this developing field.

Other methods available to the public to study molecular candidates are described in detail in chapter 2. In this section the strengths and weaknesses of the main modern computational methods are discussed to paint a fairly comprehensive picture of the spectrum where our method falls. Density functional theory, and the tight-binding approximation DFTB are described in detail in chapter 3. In chapter 4, the theory and implementation of TI-DFTB and several convergence options within the method are discussed. Within chapter 5 there is a proof and description of the implementation of transition dipole moment calculations within a TI-DFTB framework. A proof of concept of the final TI-DFTB framework, including ES and state-transition information against higher levels of theory is described in chapter 6, and in chapter 7 we discuss the implications of our findings.

# Chapter Two

# AN OVERVIEW OF COMPUTATIONAL CHEMISTRY

## 2.1    A Brief Orientation

The 20th century houses both the conception and boom of modern computational chemistry. In the 20's and 30's quantum mechanical calculations were first applied to chemical systems, a movement pioneered by people including Linus Pauling. The 40's saw the development of the first electronic computers, replacing forever the old mechanical models. The first quantum mechanical calculations performed on computers were executed in the 50's, followed by the development of a hierarchy of quantum chemical methods in the 60's and 70's. Kohn and Pople introduced the first electronic structure methods, propelling this fledgling enterprise into the 21st century where the range of computational chemistry models have exploded into the active corner of modern chemistry it is today.

Although to an unwitting consumer modern computers seem limitless in their performance, a computational chemist understands the inevitability that certain trade-offs must be expected and carefully considered. Computational chemistry is as any system: a delicate dance of give and take where the more fully you wish to describe your model correlates to an increased level of toil on the part of the scientist, or more accurately, the technological

resources she has access to. As the size of a system one wishes to consider increases, so does the computational expense in describing that system rigorously - therefore many of the approaches to methods development in recent times have introduced approximations to a full physical treatment that allow reasonably accurate predictions to be made about many-electron systems. A purist - or perhaps a recent physical chemistry student - might balk at this news, but fear not, the Shrödinger equation was in fact useful information to absorb and tediously derive, however if this perfectly exact treatment of a physical system cannot be extended to a helium atom how is one to use it to describe a kinase, or a solar device?

Understanding the spectrum of computational feasibility and level of physical description one is left on a seesaw teetering between full quantum mechanical and classical descriptions of particles deciding where the fulcrum of each system lies. This metaphorical playground toy is delineated into categories: *ab ibitio*, semi-empirical, and classical. *Ab initio* methods include Hartree-Fock (HF), post Hartree-Fock, and density functional theory (DFT). These electronic structure methods explicitly treat all or most electronic degrees of freedom and offer the highest amount of physical detail with the highest computational cost. Semi-empirical methods like Hückel, extended Hückel, and density functional tight binding (DFTB) expedite the description of electronic systems using experimentally determined constants termed parameters. This parameterization increases the speed of a calculation while making assumptions about the system, introducing error but allowing the extension of these methods to electron populations in the hundreds. Classical methods step away from remodeling the Schrödinger equation altogether, instead employing force fields and continuum models to accomplish calculations of thousands of electrons. These classical methods are grouped into subcategories like molecular mechanics, molecular dynamics, course-grained models and more. Truthfully they have very little to do with the crux of this work, however they will be described with care for the benefit of the reader, and to describe where TI-DFTB fits into the zoo of computational methods.

## 2.1.1 In Practice

The first thing any computational chemist must understand is how to describe a system to their computer and what they hope the computer will return, fundamental ideas termed respectively the molecular geometry and the potential energy surface (PES).

**Input: The Molecular Geometry**

The molecular geometry is simply the identity and position of each atom in a system. An example structure of this is a Cartesian coordinate xyz structure where each nucleus is assigned a three coordinate location in space. Applying this to a model, water ($H_2O$) has 9 Cartesian coordinates. For all non-linear molecules the number of degrees of freedom can be calculated by the simple arithmetic $3N - 6$ (and $3N - 5$ for linear molecules) where $N$ is the number of atoms, therefore water possesses three intrinsic degrees of freedom - each $O - H$ bond-length and the $H - O - H$ bond angle. Using information about the degrees of freedom of a system allows you to create a second form of input called a Z-matrix where the columns correspond to the bond-length, bond angle, and dihedral angle between atoms in a chain. Although this input is not useful for cyclic or branched systems, it can be an intuitive form of input for some systems.

**(An) Output: (Part of) The Potential Energy Surface**

The potential energy surface (PES) is a plot of the energy of a system as a function of geometric degrees of freedom. Minima correspond to the most stable geometries, where the global minimum is a good guess at the native configuration of a molecular system. A common example of a PES is a Morse potential where energy is charted as a function of bond-length, however the true PES is a function of every degree of freedom a molecule possesses. In practice, PES's are typically represented as graphs charting energy as a function of one to three degrees of freedom or linear combinations of them. This requires the scientist to place

constraints on her system, for example setting specific bond-lengths in parts of the system and plotting how the energy changes in response to changing a single variable.

Understanding the nature of an arbitrary PES is important as it lends insight to the goal of a computation. When one is attempting to understand a system she wants to know about how the system behaves in nature, therefore the lowest energy configuration must be established before further calculations can commence. This process is known as a geometry optimization, and involves finding the global minimum of the PES function although this is certainly easier said than done. There is no surefire way to reach a global minimum of any function, however most computational methods do so in a step-wise gradient descent approach starting from the initial guess provided in the input file and following the PES downhill. The gradient of a two dimensional PES tracking two degrees of freedom $q_1$ and $q_2$ is calculated by taking the partial derivative of each degree of freedom with respect to each other: $\vec{\nabla}E = \left( (\frac{\delta E}{\delta q_1})_{q_2}, (\frac{\delta E}{\delta q_2})_{q_1} \right)$. Thresholds (or tolerances) can be set for $\delta q_n$ to tune step size and the threshold for $\vec{\nabla}E \approx 0$ sets precision.

The PES is used to describe much of the physical nature of chemicals, and describing and operating upon this surface is what computational chemistry is all about. Whether it be describing difficult PES with model functions or traipsing from one minimum to another along a saddle-point seeking a trajectory to describe transition states, this function is the most fundamental idea behind this last hundred years of study. The following text will describe different ways chemists and physicists have tried to describe the PES of systems, and outline the methodology of constructing the PES of an arbitrary input geometry.

## 2.2   Classical Methods

What is the motivation behind trying to describe a chemical system classically? When considering the electronic Hamiltonian $\hat{H}$ in the Schrödinger equation $\hat{H}\Psi = E\Psi$ for a

diatomic hydrogen gas molecule;

$$\hat{H} = -\frac{\hbar^2}{2m_e}\sum_{i=1}^{2}\nabla i^2 + \frac{e^2}{4\pi\epsilon_0}\left[\frac{1}{R} - \sum_{i=1}^{2}\left(\frac{1}{|r_i - R_A|} + \frac{1}{|r_i - R_B|}\right) + \frac{1}{|r_2 - r_1|}\right] \tag{2.1}$$

$\hat{H}$ depends on the kinetic energy of the electrons, the nuclear repulsion term, the electron-nuclear attraction term and the electron repulsion. If extended to a box of hydrogen gas the Hamiltonian quickly becomes incredibly complicated, and even more so if considering, say, a lattice of carbon nanotubes. Thus is the crux of computational chemistry; to make approximations and harness the power of modern computers to solve this problem with tunable accuracy and describe electronic phenomena to a level of detail a researcher requires.

### 2.2.1 Force Fields and Molecular Mechanics

Molecular mechanics (MM) methods represent the energy of a system as a force field according to the following equation.

$$E_{MM} = \sum_{bonds} E_{bond}(\vec{q}) + \sum_{angles} E_{angle}(\vec{q}) + \sum_{dihedrals} E_{dihedral}(\vec{q}) + \sum_{atom\ pairs}\left(E_{Coulomb}(\vec{q}) + E_{dispersion}(\vec{q})\right) \tag{2.2}$$

Although this model has no consideration of electronic spin or chemical reaction, MM can describe conformational changes and intermolecular interactions, making it a widely used tool to describe proteins and extended materials systems.

The bond distortion energy depends on an empirical force constant unique to each atomic pair in the system.

$$E_{bond}(R_{AB}) = \frac{1}{2}k_{AB}(R_{AB} - R_0)^2 \tag{2.3}$$

This model does not allow for bond breaking or forming, but can be tuned to reflect anharmonicity by replacing the Harmonic with a higher order polynomial or Morse potential.

The angle distortion energy can be extended to higher order, however there are some notable drawbacks to this proposed equation.

$$E_{angle}(\theta_{ABC}) = \frac{1}{2}k_{ABC}(\theta_{ABC} - \theta_0)^2 \tag{2.4}$$

11

A linear bond angle cannot be described, and only one local minimum is considered. Out of plane bending is also not included in this, such as the inversion of ammonia.

The energy about the change in a dihedral angle, or the torsional energy, reflects an overall period of $2\pi$ (or less) with a maximum at each barrier.

$$E_{tors}(\phi_{ABCD}) = \frac{U_{barrier}}{2}[1 + \cos(n\phi - \phi_0)] \tag{2.5}$$

Changing $n$ allows control of the periodicity, and $\phi_0$ controls the offset.

The Coulombic terms of the MM energy equation are calculated between partially charged species that are not bonded nor in the same bonding network.

$$E_{Coulomb} = \frac{1}{2} \sum_{A,B}^{nonbonded} \frac{1}{4\pi\epsilon_0} \frac{q_A q_B}{R_{AB}} \tag{2.6}$$

For example, two hydrogens on an ammonia molecule will have no Coulombic energy between them nor with a neighboring hydrogen gas molecule, however they will have a nonzero Coulombic energy term between them and another neighboring ammonia molecule.

The dispersion or van der Waals energy is restricted by setting a distance under which it should be considered.

$$E_{dispersion} = \sum_{A,B}^{restricted} 4\epsilon \left[ \left( \frac{\sigma}{R_{AB}} \right)^{12} - \left( \frac{\sigma}{R_{AB}} \right)^{6} \right] \tag{2.7}$$

This also does not consider atoms within the same bonding network. One can control the amplitude of this energy function with the parameter $\epsilon$ and the shift with $\sigma$.

The force field described above is considerably parameterized. Values of $R_0, \theta_0, \phi_0, k_{AB}$, $k_{ABC}, U_{barrier}, n, q_i, \epsilon$ and $\sigma$ for all atoms or atom pairs are determined experimentally or with higher level computations like *ab initio* methods.

Molecular mechanics might seem questionable in the number of approximations it uses, however as stated before this is an invaluable tool for people studying large systems. With MM one can perform energy decompositions, geometry optimizations, and molecular dynamics. To perform molecular dynamics one must take the gradient of $E_{MM}$ and derive the

acceleration of the particles. From there an integration scheme is employed to solve Newton's second law and classical kinematic equations to predict the lowest energy trajectory of the particles in the system.

## 2.3 Ab Initio Quantum Chemistry

As stated, MM does not explicitly treat electrons quantum mechanically, so how would one go about describing a system in a more fine grained and electronically motivated manner? Let us step through the electronic Hamiltonian for He to scaffold the following methods. The Shrödinger equation for He is $\hat{H}\Psi = E\Psi$, where:

$$\Psi = (\vec{r_1}, \vec{r_2})$$
$$\hat{H} = -\frac{\hbar^2}{2m_e}\nabla_1^2 - \frac{Ze^2}{4\pi\epsilon_0 r_1} - \frac{\hbar^2}{2m_e}\nabla_2^2 - \frac{Ze^2}{4\pi\epsilon_0 r_2} + \frac{e^2}{4\pi\epsilon_0 r_{12}}$$

(2.8)

The elements of the Hamiltonian operator are the kinetic energy of electron one, the Coulombic attraction of electron one and the nucleus, analogous terms for electron two and finally the electron repulsion between electrons one and two.[39] If you ignore the fifth term of the second equation, you can approximate the operator as a pair of $He^+$ Hamiltonians, where the wavefunction is the product of the wavefunctions of the individual electrons and the energy is a sum of individual electron energies. The ground state (GS) wavefunction could therefore be represented as:

$$\phi(\vec{r_1}, \vec{r_2}) = \psi_0(\vec{r_1})\psi_0(\vec{r_2}) = Ne^{-2\vec{r_1}/a_0}e^{-2\vec{r_2}/a_0}$$

(2.9)

If a GS wavefunction $\psi_0$ has energy $E_0$, then the energy expectation value is $E_0^{gs}$,

$$\frac{\int \psi_0^* \hat{H}\psi_0 d\tau}{\int \psi_0^* \psi_0 d\tau} = E_0^{gs}$$

(2.10)

and the variational principle postulates that the energy expectation value of any trial wavefunction $\phi$ is greater than or equal to $E_0^{trial}$.

$$\frac{\int \phi^* \hat{H}\phi d\tau}{\int \phi^* \phi d\tau} \geq E_0^{trial}$$

(2.11)

Therefore, every wavefunction is a superposition of $\psi_0$ and higher energy eigenfunctions.

This notion of variationally minimizing an object with respect to some parameter relates closely to how density functional tight-binding (DFTB) expresses a ground state density through a Taylor expansion, so let's examine this carefully. To use eqn. 2.11, one might define $\phi$ as a trial wavefunction with variable parameters (eg. a sum of Gaussians), then minimize the energy expectation value with respect to those parameters. The resulting wavefunction and energy will be the closest possible representation of $\psi_0$ and $E_0$ achievable within the scope of the functions explored (ie. the span of the basis).[40] For an example, lets consider electron shielding, $Z_{eff}$ as an adjustable parameter.

$$\phi(\vec{r_1}, \vec{r_2}, Z_{eff}) = N e^{-Z_{eff}(\vec{r_1}+\vec{r_2})/a_0} \tag{2.12}$$

In this scenario we find the $Z_{eff}$ where the energy expectation value is the lowest. By the variational principle this indicates that the lowest answer will be the most similar to the correct answer, so minimization of this equation provides the closest possible answer with respect to the chosen parameter. The flexibility of the chosen parameters allows for $\phi$ to approximate $\psi_0$ and $E_0$.

Decomposing $\psi_0$ into individual contributions from each electron $\psi(\vec{r_1}, \vec{r_2}) = \phi_{1s}(\vec{r_1})\phi_{1s}(\vec{r_2})$ is known as the Hartree product wavefunction. In this approximation the electrons are truly independent, not satisfying the Pauli principle that demands all spin functions to be orthogonal to each other. By treating electrons independently, Hartree-Fock (HF) theory requires the construction of spin orbitals from the spatial and spin components of the one electron Hamiltonian.

$$\chi(x_i) = \phi(\vec{r_i})\alpha(\omega_i) \tag{2.13}$$

In order to satisfy the Pauli principle one must construct a Slater determinant where every electron is associated with each orbital, and electron correlation can be considered.[41]

$$\psi(\vec{x_1}, \vec{x_2}) = \frac{1}{\sqrt{2}} \begin{vmatrix} \chi_1(\vec{x_1}) & \chi_2(\vec{x_1}) \\ \chi_1(\vec{x_2}) & \chi_2(\vec{x_2}) \end{vmatrix} \longrightarrow \psi(\vec{x_1}, \vec{x_2}) = |\chi_1\chi_2\rangle \tag{2.14}$$

Electron correlation refers to the likelihood that finding one electron in a certain location is affected by the presence of another electron. When one can decompose the probability density of both electrons into the product of the individual electron densities as is demonstrated by the Hartree product in eqn. 2.9, this indicates that these probability densities are independent and that the location of each electron is completely unaffected by the outside electron cloud. In nature this is of course untrue, and electrons cluster themselves into favorable atomic or molecular orbitals to minimize electron repulsion. The two electron probability functions of same and opposite spin electrons respectively are listed below.

$$P_{\uparrow\downarrow}(\vec{r_1}, \vec{r_2}) = \frac{1}{2}\Big[|\phi_1(\vec{r_1})|^2|\phi_2(\vec{r_2})|^2 + |\phi_1(\vec{r_2})|^2|\phi_2(\vec{r_1})|^2\Big]d\vec{r_1}\vec{r_2}$$

$$P_{\uparrow\uparrow}(\vec{r_1}, \vec{r_2}) = \frac{1}{2}\Big[|\phi_1(\vec{r_1})|^2|\phi_2(\vec{r_2})|^2 + |\phi_1(\vec{r_2})|^2|\phi_2(\vec{r_1})|^2 \tag{2.15}$$

$$- \Big(\phi_1^*(\vec{r_1})\phi_2^*(\vec{r_2})\phi_2(\vec{r_1})\phi_1(\vec{r_2}) + \phi_1^*(\vec{r_2})\phi_2^*(\vec{r_1})\phi_2(\vec{r_2})\phi_1(\vec{r_1})]d\vec{r_1}\vec{r_2}\Big)\Big]d\vec{r_1}\vec{r_2}$$

As shown by the final term in $P_{\uparrow\uparrow}$, same spin electrons in a Slater determinant are correlated. This process is similar to finding the inner product $\langle\chi_1\chi_2|\chi_1\chi_2\rangle$.

## 2.3.1 Hartree-Fock Theory (HF)

**Mathematical Formulation -** The goal of Hartree-Fock (HF) theory is to use the variational principle and apply it to the specific case of a single Slater determinant of one-electron orbitals.[42] This is referred to by physicists as a "mean field theory."

The first procedure of a HF calculation is to evaluate the expectation value of $\hat{H}$ over a Slater determinant. This generally has one or few solutions that describe how an electron feels due to the average electron cloud. Each $\chi_i$ considered can be thought of as an approximate representation of a molecular orbital where each function has a real three dimensional shape. The many electron Hamiltonian is comprised of the kinetic energy of the

electrons, the electron-nuclear attraction and electron-electron repulsion terms. Using the Born-Oppenheimer approximation (where nuclei are fixed) the many electron Hamiltonian can be represented as:

$$\hat{H} = \sum_{i=1}^{n} \frac{-\hbar^2}{2m_e} \nabla_i^2 + \sum_{i=1}^{n} \left( \sum_{A=1}^{N} \frac{-Z_A e^2}{4\pi\epsilon_0 |r_i - R_A|} \right) + \sum_{i=1}^{n} \left( \sum_{j=1}^{i} \frac{e^2}{4\pi\epsilon_0 |r_i - r_j|} \right) \qquad (2.16)$$

Using atomic units, or a.u. convention to simplify this equation, eqn. 2.16 can be written as:

$$\hat{H} = \sum_{i=1}^{n} \hat{h}_i + \frac{1}{2} \sum_{i+j=1}^{n} \hat{g}_{ij} \qquad (2.17)$$

The one electron operator $\hat{h}$ incorporates the kinetic energy and attractive terms while the two electron operator $\hat{g}$ calculates repulsive terms. They are expanded in a.u. below.

$$\hat{h}_i = -\frac{1}{2}\nabla_i^2 - \sum_{A=1}^{n} \frac{Z_A}{r_{iA}}$$

$$\hat{g}_{ij} = \frac{1}{|r_i - r_j|} = \frac{1}{r_{ij}} \qquad (2.18)$$

According to Slater-Condon rules for one-electron operators, the expectation value of $\hat{h}$ over identical determinants evaluates to a sum; $\sum_{i=1}^{n} \langle \chi_i | \hat{h} | \chi_i \rangle$. If determinants differ by a single orbital $(\chi_k \rightarrow \chi_l)$ the expectation value evaluates to $\langle \chi_k | \hat{h} | \chi_l \rangle$. If determinants differ by two or more orbitals, the expectation value is zero.

The two-electron operator is more difficult to decompose as it includes electron correlation and is therefore spin dependent. For the opposite spin circumstance, $P_{\uparrow\downarrow}$ remains as describes in eqn. 2.15. Using this format to calculate electron repulsion, one applies $\frac{1}{r_{12}}$ and integrates.

$$P_{\uparrow\downarrow}(\vec{r_1}, \vec{r_2}) = \frac{1}{2} \int \int |\phi_1(\vec{r_1})|^2 \frac{1}{r_{12}} |\phi_2(\vec{r_2})|^2 + |\phi_1(\vec{r_2})|^2 \frac{1}{r_{12}} |\phi_2(\vec{r_1})|^2 d\vec{r_1} d\vec{r_2}$$

$$J_{12} = \int \int |\phi_1(\vec{r_1})|^2 \frac{1}{r_{12}} |\phi_2(\vec{r_2})|^2 d\vec{r_1} d\vec{r_2} \qquad (2.19)$$

$$\langle \chi_1 \chi_2 | \frac{1}{r_{12}} | \chi_1 \chi_2 \rangle = \frac{1}{2}(J_{12} + J_{12}) = J_{12}$$

Each term in the opposite spin case is a Coulombic interaction. $J_{12}$ can therefore be thought of as the Coulombic repulsion term, or electrostatic term. Notice that each electron is calculated to inhabit each orbital.

For electrons with the same spin this Coulombic term is present as well, however as seen in eqn. 2.15 there is a slightly more bulky term incorporating electron correlation. Calculation of the analogous electron repulsion term as above for electrons with the same spin looks as follows:

$$
P_{\uparrow\uparrow}(\vec{r_1}, \vec{r_2}) = \frac{1}{2} \int \int |\phi_1(\vec{r_1})|^2 \frac{1}{r_{12}} |\phi_2(\vec{r_2})|^2 + |\phi_1(\vec{r_2})|^2 \frac{1}{r_{12}} |\phi_2(\vec{r_1})|^2
$$
$$
- \left( \phi_1^*(\vec{r_1})\phi_2^*(\vec{r_2}) \frac{1}{r_{12}} \phi_2(\vec{r_1})\phi_1(\vec{r_2}) + \phi_1^*(\vec{r_2})\phi_2^*(\vec{r_1}) \frac{1}{r_{12}} \phi_2(\vec{r_2})\phi_1(\vec{r_1})] d\vec{r_1}\vec{r_2} \right) d\vec{r_1}\vec{r_2}
$$
$$
K_{12} = \int \int \phi_1^*(\vec{r_1})\phi_2^*(\vec{r_2}) \frac{1}{r_{12}} \phi_2(\vec{r_1})\phi_1(\vec{r_2}) d\vec{r_1}\vec{r_2}
$$
$$
\langle \chi_1\chi_2 | \frac{1}{r_{12}} | \chi_1\chi_2 \rangle = \int \int |\phi_1(\vec{r_1})|^2 \frac{1}{r_{12}} |\phi_2(\vec{r_2})|^2 - \phi_1^*(\vec{r_1})\phi_2^*(\vec{r_2}) \frac{1}{r_{12}} \phi_2(\vec{r_1})\phi_1(\vec{r_2}) d\vec{r_1}\vec{r_2}
$$
$$
= J_{12} - K_{12}
$$

$$(2.20)$$

This $K_{12}$ term can be thought of as an exchange term. Electrons with the same spin are therefore, and understood chemically, less stable near each other than they would be if they had opposite spins. This satisfies the Pauli principle that orbitals be occupied by two spin paired electrons.

HF theory therefore calculates the energy by taking the expectation value of the Hamiltonian over a single Slater determinant. The energy is notably not a simple sum of orbital energies.

$$E(|\chi_i...\chi_n\rangle) = \langle\chi_i...\chi_n|\hat{H}|\chi_i...\chi_n\rangle$$

$$= \langle\chi_i...\chi_n|\sum_{i=1}^{n}\hat{h}_i + \frac{1}{2}\sum_{i,j=1}^{n}\hat{g_{i,j}}|\chi_i...\chi_n\rangle$$

$$= \sum_{i=1}^{n}\langle\chi_i...\chi_n|\hat{h}_i|\chi_i...\chi_n\rangle + \frac{1}{2}\sum_{i,j=1}^{n}\langle\chi_i...\chi_n|\frac{1}{r_{12}}|\chi_i...\chi_n\rangle \quad (2.21)$$

$$= \sum_{i=1}^{n}\langle\chi_i|\hat{h}_i|\chi_i\rangle + \frac{1}{2}\sum_{i,j=1}^{n}(ii|jj) - (ij|ji)$$

$$E = \sum_{i=1}^{n}\epsilon_i + \frac{1}{2}\sum_{i,j=1}^{n}J_{ij} - K_{ij}$$

The second task of a HF calculation is to vary the one electron orbitals to minimize the energy. According to the variational principle, the expectation value of the Hamiltonian over any trial Slater determinant is greater than or equal to the true energy of the system. What follows therefore is to define a basis of orbitals $\chi_i$ that minimize the energy of the system subject to the constraint that the orbitals be orthonormal. Orthonormality is defined below in eqn. 2.22.

$$\langle\chi_i|\chi_j\rangle = \int \chi_i^*(\vec{r})\chi_j d\vec{r} = \begin{cases} 1 & \text{if } i = j \\ 0 & \text{if } i \neq j \end{cases} = \delta_{ij} \quad (2.22)$$

This minimization technique can be thought of in the light of a Lagrangian approach where one minimizes an auxiliary function describing the constraint.

$$F(x,y,z) = f(x,y,z) - \lambda g(x,y,z)$$

$$L[\{\chi_i\}] = E[\{\chi_i\}] - \sum_{i,j=1}^{n}\lambda_{ij}(\langle\chi_i|\chi_j\rangle - \delta_{ij}) \quad (2.23)$$

One then takes the variation (or functional derivative) with respect to $\chi_i \rightarrow \chi_i + \delta\chi_i$,

$$\delta L[\{\chi_i\}] = \sum_{i=1}^{n}\langle\delta\chi_i|\hat{h}_i|\chi_i\rangle + \frac{1}{2}\sum_{i,j=1}^{n}(\delta\chi_i\chi_i|\chi_j\chi_j) - \delta\chi_i\chi_j|\chi_j\chi_i)$$

$$- \sum_{i,j=1}^{n}\lambda_{ij}\langle\delta\chi_i|\chi_j\rangle + \text{ all complex conjugates} \quad (2.24)$$

$$\delta L[\{\chi_i\}] = 0$$

followed by factoring out the orbital perturbation $\delta\chi_i$,

$$0 = \sum_{i=1}^{n} \langle \delta\chi_i | \hat{h}_i | \chi_i \rangle + \frac{1}{2} \sum_{i,j=1}^{n} \left( \langle \delta\chi_i | \hat{j}_i | \chi_i \rangle - \langle \delta\chi_i | \hat{k}_j | \chi_i \rangle - \lambda_{ij} \langle \delta\chi_i | \chi_j \rangle \right)$$

$$0 = \sum_{i=1}^{n} \langle \chi_i | \left( \hat{h}_i + \sum_{j=1}^{n} (\hat{J}_{ij} - \hat{K}_{ij}) \right) | \chi_i \rangle - \frac{1}{2} \sum_{i,j=1}^{n} \lambda_{ij} \langle \delta\chi_i | \chi_j \rangle \tag{2.25}$$

which holds for variations of any of the orbitals $\chi_i$, so:

$$\left( \hat{h}_i + \sum_{j=1}^{n} (\hat{J}_{ij} - \hat{K}_{ij}) \right) | \chi_i \rangle = \sum_{j=1}^{n} \lambda_{ij} | \chi_j \rangle \tag{2.26}$$

Now one might define the one-electron Fock operator using eqn. 2.26, and recast the resulting equation through a unitary transformation of the orbitals (i.e. a linear combination that preserves orthonormality) to define $\epsilon_i$, the energy of a spin orbital.

$$\hat{f}_i = \hat{h}_i + \sum_{j=1}^{n} (\hat{J}_j - \hat{K}_j)$$

$$\hat{f}_i | \chi_i \rangle = \sum_{j=1}^{n} \lambda_{ij} | \chi_j \rangle \tag{2.27}$$

$$\hat{f}_i | \chi_i \rangle = \epsilon_{i'} | \chi_{i'} \rangle$$

The Fock operator describes molecular orbitals in terms of the kinetic energy of the electrons and their attraction to the nucleus ($\hat{h}_i$) as well as Coulomb ($\hat{J}_i$) and exchange ($\hat{K}_i$) interactions with other electrons. It is formulated in such a way to avoid double-counting, where the elements of $\hat{g}_{ij}$ cancel out when $i = j$. The Fock operator is defined by the molecular orbitals of the system as shown by eqn. 2.27. Therefore we must define the molecular orbital basis set in order to construct $\hat{f}_i$. The crux of all HF equations lies in an iterative eigenvalue problem wherein determining one-electron orbitals and their energies allows for the construction of the Slater determinant for which the energy is minimized.

The final part of a HF calculation therefore lies in introducing the concept of a basis set, and equations by which the orbitals might be iteratively guessed and redefined known as the self-consistent field (SCF) equations - initially outlined by Roothan and Hall.[43] For this approach one must construct a Slater determinant from one-electron molecular orbitals,

19

however as chemists we have a better physical understanding of atomic orbitals. We therefore use atomic orbitals (AO) as a basis to construct molecular orbitals (MO) via linear combination (LC). Let $n$ be the number of electrons (and therefore the number of occupied spin MOs) and $m$ be the total number of AO from which we will construct our Slater determinant ($n \leq m$). A small note is that AO are generally expressed with Greek letters ($\mu, \nu$) while MOs are expressed with Roman letters (i,j). The highest and lowest energy occupied MOs are therefore:

$$
\begin{aligned}
|\chi_1\rangle &= C_{11}\phi_1...C_{m1}\phi_m \\
|\chi_n\rangle &= C_{1n}\phi_1...C_{mn}\phi_m \\
|\chi_i\rangle &= \sum_{\mu=1}^{m} C_{\mu i}\phi_\mu = \sum_{\mu=1}^{m} C_{\mu i}|\mu\rangle
\end{aligned}
\tag{2.28}
$$

Generally, the $i^{th}$ MO is expressed as the $i^{th}$ row of the following matrix, where each AO contributes to the overall shape of the MO according to the values of the MO coefficients.

$$
\begin{bmatrix} \chi_1 \\ \vdots \\ \chi_n \end{bmatrix} = \begin{bmatrix} C_{11} & C_{21} & \ldots & C_{m1} \\ C_{12} & C_{22} & \ldots & C_{m2} \\ \vdots & \vdots & \ddots & \vdots \\ C_{1n} & C_{2n} & \ldots & C_{mn} \end{bmatrix} \begin{bmatrix} \phi_1 \\ \phi_2 \\ \vdots \\ \phi_m \end{bmatrix}
\tag{2.29}
$$

Rewriting our original HF equation (eqn. 2.27) we begin to deconstruct this MO basis into

LCAO that depend on our one-electron spin orbitals.

$$\hat{f}_i|\chi_i\rangle = \epsilon_i|\chi_i\rangle$$

$$\hat{f}_i\sum_{\mu=1}^{m}C_{\mu i}|\mu\rangle = \epsilon_i\sum_{\mu=1}^{m}C_{\mu i}|\mu\rangle$$

$$\Downarrow$$

$$\langle\nu|\hat{f}_i\sum_{\mu=1}^{m}C_{\mu i}|\mu\rangle = \langle\nu|\epsilon_i\sum_{\mu=1}^{m}C_{\mu i}|\mu\rangle$$

$$\sum_{\mu=1}^{m}\langle\nu|\hat{f}_i|\mu\rangle C_{\mu i} = \epsilon_i\sum_{\mu=1}^{m}\langle\nu|\mu\rangle C_{\mu i}$$

$$\text{where } \langle\nu|\hat{f}_i|\mu\rangle = \int \phi_\nu^*(\vec{r}_i,\omega_i)\hat{f}_i\phi_\mu(\vec{r}_i,\omega_i)d\vec{r}_i d\omega_i$$

$$F_i = \begin{bmatrix} \int \phi_1^* f_i\phi_i d\tau & \int \phi_2^* f_i\phi_i d\tau & \cdots \\ \int \phi_2^* f_i\phi_i d\tau & \ddots & \\ \vdots & & \end{bmatrix}$$

$$S_i = \begin{bmatrix} \int \phi_1^*\phi_i d\tau & \int \phi_2^*\phi_i d\tau & \cdots \\ \int \phi_2^*\phi_i d\tau & \ddots & \\ \vdots & & \end{bmatrix}$$

$$\tag{2.30}$$

$$\Downarrow$$

$$\mathbb{F}\vec{c} = \epsilon\mathbb{S}\vec{c}$$

These Roothan-Hall equations are recursive. To apply eqn. 2.30, first a guess is used to construct an initial MO coefficient matrix ($\mathbf{C}^0$) and then to build the Fock matrix ($\mathbf{F}^0$). One then solves the general eigenvalue equation for $\mathbf{C}^1$ and $\epsilon^1$ followed by computation of $\mathbf{F}^1$ from $\mathbf{C}^1$. This continues until $\Delta\epsilon$ has converged below some threshold.

The Fock matrix elements incorporate the four main electronic energy components of the Hamiltonian:

$$F_{\mu\nu} = T_{\mu\nu} + V_{\mu\nu} + J_{\mu\nu} + K_{\mu\nu}$$

$$T_{\mu\nu} = \langle\mu| - \frac{1}{2}\nabla^2|\nu\rangle : \text{The KE}$$

$$V_{\mu\nu} = -\sum_A \langle\mu|\frac{Z_A}{r_A}|\nu\rangle : \text{The electron/nuclear attraction}$$

$$J_{\mu\nu} = \sum_{\lambda\sigma} P_{\lambda\sigma}(\mu\lambda|\nu\sigma) : \text{The Coulombic term}$$

$$K_{\mu\nu} = -\frac{1}{2}\sum_{\lambda\sigma} P_{\lambda\sigma}(\mu\lambda|\nu\sigma) : \text{The exchange term}$$

$$\tag{2.31}$$

Both $J_{\mu\nu}$ and $K_{\mu\nu}$ use the density matrix and rely on four separate indices. This is the most computationally expensive part of a HF calculation, causing this method to scale $O(N^4)$. The convergence criteria can be manipulated according to the calculation at hand. A few examples of convergence criteria would be the change in energy, the change in MO coefficients, or the change in the gradient. Any of these values can be tested against some defined threshold to determine when a calculation had converged satisfactorily.

**Basis Sets -** Basis sets are functions that describe molecular (or crystal) orbitals from an atomic orbital basis. The higher the level of physical description of the atomic orbitals the more precise a calculation will be, but the computational cost will increase. These bases are linearly independent vectors that can be infinitely added to describe a space that increases in dimension with every additional vector. The synonymous wording for this application is the infinite addition of orthonormal basis functions to describe an increasingly complex electronic space - the more basis functions included, the more well described the space.

An example of these basis functions is a Slater-type orbital (STO). These functions are generally described by the form: $R(r) = Nr^l e^{-\zeta r}$. They describe long-range behavior well and introduce no radial nodes. Manipulating the $\zeta$ term allows for control of how diffuse or localized the function is. STOs are used without alteration in methods like extended Hückel, however they can be problematic to use in *ab initio* methods as the Coulombic integrals often do not have real solutions. These time intensive calculations are often precomputed for *ab initio* methods and approximated for HF.

STOs can be approximated with a sum of Gaussian functions, $R(r) = Nr^l e^{-\alpha r^2}$ where the $\alpha$ term is varied to replicate the cusp conditions of a STO, wherein there is a derivative discontinuity or kink at the nucleus. Gaussian-type orbitals (GTO) are inherently inaccurate at $r = 0$ where an STO predicts a derivative of infinity and a GTO predicts a derivative of zero, however both do well at long range.

Examples of select basis set construction follow. Minimal basis sets like the group STO-

MG approximate Slater-type atomic orbitals with a sum of 2-6 GTO (eg. STO-3G) and represent the low end of physical description. Split-valence basis sets include virtual orbitals and represent atomic orbitals with multiple STO with different $\zeta$. This class includes the "double-" and "triple-zeta" family of basis sets, and have names like 3-21G. Basis sets with this type of nomenclature were created by John Pople whose lab has also produced triple- and quadruple-zeta split valence basis sets which would have three or four numerical values after the dash, respectively. The basis set 3-21G* is similar to the aforementioned example, however this basis set includes polarization functions with higher angular momentum quantum numbers ($p \rightarrow d$). 3-21+G includes diffuse functions with higher principle quantum numbers ($2p \rightarrow 3p$). Pople basis sets are becoming out of date, due to their cost to accuracy ratio. Another popular group of basis sets were developed by the Dunning lab. They have names cc-pVDZ which can be read as "correlation-consistent polarized valence-only double $\zeta$" and are optimized for calculations involving electron correlation.

Most computational chemists need only choose a basis set, weighing their individual preference in the spectrum of precision versus expense. The ideal basis set closely reproduces the MO of your system using the fewest possible functions. To indicate what kind of calculation has been attempted, one describes both the method and the basis set. For example, HF/6-311G//HF/3-21G indicates that a single point HF calculation with 6-311G (a triple-zeta Pople type basis set) was followed by a HF geometry optimization with 3-21G (a double-zeta Pople type basis set).

**In Practice -** HF calculations come in two main flavors, restricted (RHF) and unrestricted (UHF). RHF calculations are cheaper as they fill up the occupied MO with pairs of opposite spin electrons, but as UHF calculates spin-specific MO (twice as many MO as RHF) UHF is required for systems with unpaired electrons. Having both options available is important in the face of "wavefunction instability" where SCF calculations can converge on a solution that is not actually the lowest energy configuration of the system. Perhaps a RHF calculation

converges for a system where a closed shell singlet is not truly the lowest energy electron configuration. To correctly describe a singlet bi-radical system, or a triplet state, one would need to use UHF to resolve the RHF/UHF instability. Remember - the variational principle does *not* guarantee that SCF calculations always converge on the global minimum!

Another thing to take into consideration is the convergence with respect to basis set size. The higher number of Gaussian type functions, the higher the accuracy. It is possible to extrapolate to a "complete" basis set:

$$E_\chi^{HF} = E_{CBS}^{HF} + Ae^{-\alpha\chi}$$

$$\chi = \text{The number of GTO in each AO (or } \zeta)$$ 

$$A, \alpha = \text{Empirical values}$$

(2.32)

Going beyond triple-zeta is often unnecessary in HF as the electron correlation error can overcome the basis set limits. Additionally, HF scales $O(N^4)$, where $N$ is the number of basis functions, therefore larger basis sets can be needlessly expensive. However, that is not to say that larger basis sets are always unnecessary. For calculations regarding thermochemistry one needs a larger basis set to capture reaction energetics, and should choose a basis set that treats electron correlation appropriately. For a geometry optimization, one can find the lowest energy molecular geometry with a small basis set, as HF accuracy depends on specific chemical bonds. A larger basis set will improve the accuracy of the energy by shifting the potential energy surface to a lower energy, however it will not change where the local or global minima are. Hearkening back to the variational principle, allowing for a larger test space can lead you closer to the correct answer, and for a computational chemist the lowest answer is always the better answer when searching for a minimum.

Care should be taken when calculating intermolecular interactions with HF, as there is no explicit electron correlation and therefore an empirical dispersion energy should be added to the calculated HF energy. HF is also not a size-consistent approach, and dissociation energy

cannot be calculated as it would be when using an approach like *ab initio*. Size-consistency refers to the total energy equaling the sum of the parts ($E_{AB} = E_A + E_B$).

### 2.3.2   Wavefunction-based Correlation Methods (WF)

**Configuration Interaction (CI) -**   HF is not an exact method, the most egregious approximation being made when describing an electronic system with a single Slater determinant. This method can describe static electron correlation, but neglects dynamic electron-electron interactions due to averaging.

$$E = \left\langle \chi_1...\chi_n \middle| \hat{H} \middle| \chi_1...\chi_n \right\rangle$$
$$\hat{f}_i(\{\chi_k\}) \middle| \chi_i \rangle = \epsilon_i \middle| \chi_i \rangle \tag{2.33}$$

Each $\hat{f}_i$ calculates the energy of a one-electron orbital, only considering the interaction of the $i^{th}$ electron with the average electron cloud, but this is a large approximation for some systems. If one Slater determinant is not enough to correctly describe a system, one could construct a wavefunction as a linear combination of weighted Slater determinants. These additional Slater determinants would include contributions from the virtual orbitals to increase the flexibility of the wavefuncton description.

$$\Psi_{CI} = \left| \chi_1...\chi_n \right\rangle + c_1 \left| \chi_1...\chi_{n-1}, \chi_{n+1} \right\rangle + ...$$
$$\Psi_{CI} = \Psi_{HF} + c_1 \Psi_1 + ... \tag{2.34}$$

One can construct as many $\mathbf{C}_i \Psi_i$ as there are available promotions. Below, $i$ indicates the occupied orbital the electron has been "excited" from, and $a$ indicated the virtual orbital it is "excited" to.

$$\left| \Psi_{HF} \right\rangle = \left| \chi_1...\chi_n \right\rangle$$
$$\left| \Psi_i^a \right\rangle = \left| ...\chi_a... \right\rangle : \text{Singly excited (CIS)} \tag{2.35}$$
$$\left| \Psi_{ij}^{ab} \right\rangle = \left| ...\chi_a...\chi_b... \right\rangle : \text{Doubly excited (CISD)}$$

A full CI calculation where every electron is excited from an occupied to a virtual orbital is in theory a perfectly exact solution for the many-electron wavefunction in the chosen basis.

$$\left|\psi\right\rangle = \left|\psi_{HF}\right\rangle + \sum_{i\to a} c_i^a\left|\psi_i^a\right\rangle + \sum_{\substack{i\to a \\ j\to b}} c_{ij}^{ab}\left|\psi_{ij}^{ab}\right\rangle + ... \tag{2.36}$$

This function eventually truncates in a finite basis, as although one can always increase the number of virtual orbitals by extending the basis set size, a calculation will only ever have $n$ substitutions as there are only $n$ occupied orbitals. To find the energy of a CI calculation, one applies Slater-Condon rules as outlined below.

$$\left\langle\chi_1...\chi_n\left|\hat{h}\right|\chi_1...\chi_n\right\rangle = \sum_{i=1}^n\left\langle\chi_i\left|\hat{h}\right|\chi_i\right\rangle$$

$$\left\langle\chi_1...\chi_k...\chi_n\left|\hat{h}\right|\chi_1...\chi_l...\chi_n\right\rangle = \left\langle\chi_k\left|\hat{h}\right|\chi_l\right\rangle \tag{2.37}$$

$$\left\langle\chi_1...\chi_k\chi_l...\chi_n\left|\hat{h}\right|\chi_1...\chi_p\chi_q...\chi_n\right\rangle = 0$$

Truncating a CI calculation at single excitations (CIS) or double excitations (CISD) can often recover over 90 percent of the electron correlation. This method is very computationally expensive, and suffers from the same lack of size-consistency as HF.

**Coupled Cluster (CC) -** Continuing on the road to a well-described electron correlation, one arrives at the coupled cluster (CC) approach to HF modification which fixes the size-inconsistency of HF and CIS/D.[44] Let's define the cluster operator, $\hat{T}_n$:

$$\hat{T}\left|\psi\right\rangle = \frac{1}{4}\sum_{ijab} t_{ij}^{ab}\left|\psi_{ij}^{ab}\right\rangle$$

$$\hat{T} = \hat{T}_1 + \hat{T}_2 + ... + \hat{T}_n \tag{2.38}$$

What if we applied $e^{\hat{T}}$ to $\left|\psi_{HF}\right\rangle$? eqn. 2.39 shows the cluster operator for both coupled cluster singles (CCS) and coupled cluster singles and doubles (CCSD).

$$e^{\hat{T}} = 1 + \hat{T} + \frac{1}{2}\hat{T}^2 + ... = 1 + \hat{T}_1 + \hat{T}_2 + \frac{1}{2}\hat{T}_1^2 + \hat{T}_1\hat{T}_2 + \frac{1}{2}\hat{T}_2^2 \tag{2.39}$$

This operator introduces higher disconnected excitations (powers and products of $T_i$) even at early truncations. These excitations restore size-consistency, and yield a hierarchy of *ab initio* approximations that are widely employed as the "gold-standard" for benchmarking other electronic-structure methods.

### 2.3.3 Møller-Plesset Perturbation Theory (MP2)

Møller-Plesset time-independent perturbation theory is in essence the tweaking of an easy problem to approximate the solution to a hard one. This method assumes a reference wavefunction derived by HF, and formulates a Hamiltonian comprised of the HF reference Hamiltonian perturbed by a correlation operator, $\hat{V}$.

$$
\begin{aligned}
&\hat{H} = \hat{H}_0 + \lambda \hat{\nu} \\
&\left|\psi_0\right\rangle = \left|\psi_{HF}\right\rangle \\
&\psi = \psi_0 + \lambda \psi^{(1)} + \lambda^2 \psi^{(2)} + ... \\
&E = E^{(0)} + \lambda E^{(1)} + \lambda^2 E^{(2)} + ...
\end{aligned}
\tag{2.40}
$$

The $\lambda$ term is a scalar between zero and one that modifies $\hat{V}$. This lambda is by extension used to scale the first and second order expansions of $\psi$ and $E$. Without any approximations thus far, the Schrödinger equation has been modified as follows:

$$
\begin{aligned}
&\hat{H}\psi = E\psi \\
&(\hat{H}_0 + \lambda \hat{\nu})\psi = E\psi \\
&(\hat{H}_0 + \lambda \hat{\nu})\Big(\sum_{i=0}^{N} \lambda^i \psi^{(i)}\Big) = \Big(\sum_{i=0}^{N} \lambda^i E^{(i)}\Big)\Big(\sum_{i=0}^{N} \lambda^i \psi^{(i)}\Big)
\end{aligned}
\tag{2.41}
$$

By truncating the energy expression to second order and setting terms of the same order with respect to the wavefunction equal, it s possible to derive an expression for the second-order Møller-Plesset (MP2) correlation energy.

$$E_{corr}^{MP2} = -\frac{1}{4} \sum_{i<j}^{occ} \sum_{a<b}^{virt} t_{ij}^{ab} = -\frac{1}{4} \sum_{i<j}^{occ} \sum_{a<b}^{virt} \frac{|(ij|ab) - (ia|jb)|^2}{(\epsilon_a + \epsilon_b) - (\epsilon_i + \epsilon_j)} \qquad (2.42)$$

## 2.4 Semi-Empirical Approaches

Methods that fall in the *ab initio* category are computationally expensive due to a full electronic treatment. Semi-empirical approaches attempt to reduce this computational burden by pretabulating or experimentally determining the many simple expressions within these methods that need to be calculated at every iteration. Density functional tight-binding (DFTB), the semi-empirical star of this work, parameterizes a significant amount of a full electronic structure calculation allowing similar accuracy at a fraction of the time. In semi-empirical approaches, pretabulated and experimental parameters are calculated or collected for particular bonds or groups of atoms in high level methods and saved as discreet numbers in parameter libraries. The following method uses parameters substantially, and is a useful tool to describe the kind of paramterization used in DFTB, described in section 3.2.

### 2.4.1 Hückel and Extended Hückel

The Hückel method is a simple semi-empirical technique that uses the single-electron Hartree product orbitals, but does not use Slater determinants. This method therefore does not account for electron correlation, exchange, nor does it necessarily consider the Pauli principle. The goal of these calculations is to obtain a qualitative description of the shape, energy, and ordering of a system's MO. This method is valuable to investigate as a simple and transparent vessel to allow us to understand the equations that form the foundation of other MO methods like DFTB (section 3.2.) The Hückel method can be compared to DFTB in that the matrix elements of both methods are known, and the problem can be simplified to an eigenvalue and eigenvector search.[45] By visualising Hückel methodologies, later description of DFTB, the focal point of this manuscript, will be simpler for the reader to visualize.

**Mathematical Formalism -**  Let's begin by describing the Hückel treatment of $H_2$ and approximate the $H_2$ MO as an LCAO.

$$\psi = c_1\phi_1 + c_2\phi_2$$
$$\hat{H}(c_1\phi_1 + c_2\phi_2) = E(c_1\phi_1 + c_2\phi_2)$$

(2.43)

Next, left-multiply by one AO and integrate over all space (could use $\phi_1$ or $\phi_2$) to define the secular equations.

$$\int \phi_1\hat{H}(c_1\phi_1 + c_2\phi_2) = \int \phi_1 E(c_1\phi_1 + c_2\phi_2)$$
$$c_1\int \phi_1\hat{H}\phi_1 + c_2\int \phi_1\hat{H}\phi_2 = c_1 E\int \phi_1\phi_1 + c_2 E\int \phi_1\phi_2$$

(2.44)

These secular equations are divided into discrete parts that are each assigned a value in the Hückel method. The latter half of eqn. 2.44 becomes;

$$c_1\alpha + c_2\beta = Ec_1 + 0$$

(2.45)

Let's dive into this approximation. $\alpha = \int \phi_1\hat{H}\phi_1$ is the Coulomb integral, expressing the initial energy of each AO. $\beta = \int \phi_1\hat{H}\phi_2$ is a resonance integral, which defies a classical description to describe the electron transfer and resonance between $\phi_1$ and $\psi_2$. $\int \phi_1\phi_1$ reduces to 1 as each AO is normalized. The biggest approximation made in this method occurs when $\int \phi_1\phi_2$ is reduced to 0. This expression would generally describe the overlap integral, which would have non-zero values due to the fact that AO on different atoms are not mutually orthogonal. This large approximation however is what makes this method so computationally affordable. The following set of equations outlines how one would solve a Hückel calculation for $H_2$.

$$c_1\alpha + c_2\beta = Ec_1$$

$$c_1\beta + c_2\alpha = Ec_2$$

Solve for $c_n + E$. Implicit: $c_1^2 + c_2^2 = 1$

$$\alpha + \frac{c_2}{c_1}\beta = E = \alpha + \frac{c_1}{c_2}\beta$$

$$\frac{c_2}{c_1}\beta = E - \alpha = \frac{c_1}{c_2}\beta \qquad (2.46)$$

$$\frac{c_1}{c_2}\beta = \frac{c_1}{c_2}\beta$$

$$c_1^2 = c_2^2$$

$$c_1 = \pm c_2$$

So what does this tell us? There are two possibilities for this system. Either $c_1 = c_2$ and $E = \alpha + \beta$ or $c_1 = -c_2$ and $E = \alpha - \beta$. The former would describe a bonding MO, while the latter represents the antibondng MO. (Note that both $\alpha$ and $\beta$ are negative numbers!) These equations can be (and generally are) represented as eigenvalue equations. This example looks like:

$$\begin{bmatrix} \alpha & \beta \\ \beta & \alpha \end{bmatrix} \begin{bmatrix} c_1 \\ c_2 \end{bmatrix} = E \begin{bmatrix} c_1 \\ c_2 \end{bmatrix} \qquad (2.47)$$

Notice that the energy is the eigenvalue while the $c_n$ coefficients make up the eigenvector. These eigenvalues and eigenvectors are intrinsic to the matrix made up of the AO energies ($\alpha$) and AO couplings ($\beta$).

Hückel theory is used to evaluate conjugated $\pi$ systems. Let us look then at how one would solve for the MO of butadiene. Butadiene is made up of carbon (2s, 3p) and hydrogen (1s), and has 22 valence MO consisting of a $\sigma$ system and a $\pi$ system. Looking only at the $\pi$ system, we have four out of plane $p$ orbitals denoted hereafter as $\phi_1 - \phi_4$. Because we are only considering $p$ orbitals on carbons, each Coulomb integral will have the same value, that is, each $\alpha$ will have the same numerical value. Let's set up our Hückel eigenvalue problem.

$$
\begin{bmatrix} \alpha & \beta & 0 & 0 \\ \beta & \alpha & \beta & 0 \\ 0 & \beta & \alpha & \beta \\ 0 & 0 & \beta & \alpha \end{bmatrix} \begin{bmatrix} c_1 \\ c_2 \\ c_3 \\ c_4 \end{bmatrix} = E \begin{bmatrix} c_1 \\ c_2 \\ c_3 \\ c_4 \end{bmatrix} \tag{2.48}
$$

Notice the assumption that only AO on explicitly bonded atoms have non-zero resonance integrals. This approximation pales in comparison to the complete disregard of the overlap integrals, and is the primary reason that this method is generally used for a qualitative understanding of conjugated linear and cyclic systems. This system has four eigenvalues corresponding to four eigenvectors, which are shown to one significant figure below.

$$
\hat{H}\vec{c} = (\alpha \pm \beta)\vec{c}
$$

$$
\begin{aligned}
\alpha - m\beta \qquad & \vec{c_1} = (+0.4, +0.6, +0.6, +0.4) \\
\alpha - n\beta \qquad & \vec{c_2} = (+0.6, +0.4, -0.4, -0.6) \\
\alpha + n\beta \qquad & \vec{c_3} = (+0.6, -0.4, -0.4, +0.6) \\
\alpha + m\beta \qquad & \vec{c_4} = (+0.4, -0.6, +0.6, -0.4)
\end{aligned} \tag{2.49}
$$

Each index of the $\vec{c_n}$ describes the relative size of the MO on the carbon corresponding to that index, and the sign of each value describes its orientation. $\vec{c_1}$ is the lowest energy $\pi$ system where there are no nodes. $\vec{c_4}$ describes the fully antibonding MO configuration where there is a node between each carbon unit. $\vec{c_1}$ has a larger electron cloud on the inner carbon units while $\vec{c_2}$ has larger orbitals on the ends of the molecule.

Extended Hückel is a natural progression from the aforementioned method, and differs very little in its general setup. While the integral $\int \phi_1 \phi_1$ still reduces to one, the overlap, Coulomb and resonance integrals are treated slightly differently. $\alpha$, which corresponds to the energy of each AO, is empirically parameterized with ionization energies distinct to different molecular environments. The resonance integrals are still approximated to be $\beta$ or zero

depending on whether or not the two atoms are neighbors, but in extended Hückel $\beta$ is calculated using the Wolfsberg-Helmholtz approximation.[46]

Most notably, the overlap integral $\int \phi_1 \phi_2$ is not disregarded in this method and is explicitly calculated by integrating over the product of the basis functions. These differences allow for extended Hückel calculations to be carried out on molecules with multiple atom types.

## 2.4.2   Comments on Density Functional Methods

The classification of density functional theory (DFT) as either *ab initio* or semi-empirical has often been debated, and indeed the classification tends to be more useful in describing specific functionals over the full theory of density functionals.[47,48] The concept of density functional based methods have been entirely categorized under a semi-empirical umbrella for this manuscript as DFT is the foundation upon which DFTB was built, and the problem-solving techniques present in the conception of this method follow a similar accessibility trend as that main semi-empirical method described here. Because DFT is such a tunable and robust computational strategy, it is easy to assume that it is the only method worth considering. The other aforementioned methods have been described to remind one that this is not the case.

# Chapter Three

# DENSITY FUNCTIONAL THEORETICAL APPROACHES (DFT and DFTB)

As shown in the above first principles approaches, wavefunctions are complicated and time-consuming to fully describe. Density functional theory is a method that approximates the wavefunction of a system by its electronic density, and in so doing can dramatically lower computational cost of large systems. This model termed density functional theory (DFT) radically shifted the way computational chemists approach many-electron calculations and is to this day the most common type of electronic structure calculation that one will encounter. The allure of DFT is that there exits a theoretically attainable and chemically exact solution, and indeed the DFT community is a thriving and ever growing niche of physical chemistry. This author does not work directly in that niche, however, and the following overview in section 3.1 is provided simply to support future students who have only just begun to learn about this discipline as it sets up the primary method of this work smoothly.

DFT has been further approximated to afford the user a desktop friendly density based calculation in the form of density functional tight-binding (DFTB). DFTB is the method upon which this work is focused, and the platform for the the time-independent excited

state framework $\Delta$DFTB, and subsequent molecular orbital relaxation maximum overlap methods (MOM, IMOM, DAD) and time-independent transition dipole moment calculations (TI-TDM). The following chapter will thoroughly introduce DFT and build from that a mathematical formalism of DFTB to ground the method development work in chapter 4 and chapter 5.

## 3.1 Density Functional Theory (DFT)

The formalism of DFT can be understood historically, as this method developed over time as an extension of Hartree-Fock (HF) theory (subsection 2.3.1).[49] In such a method as HF and other wavefunction based methods, each electron is described with three spatial coordinates and a fourth spin coordinate, forcing the definition of $4n$ unique indices for an $n$ electron system, and an additional polynomial scaling to form objects like two electron integrals. Physically, the energy of a chemical system depends on the electron density, not necessarily the wavefunction - but can we express the energy as a function of the electron density ($\rho$) and disregard the wavefunction ($\psi$) entirely? (That is to say, can we accurately define a space using the complex square of the wavefunction and disregard phase information entirely?) Fortunately we can, and the following section will outline the formulation of a model that requires only the intuitive definition of the three spatial coordinates that define the electronic densities of the $\alpha$ (spin-up) electrons, $\beta$ (spin-down) electrons, and difference of these two to determine a magnetization density ($\alpha - \beta$).

**Thomas-Fermi (1927) -** To accomplish the energy calculation of a many electron system one must define an operator for $E$ in terms of $\rho(x, y, z)$. Thomas and Fermi defined the first model as follows:

$$E[\rho(\vec{r})] = V_{ne}[\rho(\vec{r})] + V_{ee}[\rho(\vec{r})] + T[\rho(\vec{r})]$$

$$V_{ne}[\rho(\vec{r})] = \sum_k^{nuc} \int \frac{Z_k}{|\vec{r} - \vec{r_k}|}\rho(\vec{r})d\vec{r}$$

$$V_{ee}[\rho(\vec{r})] = \frac{1}{2}\int\int \frac{\rho(\vec{r_1})\rho(\vec{r_2})}{|\vec{r_1} - \vec{r_2}|}d\vec{r_1}d\vec{r_2}$$

$$T[\rho(\vec{r})] = \frac{3}{10}(3\pi^2)^{2/3}\int \rho^{5/3}(\vec{r})d\vec{r}$$

(3.1)

Unfortunately, this model is terrible unless one is dealing with a metallic system at or near the Fermi level. The final term $T[\rho(\vec{r})]$ is an approximation of the electronic kinetic energy with that of a uniform electron gas (otherwise known as "jellium") which is a pretty scandalous way to treat non-theoretical chemical systems. Small molecules, semiconductors, bio-materials, insulators, and any other system chemically described as bonded are all poorly described by a nearly uniform electron density. Also, this model suffers from the very anticipated flaw that DFT developers sought to disprove - a ton of information is lost without considering the wavefunction here. There is no exchange or correlation considered, neglecting the Pauli principle that leads to non-classical repulsion from electrons with the same spin, and there is no account for self-interaction error. Ignoring self-interaction specifically results in the nonsensical conclusion that a single electron system would have a non-zero electron repulsion term.

**Hohenberg-Kohn (1964) -** The turning point for DFT came in the form of two theorems; the existence theorem and the variational theorem. Pioneered by Hohenberg and Kohn, these two notions validated the DFT proposition to the point that different extensions of density functional based calculations would become the most widely used electronic structure methods in existence.[50,51]

The existence theorem states that the GS electron density of a system uniquely determines the Hamiltonian and therefore all of the properties of that system. Therefore, one can define an exact density functional to express the exact energy of that system. The variational

theorem states that like the wavefunction, the electron density obeys the variational principle, whereby trial wavefunctions or densities can be used to describe a system, and that the lowest energy solution will more closely match the correct answer than the other higher energy trials. In the iterative nature of computation this presents to the user that as the calculated energy of a system goes down, the closer one gets to the exact answer. This suggests how one would find the GS density from an exact density functional, however this model is not useful yet as of 2020. It has been postulated that an exact density gives rise to the exact Hamiltonian of a system and furthermore the exact wavefunction, however this defeats the purpose of DFT as the wavefunction is not being circumnavigated in this situation. Also, we don't know what the exact density functional is yet!

**Kohn-Sham (1965) -** Working with the early DFT method proposed by Thomas and Fermi, Kohn and Sham sought to unite the actualized calculations of 1927 with the exciting ideas of 1964. From their perspective, the Thomas-Fermi model had a major advantage and a major disadvantage - both happened to be that electron-electron interactions were neglected. Although mean field theories like the Thomas-Fermi model of a uniform electron gas, we as chemists cannot avoid the importance of exchange and correlation, both of which were neglected. Kohn and Sham decided to solve this problem via Occam's razor, and simply added a correction term. The term they added was an explicit exchange and correlation component of the energy equation, and according to the existence theorem a correction term exists for which the total energy of any system is exactly correct. The revolutionary new energy functional was as follows:

$$E[\rho(\vec{r})] = V_{ne}[\rho(\vec{r})] + V_{ee}[\rho(\vec{r})] + T[\rho(\vec{r})] + E_{xc}[\rho(\vec{r})] \tag{3.2}$$

As uninteresting as the previous equation may seem, the meat of this idea lies in the construction of $E_{xc}[\rho(\vec{r})]$. Scientists have offered many ideas over the decades for what this functional could be, and the multitude of currently available functionals will be described in

summary later in the chapter (3.1.1). The main takeaway from this idea is the possibilities that Kohn-Sham (KS) DFT offers, for if one could find the exact density functional they would also be able to find the exact GS electron density and the total energy of their system with computational ease. They could also define one-electron KS molecular orbitals (MO) and their respective energies, which according to Koopman's theorem can be used to define a system's HOMO-LUMO gap, ionization energy, electron affinity, etc.[52]

Encapsulated in these functionals are chemically relevant bits of information such as how an electron's kinetic energy changes in response to electron-electron interactions, electron correlation and exchange, and self-interaction corrections. There is still an active field within computational chemistry aimed at improving density functionals. At the moment, certain functionals are better for certain situations and many are parameterized heavily. However, this theory-motivated field works specifically on how to define the perfect $E_{xc}[\rho(\vec{r})]$ such that all of nature can be defined accurately and reliably within the constraints of DFT.

Assuming one is using a suitable density functional, the general procedure of Kohn-Sham DFT is to iteratively define the set of one-electron molecular orbitals $\{\chi_i\}$ that are occupied in their system. The MOs are built from a basis set of atomic orbitals (AOs), $\{\phi_i\}$ that are used to construct a matrix for which the MO coefficients are the eigenvectors, and the energy is the eigenvalue. The elements of this matrix are calculated as follows:

$$F_{\mu\nu} = \left\langle \phi_\mu \middle| -\frac{1}{2}\nabla^2 - \sum_{k}^{nuclei} \frac{Z_k}{|\vec{r}-\vec{r_k}|} + \int \frac{\rho(\vec{r'})}{|\vec{r}-\vec{r'}|} d\vec{r'} + V_{xc} \middle| \phi_\nu \right\rangle \qquad (3.3)$$

Using this expression, one initially will guess some trial density $\rho(\vec{r})$ and iteratively solve for the MO coefficients, updating the density with each step until the change in energy is below some threshold.

### 3.1.1 Jacob's Ladder of Density Functionals

Although DFT is in theory capable of exact accuracy, functionals are developed by scientists to match experiment as closely as possible. Development generally falls into one of two camps; the "bottom-up" first principles approach or the "top-down" empirical approach. First principles folks develop functionals with the ultimate goal of universality, or transferability to a wide range of systems. The form of the functional is derived from known parameters and limits of model system data and augmented with a few adjustable parameters. These functionals tend to be favored by theoretical physicists. The empirical developers, who consist mainly of chemists, try to create functionals that display a particularly high level of accuracy to specific domains of interest. These functional forms are initially guessed and then fit to training data, containing many adjustable parameters.[53–55]

Density functionals come in a range of physical complexity which allows one to choose where each desired calculation falls on the line between computational feasibility and accuracy.[56] The following section will list this classification of functionals in ascending physical complexity, and by extension increasing computational cost.

**Local Density Approximation (LDA) -** This class of functionals is the most approximate, and describes the first rung of Jacob's ladder. There is no unique local density approximation, but "the" LDA usually refers to the exchange-correlation term derived from analysis of a uniform electron gas. Because of this, this method is not good for systems with strongly varying densities. The exchange-correlation energy at each given point depends only on the density at that point, not the density as a whole as is the case in other functionals.

$$E_{xc}^{LDA}[\rho(\vec{r})] = \int \rho(\vec{r})\epsilon_{xc}^{UEG}[\rho(\vec{r})])d\vec{r}$$

$$E_{xc}^{LDA}[\rho(\vec{r})] = \int \rho(\vec{r})\big(\epsilon_x[\rho] + \epsilon_c[\rho]\big)d\vec{r} \tag{3.4}$$

$$\epsilon_x[\rho] = -\frac{9\alpha}{8}\left(\frac{3}{\pi}\right)^{1/3}\rho$$

$\epsilon_c[\rho]$ is not analytical, but instead is calculated with Monte-Carlo. LDA is the simplest func-

tional used in DFT, and can be generalised to account for different spins (LSDA). Though this approach sounds messy, this approximation works well for some systems and the energy term is incredibly easy to compute. This functional does show the high level of parameterization used in the construction of DFT, and reminds one of the "semi-empirical vs. *ab initio*" argument in which some members of the density functional community engage.

*Example Functionals: GVWN, GPW92*

**Generalized Gradient Approximation (GGA) -** Where LDA can over-bind, the generalized gradient approximation (GGA) functionals tend to perform better. This method allows for a semi-local calculation to be made that accounts for density fluctuations better. This class of functionals adds a dependence on the gradient of the density, or the first derivative of the electronic density. The new exchange energy is computed as follows.

$$E_{xc}^{GGA}[\rho(\vec{r})] = \int \rho(\vec{r})\epsilon_{xc}\big[\rho(\vec{r}), s(\vec{r})\big] d\vec{r}$$
$$s(\vec{r}) = \left|\frac{\Delta\rho(\vec{r})}{2K_F\rho(\vec{r})}\right| \tag{3.5}$$
$$\epsilon_{xc}[\rho(\vec{r}), s(\vec{r})] = \epsilon_{xc}^{LDA}[\rho(\vec{r})] + \Delta\epsilon_{xc}\left[\frac{|\Delta\rho(\vec{r})|}{\rho^{4/3}(\vec{r})}\right]$$

GGA functionals include a higher order correction term, however it does not necessarily correlate to better performance. GGA and LDA have a similar level of physical description, and are used with regard to the specific system requirements.

*Example Functionals: BLYP, PBE*

**Meta-GGA -** Meta-GGA are similar to GGA functionals an the added dependence on the second derivative of the electronic density (or the Laplacian). In general, these functionals include a dependence on the non-interacting kinetic energy density ($\tau$).

$$E_{xc}^{mGGA}[\rho(\vec{r})] = \int \rho(\vec{r})\epsilon_{xc}\big[\rho(\vec{r}), \nabla\rho(\vec{r}), \tau(\vec{r})\big] d\vec{r}$$
$$\tau(\vec{r}) \propto \nabla^2\rho(\vec{r}) \tag{3.6}$$
$$\tau(\vec{r}) = \sum_i^{occ} \frac{1}{2}|\nabla\psi_i(\vec{r})|^2$$

*Example Functionals: TPSS, VSXC*

**Occupied Orbital-Dependent Functionals -** The simplest example of this fourth rung functional class is the hybrid exchange (XC) functionals.[57,58] In functionals that calculate exact exchange, the XC functional depends on occupied orbitals.

$$E_x^{exact} = -\sum_{i<j} \langle ij|ij \rangle$$

$$\langle ij|ij \rangle = \int \psi_i^*(\vec{r_1})\psi_j(\vec{r_1})\frac{1}{|\vec{r_1} - \vec{r_2}|}\psi_j^*(\vec{r_2})\psi_i(\vec{r_2})d\vec{r_1}d\vec{r_2} \tag{3.7}$$

A common hybrid functional, PBE0, has the following hybridization ($a_x = 0.25$):

$$E_x = a_x E_x^{exact} + (1 - a_x)E_x^{PBE} \tag{3.8}$$

*Example Functionals: PBE0, B3LYP*

**Virtual Orbital Dependent Functionals -** Including the virtual orbitals within the functional offers a clearer description of dispersion effects and improves the accuracy for transition state calculations. The only well established type of this functional so far are the double-hybrid functionals which combine exact exchange and MP2 correlation, two approaches where the XC functional depends on either the occupied or virtual orbitals, respectively. An example MP2 correlation energy could be described as follows,

$$E_c^{MP2} = -\frac{1}{4}\sum_{i<j}^{occ}\sum_{a<b}^{virt}\frac{|(ij|ab) - (ia|jb)|^2}{\epsilon_a + \epsilon_b - \epsilon_i - \epsilon_j} \tag{3.9}$$

and the double-hybrid DFT correlation energy could be calculated according to the following equation.

$$E_c = a_c E_c^{MP2} + (1 - a_c)E_c^{GGA} \tag{3.10}$$

### 3.1.2 DFT Today

While executing a DFT calculation, one is given many choices to best describe the system in question. One may choose an exchange-correlation functional (the main categories of which

are described above), a basis set (which can affect convergence time much more than in an HF calculation, and many applications necessitate specific basis sets), and an integration grid (where one can fit a set of fewest possible points to integrate over while fully describing their system, while many exchange functionals require a specific grid density). It gets quite complicated very quickly! Much of the focus of computational chemistry as a whole is related to DFT in: developing functionals, developing basis sets, developing approximations to simplify calculations, expanding existing approximations to more fully describe a system, etc. DFT serves today as a platform that goes well beyond the toolkit developed by Kohn and Sham, to include excited states and real-time dynamics via a perturbative method, time-dependant density functional theory (TD-DFT).[59–63]

## 3.2 Density Functional Tight Binding (DFTB)

There exists in the world of computation an ever growing need for electronic description of a bulk material, pulling scientists between the world of force fields (FF) or molecular mechanics (MM) to describe large systems efficiently, and density functional theory (DFT) or *ab initio* methods to describe the electronic properties. Within this gap of efficiency and physical description lies the domain of semi-empirical methods which approximate and parameterize higher order calculations to reasonably describe larger systems. Density functional based tight binding (DFTB) theory is a simplification of Kohn-Sham DFT to a tight binding formalism which allows for near DFT accuracy with a CPU cost about three orders of magnitude lower than traditional DFT.[64] This group focuses on DFTB as implemented in the open-source platform DFTB+.[65]

### 3.2.1 Mathematical Formalism

Density functional based tight-binding (DFTB) is derived from a simplification of Kohn-Sham density functional theory (DFT) to a tight binding form, allowing for a less compu-

tationally complex semi-empirical method for applications with large systems and longer time-scales.[66,67]

The total energy functional of Kohn-Sham (KS) DFT is expanded with respect to a chosen reference density ($\rho_0$) that is calculated from a superposition of neutral atomic densities.[68] The ground state (GS) density is then represented as this approximated density perturbed as shown below.

$$\rho(\vec{r}) = \rho_0(\vec{r}) + \delta\rho(\vec{r}) \tag{3.11}$$

A Taylor expansion is then applied to the total energy expression up to the third order as follows, where $V^{xc}$ and $E^{xc}$ are the exchange correlation potential and energy. The below equation describes the three levels of expansion that have been used to describe DFTB at the third order, however one can decompose the following equations into the non-self-consistent DFTB1 ($E^0 + E^1$), and second order self-consistent DFTB2 ($E^0 + E^1 + E^2$) as well.

$$E^{DFTB3}[\rho_0 + \delta\rho] = E^0[\rho_0] + E^1[\rho_0, \delta\rho] + E^2[\rho_0, (\delta\rho)^2] + E^3[\rho_0, (\delta\rho)^3]$$

$$E^0[\rho_0] = \frac{1}{2}\sum_{AB}\frac{Z_A Z_B}{R_{AB}} - \frac{1}{2}\iint\frac{\rho_0(\vec{r})\rho_0(\vec{r'})}{|\vec{r}-\vec{r'}|}d\vec{r}d\vec{r'} - \int V^{xc}[\rho_0]\rho_0(\vec{r}d\vec{r} + E^{xc}[\rho_0])$$

$$E^1[\rho_0, \delta\rho] = \sum_i n_i < \psi_i|\hat{H}[\rho_0]|\psi_i > \tag{3.12}$$

$$E^2[\rho_0, (\delta\rho)^2] = \frac{1}{2}\iint\left(\frac{1}{|\vec{r}-\vec{r'}|} + \frac{\delta^2 E^{xc}[\rho_0]}{\delta\rho(\vec{r})\delta\rho(\vec{r'})}\bigg|_{\rho_0}\right)\delta\rho(\vec{r})\delta\rho(\vec{r'}d\vec{r}d\vec{r'}$$

$$E^3[\rho_0, (\delta\rho)^3] = \frac{1}{6}\iiint\frac{\delta^3 E^{xc}[\rho]}{\delta\rho(\vec{r})\delta\rho(\vec{r'}\delta\rho(\vec{r''})}\bigg|_{\rho_0} X\delta\rho(\vec{r})\delta\rho(\vec{r'})\delta\rho(\vec{r''})d\vec{r}d\vec{r'}d\vec{r''}$$

Standard second-order DFTB therefore takes the KS-DFT total energy represented as a functional of charge density $\rho(\vec{r})$,

$$E_{DFT} = \sum_i^{occ}\left\langle\Psi_i\middle| - V_{ext} + \frac{1}{2}\int{}'\frac{n(\vec{r'})}{|\vec{r}-\vec{r'}|}\middle|\Psi_i\right\rangle + E_{XC}[n(\vec{r})] + \frac{1}{2}\sum_{\alpha,\beta}^{N}\frac{Z_\alpha Z_\beta}{|\vec{R}_\alpha\vec{R}_\beta|} \tag{3.13}$$

and simplifies the above expression so that it is solely dependent upon charge density fluctuations, $\Delta q$.

$$E_{DFTB} = \sum_i^{occ}\left\langle\Psi_i\middle|\hat{H}_0\middle|\Psi_i\right\rangle + \frac{1}{2}\sum_{\alpha,\beta}^{N}\gamma_{\alpha\beta}\Delta q_\alpha\Delta q_\beta + E_{rep} \tag{3.14}$$

42

The Hamiltonian is constructed from optimized MO coefficients, and diagonalization of the corresponding matrix provides the density fluctuation, $\delta\rho(r)$. The reference density is perturbed by this density fluctuation, calculating the total density as the sum of these values as per Equation 3.11.

Both $E^0$ and $E^{rep}$ are calculated from the reference density, the former resulting from a summation over the occupied orbitals with their corresponding eigenvalues, thereby constructing the Hamiltonian matrix under a two-center approximation. The latter term, $E^{rep}$ approximates the remaining Coulomb and exchange-correlation contributions with atom centered potentials. $E^{\gamma}$ represents the charge transfer between two atomic centers, with the net atomic charge derived from Mulliken charges related to the density. $E^{\omega}$ is a spin polarization term, utilizing the Mulliken spin population of each shell.

## 3.2.2   Self Consistent Charge (SCC)

The time independent Schrodinger equation is modified in all Hartree-Fock (HF) and DFT based methods to approximate the Hamiltonian as a sum of single-electron operators.

$$H^{SCC} = \sum_{i=1}^{n} \hat{f}(r_i) \tag{3.15}$$

The wavefunction therefore is a single determinant over the spin orbitals, $\sigma(s)$ and summation of the MO, $\Psi_i(r)$ expanded in a finite basis, $\Phi_\mu$.

$$\Psi_k^{SCC} = det[X_i(r_j, s_j)]$$

$$X_i(r, s) = \Psi_i(r)\sigma(s) \tag{3.16}$$

$$\Psi_i(r) = \sum_{\mu}^{N} C_{\mu i}\phi_\mu(r)$$

Because the Hamiltonian depends on the wavefunction, the resulting Schrodinger equation is nonlinear and must be iteratively converged. The MO coefficient matrix $(C_{\mu i})$ is used at each iteration to build a new Fock matrix $(F)$, and the MO's corresponding to the

lowest energy are filled. A nonlinear eigenproblem is therefore proposed, relating the MO coefficient matrix ($C$) multiplied by the overlap matrix ($S$) and energy of the system ($\epsilon$) to this optimized value $FC$ to some threshold ($\tau$).

$$FC^{NEW} = SC^{NEW}\epsilon$$
$$C^0 \rightarrow F^1$$
$$F^1C^1 = SC^1\epsilon \tag{3.17}$$
$$C^n \rightarrow F^{n+1}$$
$$\mid C^n - C^{n+1} \mid < \tau$$

Both the reference density and corresponding perturbations are calculated from the Hamiltonian, which is constructed from MO's resulting from the linear combination of atomic orbitals (LCAO). These MO coefficients are optimized via self-consistent charge (SCC) calculations that impose approximations upon the Schrodinger equation.

$$\hat{H}^{SCC}\Psi_k^{SCC} = E_k^{SCC}\Psi_k^{SCC}$$

A visual unpacking of the SCC routine is discussed in subsection 5.1.2.

### 3.2.3 Parameterization of DFTB Hamiltonians

DFTB is based on a number of approximations. First, the method is based on a valence-only minimal basis set of atomic orbitals (AO) which are used to construct the molecular orbitals (MO), and by extension, the wavefunction.

$$\psi_i = c_{\mu i}\phi_\mu \tag{3.18}$$

These AO are explicitly computed from DFT by solving the KS equations in a confining potential.

$$\left[ -\frac{1}{2}\nabla^2 + V^{eff}[\rho^{atom}] + \frac{r}{r_0}^n \right]\phi_\mu = \epsilon_\mu\phi_\mu \tag{3.19}$$

Because of this, the approximated atom-centered orbitals are slightly compressed to better describe bonding situations.

Additionally, a two-center approximation is applied to the Hamiltonian operator $\hat{H}[\rho_0]$, where:

$$\langle\phi_\mu|\hat{H}[\rho_0]|\phi_\nu\rangle \approx \langle\phi_\mu| - \frac{1}{2}\nabla^2 + V[\rho_A + \rho_B]|\phi_\nu\rangle, \qquad \mu\epsilon A, \nu\epsilon B \tag{3.20}$$

This leads to a direct neglect of three center terms and pseudo-potential contributions such that the inter-atomic forces are calculated pairwise across atomic pseudo-dimers. These pairwise interactions are calculated according to inter-atomic distance by Slater-Koster combination rules, therefore the Hamiltonian is calculated according to atomic pair calculations of Slater-Koster equations. These pairwise interactions are pretabulated and stored in repositories to form the AO basis of DFTB.

Finally, DFTB calculates the total reference energy, $E^0[\rho_0]$, using only the reference density. This is constructed with parameterized repulsive energy terms that apply to the atomic pairs within the systems geometry.

$$E^0[\rho_0] \approx E_{rep} = \frac{1}{2}\sum_{AB} V_{AB}^{rep} \tag{3.21}$$

This means that this method has a high transferability of parameters in the sense that the reference energy is independent of chemical environment, and a thorough description of a reference system can be applied to many other environments. These terms of $E_{rep}$ are pretabulated using DTF calculations or experimental data.

### 3.2.4 Applications

Due in part to the high parameterization of DFTB, it is an extremely memory efficient electronic structure method that allows calculations of large complexes with the average processing power of a standard laptop CPU. Additionally, DFTB as implemented in the software package DFTB+ 19.1 is an open source platform allowing free download and user control for tweaks to the standard software. This makes DFTB+ an incredibly accessible

option for many researchers, where bypassing a paywall or need for external processing power can afford detailed electronic description to researchers regardless of individual laboratory or university funding streams. Memory efficiency allows for a desktop calculation of large biomolecules, bulk materials, and molecular dynamic simulations of organic catalysts. To demonstrate this, a small sampling of recent publications have been selected that show the tunability of DFTB in terms of breadth of application.

## Materials Science

Depletion of fossil fuels has necessitated renewable energy sources, leading to increased research in the fields of solar devices. The sun is a resource that is effectively limitless and free of pollution, therefore photovoltaic devices constitute a commonly studied class of material. Although most current photovoltaic devices are silicon based, titanium dioxide derivatives are a valuable platform material for the development of dye-sensitized solar cells.[69,70] Titanium dioxide materials are somewhat limited in their pure structure by an intrinsic band-gap of 3eV, where photonic absorption is restricted to the ultraviolet range. Therefore, band-gap engineering, surface functionalization and doping have been a crucial element of this field. Titanium dioxide materials containing defects often have smaller band-gaps, leading to increased solar absorption. Additionally, doping titanium dioxide materials with transition metals can enhance photocatalytic activity. Furthermore, semiconductor materials like titanium dioxide can be synthesized into quantum dots (QD) or nanoparticles, small several-hundred-atom clusters that increase photon absorption via a phenomenon called "quantum confinement" when the size of the particle is small compared to the wavelength of an electron. Titanium dioxide QD alone have been used in a variety of applications, including photovoltaics, lasers, biomedical applications, and photocatalysts. DFTB is an attractive tool for studying such materials, as several hundred atoms is usually the approximate size of QD, and can model bulk defects and heterogeneous materials reasonably well.

DFTB has been useful in nanomaterials research beyond renewable energy applications.[71]

Nanotubes formed from boron nitrides (BNNTs) have been studied experimentally since their discovery in the 1990's due to their promise as gas sensors, drug delivery hosts, and gas storage matrices.[72] BNNT's like titanium dioxide derivatives perform differently if doped, or synthesised in specific dimensions. DFTB has been used to characterize gas adsorption efficiency of pristine and functionalized BNNTs, showing a calculable effect to the Fermi level of devices functionalized with amines.

**Biochemistry**

As materials science has developed, so too has the interest in nanomaterials in biomedical fields. Carbon nanotubes have proven to be biocompatable and widely useful, and modifications or coatings of these structures with biomolecules have revealed a host of applications like targeted cancer therapy, drug delivery, bioimaging and bone tissue repair. As many biochemists say, form equals function, so understanding how these biomaterials interact with targeted proteins is often a question of how they might preferentially fit into or around a specific residue. This could often be a question best suited for molecular mechanics, however this form of calculation will not describe fully the electronics of a biomaterial in great enough resolution to describe interactions at the scale of single electrons.[73,74]

DFTB is uniquely useful to this field of research in that it can speak to electronic effects of these larger molecules in a biological medium at greater electronic resolution than MM alone. DFTB+ itself has been used to characterize adsorption energies of boron nitride nanosheets, or white graphene, with different shapes to characterize how bonding affinity is affected by curvature of these materials.[75] These researchers were able to model the target residue and full nanosheets for their calculations, which would have been prohibitively expensive in full DFT.

Rhodopsins and other light harvesting biological complexes have been studied with TD-DFTB, and these calculations have shown to be in good agreement with more expensive TD-DFT calculations.[76] Kinases involved in signalling pathways related to immunity were

47

investigated with a number of MM methods and described electronically by DFTB.

**Excited States (ES)**

Perovskites are a class of material that has a specific crystal structure that is highly tunable, and construction of solar cells using these materials have proven interesting to researchers for being cost-effective, and their efficiency has skyrocketed in the recent decade.[77,78] Lead halide perovskites (LHPs) are attractive in the context of solar-cell applications and light emitting devices, thereby necessitating a full understanding of the excited state (ES) dynamics of these systems. When an LHP is photo-excited, charge carriers cause structural changes to the crystalline device which in turn affects the electronic state, resulting in the formation of polarons. To study these polarons one must model both electronic and structural degrees of freedom, which cannot be encapsulated by adiabatic MM or nonadiabatic classical path approximation methods. LHPs were computationally investigated with the fewest switches trajectory surface hopping (FSSH) method coupled with long range TD-DFTB (LR-TD-DFTB) to calculate the excitation energies, ES wavefunctions and nuclear forces.[79] For these long time-scale calculations, the researchers admitted that full DFT was impractical, and showed that the LR-TD-DFTB results agreed well with previous nonadiabatic DFT studies using a PBE functional. Using FSSH and LR-TD-DFTB these researchers were able to replicate experimental time scales for exciton dissociation, decay of carrier energy, and polaron formation.

TD-DFTB within DFTB+ has been benchmarked for GS and ES geometry optimizations of organic molecules, where photo-induced phenomena have previously been difficult to replicate over long timescales, or within an appropriate description of experimental systems including grafting support, embedding matrix, or solvent molecules.[45] A single chromophore description can be accomplished with TD-DFT assuming a molecular size equal to or smaller than about 100 atoms, however larger single compound studies are also out of reach. The precomputation by DFTB at the PBE level allows this semi-empirical method to

approximate full DFT as an eigenvalue problem of atomic charges, thereby describing charge transfer states even within the approximate framework. TD-DFTB can replicate TD-DFT in the calculation of vertical excitations, and the implementation of analytical gradients allows for for more correct ES geometry optimizations. Using common parameter sets *mio* and *3ob* these researchers calculated mean absolute error for ES bond length description and found that TD-DFTB outperformed PBE and B3LYP in description of CO bonds, and performed similarly to these higher level methods in describing CN and CC bonds. This in-depth study is one of the first to produce a side-by-side comparison between TD-DFTB and TD-DFT within DFTB+ for organic chromophores, and discusses potential pitfalls of unreliable parameterization. This study does however note that DFTB is not marked by systematic decrease of accuracy when moving from GS to ES calculations and provides clear pathways for researchers wishing to utilize this method for large scale chemical systems assessment.[80]

# Chapter Four

# TIME-INDEPENDENT DFTB (TI-DFTB 19.1)

## 4.1 Time-Independent Excited State Calculations

Excited state calculations are difficult to describe by single-determinant methods as they are inherently multireference in behavior. Previously described are a host of options to complete these calculations, however as stated they are hindered by their comparatively large computational cost when compared to analogous ground state (GS) calculations. There is therefore a gap in the computational chemist's toolkit - a method that is fast, affordable, and offers comparable accuracy to both the expensive excited state (ES) methods as well as the GS approaches. A method that offers ES solutions within the time-independent single-determinant GS method DFTB is described here. This method changes electron occupation patterns, deviating from the Aufbau principle that populates MO's according to ascending energy, and introducing analogous non-Aufbau occupancy within the existing SCC framework of DFTB. This allows for SCC relaxation of ES MOs within the time-independent framework of DFTB, allowing comparisons between GS and ES calculations to be made even-handedly (i.e. at the same level of mathematical description). These tools could prove incredibly useful for the researcher with many potential synthetic targets, or single particularly large synthetic

targets, or for the scientist who has to run calculations on a laptop. These accessible and cost efficient methods are implemented in the open source program DFTB+ for ultimate accessibility.

### 4.1.1 ΔDFTB

Minimization of the energy on each self-consistent charge (SCC) loop of a typical DFTB calculation drives the system to the global minimum of the the GS potential energy surface based on Aufbau occupation rules. To implement ES calculations, a new bias must be introduced where one or more electrons are promoted to a virtual orbital at each SCC iteration, thereby simulating a pseudo ES. These newly described electrons are not optimized after such artificial promotions however, as the occupation of the vacated orbital remains implied and relaxation of the lower molecular orbitals (MO) into the vacant space is prohibited. Additionally, the promoted electron feels the effect of the other electrons in the GS optimized molecular orbitals, and this can more accurately describe an N+1 system. In these ways, orthogonalized single-reference ES methods are restricted in application by their inability to relax the MOs in response to excitation, therefore increasing the error in situations like charge-transfer states where relaxation alters the electron configuration of the ES significantly.

ΔDFTB harnesses the power of the SCC loop allowing slight relaxation of imposed ES.[37] The Kohn-Sham (section 3.1) spin orbitals are self-constantly optimized under non-Aufbau constraints, emphasizing the highest occupied molecular orbital (HOMO) to lowest unoccupied molecular orbital (LUMO) transitions by selecting the KS orbital based on the character of the singlet ES. This method has been shown to accurately describe ES of large systems with extreme efficiency,[38] cutting down computational cost significantly and making these advanced calculations more accessible to the research community at large.

**Theory**

The ES density ($\rho_e$) is calculated according to Equation 4.1.

$$\rho_e(r) = \sum_{\sigma} \sum_{i \epsilon occ(\sigma)} \mid \phi_i^{\sigma}(r) \mid^2 \tag{4.1}$$

but because the constraint is placed on the spin orbitals rather than the MO's, this method introduces heavy spin contamination to the system by arbitrary promotion of $\alpha$ spin electrons.

Performing a non-Aufbau calculation manipulates the electronic filling to emulate a singlet ES. Because of this strict bias towards the alpha spin channel, the simple calculation resulting from the promotion of an alpha electron to the LUMO of the system does not describe a pure singlet state. The issue arises due to the quantum entanglement of a singlet ES system, whereby alpha and beta electrons have equal probability of promotion by the theoretical incoming photon. This inconsistency is not immediately apparent in DFTB as the electronic structure is approximated as an electronic density, a description that treats mixed and pure states on equal footing. However, because the singlet ES Hamiltonian is more correctly described as a composite quantum system, $H_\alpha \otimes H_\beta$ where the subscript indicates the spin of the promoted electron, isolating $H_\alpha$ only describes a partial trace of the full pure quantum state.

This issue is circumvented by application of the Ziegler sum rule (Equation 4.2), whereby the triplet state energy is subtracted from twice the mixed singlet state energy.[81–85]

$$E(S_1) = 2E[\{\phi_i^\sigma\}_m] - E[\{\phi_i^\sigma\}_t] \tag{4.2}$$

This approximates the span of the full Hilbert space defined by the singlet ES by artificially imposing the composite type nature of the pure state. In practice this requires two separate DFTB calculations, one of an artificially promoted alpha electron in the alpha spin channel to emulate the mixed state, and one of a beta electron promotion to the alpha spin channel

to describe a triplet (Figure 4.2). This doubles the calculation time, however within a tight-binding framework scaling by a factor of two still massively outpaces standard time-dependent approaches.

## 4.1.2 Code Description

Preliminary programming efforts for $\Delta$DFTB were implemented in DFTB+ 1.2 and were vetted against $\Delta$SCF, TD-DFT and TD-DFTB.[38] This study showed great promise for the $\Delta$DFTB model as the RMS error of vertical excitation energies for a small test set of molecules calculated in $\Delta$DFTB (0.82) rivaled that of TD-DFT using the common PBE functional (0.51). Furthermore, $\Delta$DFTB outperformed $\Delta$SCF (PBE/6-311+G*) when calculating vertical excitation energies of large organic dyes (RMS error of 0.64 versus 0.71 respectively). Since this publication, DFTB+ has undergone tremendous updates, the meat of the calculations moving from a linear type main file to a network of subdirectories. The current working version of this program is DFTB+ 19.1, and its tremendously different structure has made direct transfer of the original coding efforts impossible. Where previous versions of DFTB+ manipulated the dense MO coefficient matrix (HSqrReal) as a universally intact and callable array, the current program transfers these values between multiple overwritten arrays.

It is sensible perhaps to wish to avoid excess memory allocation to such a potentially large dense array, however the murky definition of the MO coefficients throughout the program makes direct implementation of $\Delta$DFTB and MOM derivatives incredibly challenging. Without an intact MO coefficient matrix, the published upon $\Delta$DFTB method, which in the past directly reordered the columns of HSqrReal, cannot be achieved. A new method involving direct reordering of the eigenvalues communicates the alternate electron populations of $\Delta$DFTB to an electron filling vector, an overview of which is described in the flowchart in Figure 4.1, and described below.
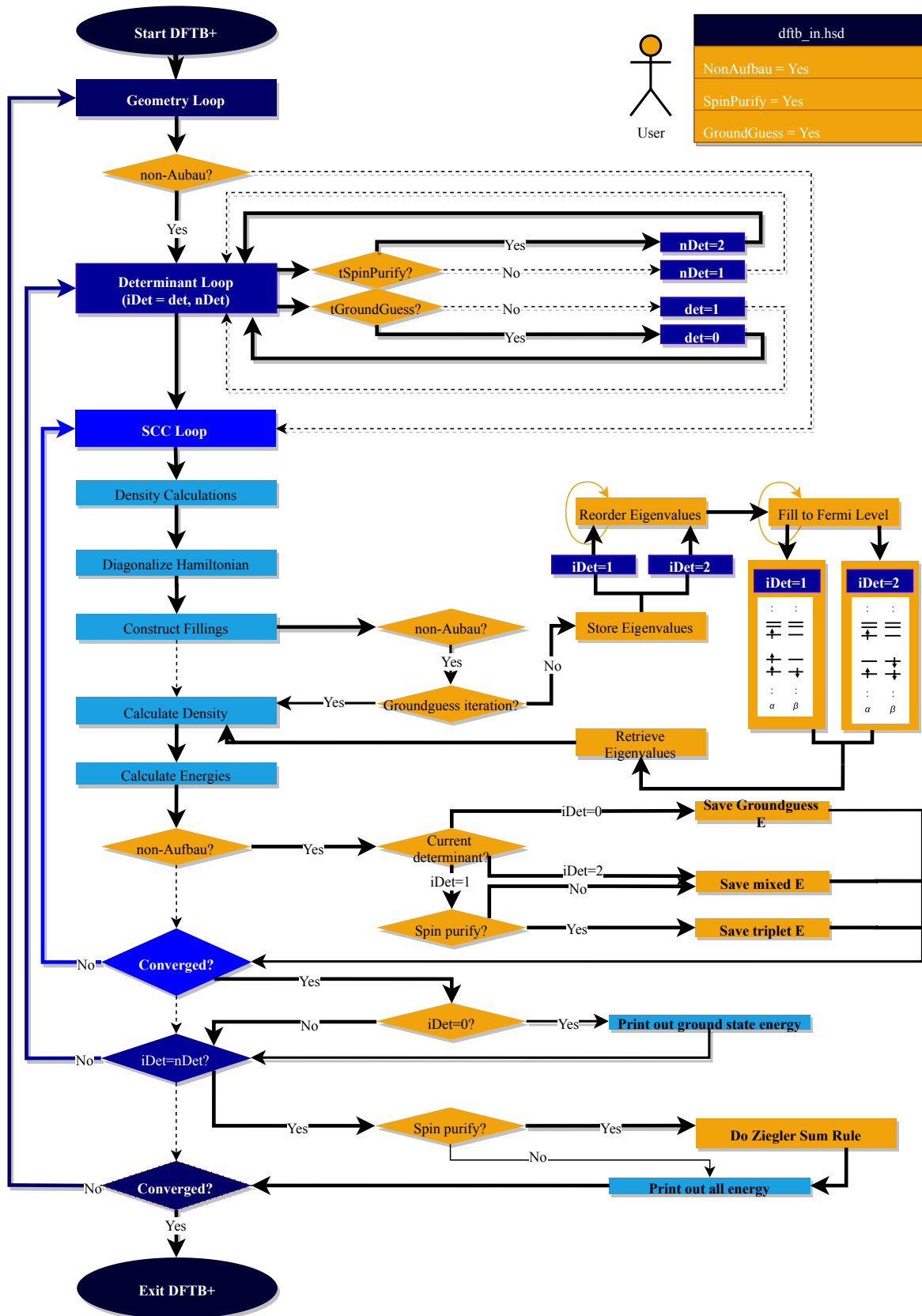
**Figure 4.1** ΔDFTB flowchart mapping calculation with Spin-Purify (nDet=2) and Ground-Guess (det=0). Determinant Loop counts iDet from det (0) to nDet (2) for a total of three iterations.

## The Determinant Loop

To do a $\Delta$DFTB calculation one must harness the SCC loop to run twice per geometry step, once for the mixed- and once for the triplet-state. $\Delta$DFTB in DFTB+ 1.2 managed calculation of both states within the linear format of the most current version of the code, however that double calculation was impossible to do in the newer version of the code using the "goto" statement previously implemented. A third loop was introduced to the main subroutine of DFTB+ 19.1 called the determinant loop, or lpDets, that encompasses the SCC loop entirely (see Figure 4.1 for approximate placement). This loop runs a tunable number of times over the SCC loop using its iteration number (0 for ground, 1 for triplet, or 2 for mixed) as an indicator of which state is being calculated. In the input file the user has the option for spin purification of their Non-Aufbau calculation, though this option is automatically set to true. In the event that the user does not want spin purification and to simply calculate a singlet state with mixed properties, the determinant loop only cycles once calculating the mixed state energy. At the end of each determinant loop the current SCC optimized energy is saved according to which state is being calculated, and once both states have converged the program applies the Ziegler sum rule to these saved energies and updates the total energy of the system. This newer version of the program has been run in tandem with its previous implementation in 1.2 and is able to replicate previously calculated energies of example molecules.

```
1    ! TI-DFTB Determinant Loop
2    ! Will pass though once if unless specified in input
3      lpDets : do iDet = det, nDet
4        call processGeometry(env, iGeoStep, iLatGeoStep, tWriteRestart,
             tStopDriver, tStopScc,&
5            & tExitGeoOpt)
6        if (tGroundGuess .and. iDet==0) then
7          call printEnergies(energy, TS, electronicSolver, tDefinedFreeE,
               tNonAufbau, tSpinPurify, tGroundGuess, iDet, &
8                            & tTDM, tiTransitionDipoleMoment)
9        end if
10       if (iDet .ne. 0) then
11         call postprocessDerivs(derivs, conAtom, conVec, tLatOpt,
               totalLatDeriv, extLatDerivs,&
12             & normOrigLatVec, tLatOptFixAng, tLatOptFixLen,
                 tLatOptIsotropic, constrLatDerivs)
13       end if
14       if (iDet == nDet) then
15         exit lpDets
16       end if
17     end do lpDets
```

**Listing 4.1** TI-DFTB determinant loop.

The determinant loop, as outlined in Listing 4.1 encompasses **processGeometry**, the subroutine responsible for the SCC cycle and necessary pre-initialization and post-analysis of the necessary variables. Minor modifications were necessary to override certain algorithmic steps within this subroutine that could not be called multiple times. Within this loop a call was also implemented to print the current energy of the ground state if the necessary calls were implemented by the user. The triplet- and mixed-state derivatives were spin purified manually. This loop is variable in nature, as it can be set to cycle through the ground state, triplet-state, and mixed-state consecutively or any number of those options in that order.

That as been arranged to be totally controlled by the input of the user.

**The Filling Swap**

As stated, the previous version of $\Delta$DFTB implemented in DFTB+ 1.2 directly modified the column arrangement in HSqrReal, therefore reordering the eigenvectors of the system to simulate the Non-Aufbau electron arrangement. As current modifications must sidestep this interaction with HSqrReal, a different and perhaps more direct rout to mimic the triplet and mixed ES was followed by manipulating the values of the array called *filling*. *Filling* is a three dimensional array with information about the system's electron occupation, k-point, and electron spin. It is a simple array consisting of ones and zeros to denote electron occupancy of the MO corresponding to the first dimensions index. Although it could not be directly modified, *filling* was manipulated through the temporary reordering of a single dimension of the *eigenvals* array which contains the eigenvalues (or MO energies) of each SCC iteration. A temporary array called *swapfill* was used to achieve this reorganization for the ease of the compiler.
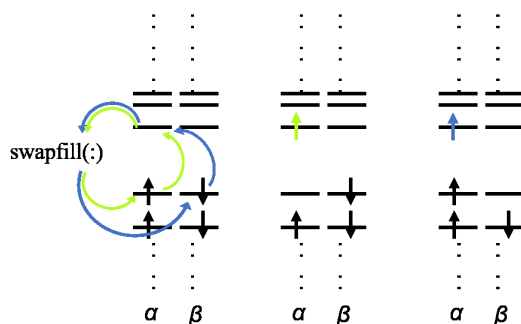


**Figure 4.2** Visualization of $\Delta$DFTB non-Aufbau filling routine: mixed state in green, triplet state in blue.

This may seem nonsensically arduous when working only in ones and zeros, however harsh numerical assignment was avoided whenever possible for both ease for the compiler as well as readability. Additionally, this arrangement allows this method to be easily expanded to work in temperature modulated filling calculations in the future.

Manipulating the fillings by way of an eigenvalue reorganization is a new approach to implementing Non-Aufbau electron populations, and is a cleaner version of the previous approach. Additionally, it automatically provides a clean output for the band.out file generated by the calculation, allowing the user to see an accurate description of the electron population of the ES system. This interface is also specifically useful in tandem with the maximum overlap method, described in section 4.2.

The primary benefit of this change was that in previously manipulating MO coefficient matrices directly, there was a huge drain on the CPU efficiency for which DFTB+ is praised. Large three dimensional matrix manipulation requires temporary matrices, populated with double precision variables that if allocated, populated, deallocated, reallocated, repopulated, etc. each SCC cycle can cause memory "loss" near 8% of the total DFTB+ routine for molecules of around 20 atoms. The current system of reordering the eigenvalues directly, and temporarily, allows reordering of one-dimensional vectors.

```fortran
if (tNonAufbau) then
  do iSpin = 1, size(eigenvals, dim=3)
    do i = 1, kpts
      if (iDet == 1 .and. tSpinPurify .and. iS==1) then
        eigenvals(int(nEl(iS))+1,i,iSpin)=eigenvals(int(nEl(iS)),i,
            iSpin)
      else if (iDet == 1 .and. tSpinPurify .and. iS==2) then
        eigenvals(int(nEl(iS)), i, iSpin)=eigenvals(int(nEl(iS)) + 1,
            i, iSpin)
      else if (iS==1 .and. iDet/=0) then
        swapFill = eigenvals(int(nEl(iS)) + 1, iSpin, iSpin)
        eigenvals(int(nEl(iS))+1,iSpin,iSpin)=eigenvals(int(nEl(iS)),
            iSpin,iSpin)
        eigenvals(int(nEl(iS)), iSpin, iSpin)  = swapFill
```

**Listing 4.2** TI-DFTB Non-Aufbau filling routine fragment. Not shown: the eigenvalues are saved, and then reordered in a non-Aufbau filling pattern.

Listing 4.3 shows how the program iteratively populates the *fillings* vector up to the Fermi level (as seen on line 4 of Listing 4.3).

```fortran
do iSpin = 1, size(eigenvals, dim=3)
  do i = 1, kpts
    do j = 1, size(eigenvals, dim=1)
      x = (eigenvals(j, i, iSpin) - Ef) / kT
#:if EXP_TRAP
      if (x > mExpArg) then
        filling(j, i, iSpin) = 0.0_dp
      else
        filling(j, i, iSpin) = 1.0_dp / (1.0_dp + exp(x))
      endif
#:else
      filling(j, i, iSpin) = 1.0_dp / (1.0_dp + exp(x))
#:endif
      if (tNonAufbau .and. j/=1) then
        if ( ((filling(max(j-1,1), i, iSpin)+filling(j-1, i, iSpin))
             ) <= elecTol) then
          exit
        end if
      else if (filling(j, i, iSpin)<=elecTol .and. .not. tNonAufbau)
           then
      if (filling(j, i, iSpin) <= elecTol) then
        exit
      end if
      ...
      Eband(iSpin) = Eband(iSpin) &
           & + kWeights(i) * (filling(j, i, iSpin) * eigenvals(j, i,
             iSpin))
```

**Listing 4.3** Portion of *filling* population routine with example TI-DFTB logic.

**The Ground Guess**

The previous code included a "ground-guess" functionality, allowing the user to toggle an optional SCC calculation according to the GS of their system when convergence of the ES was difficult. In the newest version of the code it is explicitly stated that the old eigenvectors be deallocated before beginning the next cycle of the determinant loop, so while this function no longer aids convergence it was reinstated as it offers a clear way for users to quickly know the vertical excitation energy of their system at the current geometry. This functionality was added by introducing a variable in the new determinant loop, allowing the loop to start from zero instead of one (the usual indicator of the triplet state calculation). When the variable "det" is set to zero, it carries through the following logic to run past any alternate filling logic, therefore allowing an SCC energy calculation of an Aufbau system to commence. This effort can be summarized by noting the logic present in line 11 of Listing 4.2, and inferring that a similar thread of logic was passed throughout the code.

The program then prints out the energy of the GS guess at the end of the ground state SCC calculation, and saves that information for output in the clean reading at the end of the calculation. A user can see with this option the mixed-, triplet-, ground-state and spin purified energies of their system.

## 4.2   Maximum Overlap Convergence Strategies

Though $\Delta$DFTB is a good tool for systems with well defined local minima corresponding to their first ES, many systems have very low lying virtual orbitals that become nearly degenerate near conical intersections. Calculations of the ES energy can be confused by the oscillation between two similar solutions, and collapse to the GS is common for molecules with low lying virtual orbitals. Calculating very low level ES can be nearly impossible under standard non-Aufbau occupation procedures when plagued by this phenomena called variational collapse, when the optimization of some slightly higher energy solution can cause

the calculation to fall into the global minimum of the energy landscape. Degenerate or nearly degenerate HOMO and LUMO are common in large or highly conjugated systems, therefore making calculations of examples like organic chromophores difficult to converge.[86]

To alleviate these convergence issues, the maximum overlap method (MOM) was proposed which redefines the SCC energy calculation to hold more tightly to a prescribed electronic structure and lessens the probability of collapsing into the global minimum of the GS. MOM has been expanded to multiple variations including the initial maximum overlap method (IMOM) and decision augmented diagonalization (DAD). These as well as the original MOM are described below.

**Formalism in DFTB**

DFTB is a single determinant approach, and as stated in chapter 3.2 the wavefunction is approximated by a sum of single-electron operators.

$$\hat{H}^{SCC} = \sum_{i=1}^{n} \hat{f}(r_i) \tag{4.3}$$

The eigenfunctions of these new equations are single determinants

$$\Psi_k^{SCF} = det[\chi_i(r_j, s_j)] \tag{4.4}$$

and each spin-orbital $(\chi_i = \psi_i(r)\sigma(s))$ has a molecular orbital component $(\psi_i)$ described by a linear combination of atomic orbitals $(\phi_\mu)$.

$$\psi_i(r) = \sum_{\mu}^{N} C_{\mu i}\phi_\mu(r) \tag{4.5}$$

Because of this, on each iteration when the molecular orbital matrix $(\mathbf{C}_{\mu i})$ is built, the eigenvectors of the wavefunction are uniquely described. The atomic orbitals are described by the finite AO basis as prescribed by choice of Slater-Koster files, therefore these MO coefficients are the descriptive force in defining a unique system's electronic space. These

eigenfunctions and their eigenvalues correspond to the molecular orbitals and orbital energies of the system respectively. As these values change, so does the Hilbert space of the electronic structure of the system. At its core, this electronic space is what the SCC pathway of DFTB is optimizing along a lowest energy pathway.

$$FC^{NEW} = SC^{NEW}\epsilon \tag{4.6}$$

In forcing minimization of the energy ($\epsilon$) the calculation can be driven towards the global minimum of the PES, and incorrectly bypass a desired local minimum, a phenomenon termed variational collapse. In $\Delta$DFTB occupation is forced into either a mixed- or triplet-state scheme, however if there are two nearly degenerate ES this can force the calculation to bounce between the similar electronic structures and inhibit convergence.

What the maximum overlap formalism does to offset this involves using the subspace of the system's Hilbert space defined by electronic occupation. This method uses the eigen-vectors described by the molecular orbital coefficients to define a space onto which future spaces are projected, thereby informing occupation of subsequent iterations.

## 4.2.1 Maximum Overlap Method (MOM)

The maximum overlap method is in essence an alternative population scheme. Instead of forcing excitation into the LUMO on each $\Delta$DFTB cycle, MOM populates the current SCC iteration MO's according to those that have the largest projection onto the span of the previously occupied space, driving energy calculations influenced by some informed initial guess.[87]

$$FC^N = OC^N\epsilon$$
$$O^{MOM} = (C^{N-1})^{\ddagger}SC^N \tag{4.7}$$

The SCC equation is modified so that the basis function overlap matrix ($\mathbf{S}$) is used to build a new overlap matrix ($\mathbf{O}$) which is constructed by multiplying the transpose of the

previous **C** matrix onto the product of **S** and the current MO's (Equation 4.7.) This retains the information of the past SCC cycle, and allows iterative population of molecular orbitals according to how similar they were to the previous iteration. The projection ($p_j$) of each new MO onto its equivalent from the last SCC iteration is calculated by the absolute value of the summation over the rows of this calculated **O** matrix (Equation 4.8.)

$$p_j = \left( \sum_i (O_{ij})^2 \right)^{\frac{1}{2}} \tag{4.8}$$

This vector now holds the information of which MO's overlap the most strongly with the MOs form the previous iteration, and population of the MO's in the current cycle are filled in descending projection (compare to ascending energy for Aufbau). This method does not always populate the prescribed MO filling pattern, however it can help guide the calculation by retaining the shape of the originally described electron density.[88] When paired with a $\Delta$DFTB calculation, SCC cycles following the initial energy definition of either a mixed or triplet state will hold more true to that initial guess, and keep the calculation from collapsing in either promoted configuration.

## 4.2.2   Initial Maximum Overlap Method (IMOM)

Though implementation of MOM can be helpful relaxing ES, there are still circumstances where this method fails. This single determinant ES compatible relaxation algorithm still falls short in cases involving double excitations, charge-transfer states, and near canonical intersections, therefore the equation has been slightly modified in a newer approach called the initial maximum overlap method (IMOM).[89] This method works under the same rules governed by MOM, however instead of populating the new MO's in accordance to their projection over the previously occupied space, IMOM populates MO's according to their projection over the space occupied by the initial guess.

$$FC^N = OC^N \epsilon$$
$$O^{IMOM} = (C^0)^{\ddagger} SC^N \tag{4.9}$$

The calculation continues in the same way as traditional MOM, building a projection vector using $\mathbf{O}^{IMOM}$ as $\mathbf{O}_{ij}$ in Equation 4.8. This modification is helpful in cases where even MOM descends on the energy landscape too quickly as shown in Figure 4.3, and is a good tool to probe very low level ES given a strong enough initial guess.
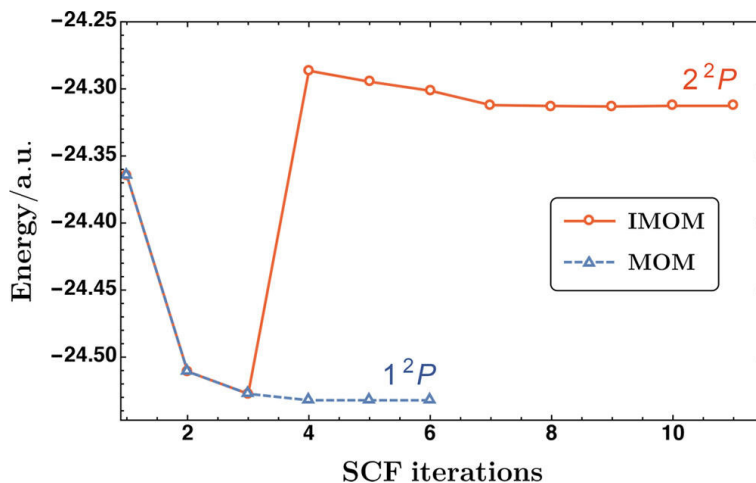


**Figure 4.3** Visualization of IMOM converging to the desired state where MOM fails. Reprinted with permission from Giuseppe M. J. Barca, Andrew T. B. Gilbert, and Peter M. W. Gill. *Journal of Chemical Theory and Computation* **2018** 14 (3), 1501-1509. DOI: 10.1021/acs.jctc.7b00994. Copyright 2020 American Chemical Society.

When pairing IMOM with $\Delta$DFTB, it can help hold the electron configuration closer to the initial mixed or triplet state definition when these states exhibit near degeneracies with the GS or the opposing spin-state.

## 4.2.3   Decision Augmented Diagonalization (DAD)

Because the energy landscape is an inherently difficult surface to probe, decision augmented diagonalization (DAD) was introduced to provide flexibility in these convergence strategies. Like IMOM, DAD is again directly comparable to MOM and seemed a natural extension of development once IMOM had been implemented in the electronic structure package DFTB+. This method (both created and hilariously named by our group) allows the user to select which SCC iteration they would like to project upon in cases where the initial guess is too

high, and quick relaxation is useful for a specific number of cycles before maximum overlap type restrictions slow descent along the energy surface. This choice of iteration is denoted by $K$ in Equation 4.10.

$$FC^N = OC^N \epsilon$$
$$O^{DAD} = (C^K)^{\ddagger} SC^N \tag{4.10}$$

This also affords flexibility to the user and gives them greater access to the energy landscape of their system, affording the possibility of probing many different ES solutions.

### 4.2.4   Code Description

The logical architecture of MOM and IMOM is shown in Listing 4.4, and DAD in Listing 4.5. The general flow of these calculations can be found in Figure 4.4.

```
1     !> If MOM
2     if (tMOMo) then
3       if(iSccIter>1) then
4         tMOM = .true.
5       endif
6       tTImat=.true.
7     endif
8     !> If IMOM
9     if (tIMOM) then
10      if(iSccIter>1) then
11        tMOM = .true.
12      endif
13      if (iSccIter==1) then
14        tTImat=.true.
15      endif
16    endif
```

**Listing 4.4** TI-DFTB MOM logic to alter $\Delta$DFTB determinant loop. Variable *tMOM* initiates projection subroutine and variable *tTImat* saves previous MO coefficients.
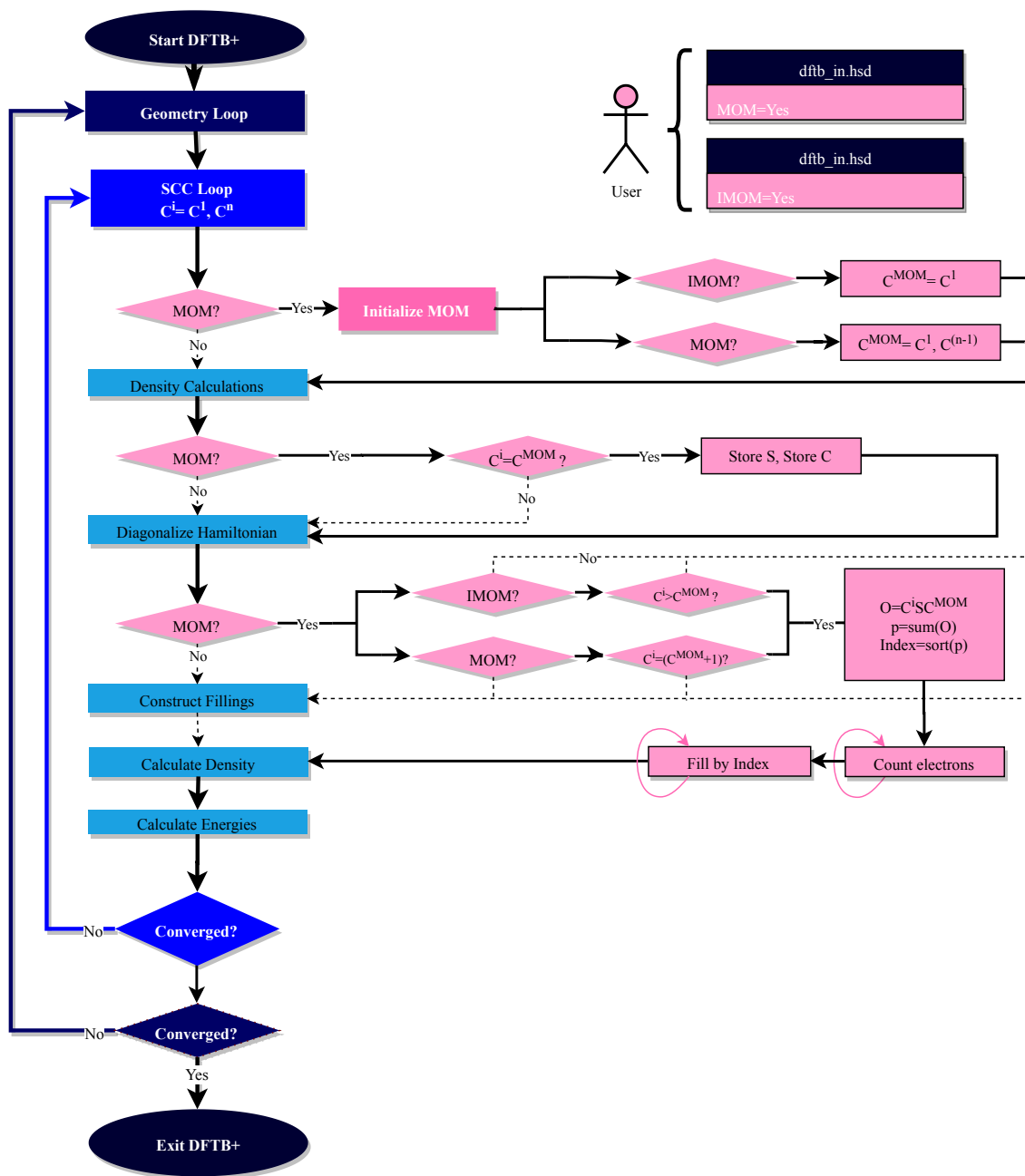
**Figure 4.4** MOM and IMOM flowchart mapping treatment of fillings. DAD would follow the IMOM architecture and simply change $C^{MOM} = C^K$ where the user may choose value of $K$. Works with $\Delta$DFTB with options for user to specify determinant for which they wish to perform maximum overlap.

```fortran
1    !> If DAD
2    if (iDADt .ne. 0) then
3      if (iDADt<iSccIter .and. iDet==1) then
4        tMOM=.true.
5      endif
6      if (iDADt==iSccIter .and. iDet==1) then
7        tTImat=.true.
8      endif
9    endif
10   if (iDADm .ne. 0) then
11     if (iDADm<iSccIter .and. iDet==2) then
12       tMOM=.true.
13     endif
14     if (iDADm==iSccIter .and. iDet==2) then
15       tTImat=.true.
16     endif
17   endif
```

**Listing 4.5** TI-DFTB DAD logic to alter $\Delta$DFTB determinant loop. DAD is both determinant (*iDet*) and SCC iteration (*iSccIter*) dependant. Variable *tMOM* initiates projection subroutine and variable *tTImat* saves previous MO coefficients.

The logical structure of MOM, IMOM and DAD was an important piece of the architecture of this platform. Many iterations of this method were attempted, but what is reported in Listing 4.4 and Listing 4.5 were the least variable and memory intensive structure that we could devise. The logical *tMOM* toggles multiple subroutines that prepare the MO coefficient and overlap matrices for direct input into an overlap calculation, and is used to call for the eventual overlap matrix calculation, projection vector creation, and filling alteration that the MOM, IMOM or DAD user defines. The variable *tTImat* is the signal that causes a cascade of temporary variable allocation to hold these values for as short a time as possible. Great care taken to not over allocate-memory to holding these many dense MO coefficient matrices.

Listing 4.6 shows a small portion of the overlap calculation, where the overlap matrix, $O$, is formed by the multiplication of the current MO coefficient matrix ($C$) and whatever previous eigenvectors the user defines ($pC$).

```
1    O = matmul(S,C)
2    temp = matmul(transpose(pC),O)
3    do ia=1,na
4      O(:,ia)=abs(temp(:,ia))*filling(:)
5    enddo
6    pr = sum(O,dim=1)
7    call index_heap_sort(p, pr)
```

**Listing 4.6** Excerpt of TI-DFTB I/MOM and DAD overlap matrix ($O$) routine. Variables $C$ and $pC$ are imported dense MO coefficients of the prescribed SCC iteration. Output variable $p$ is the projection vector that alters the electron occupation.

The overlap matrix is multiplied by a filling vector that corresponds to the spin-dependant electronic fillings of the previous SCC iteration. Because $O$ is a square matrix, this operation zeros out columns of $O$ that were previously unoccupied, but does not disallow transition to previously unoccupied MO as this information is still stored in the rows of the matrix. This step was added as many of the highest level virtual orbitals remained as fixed as the lowest occupied orbitals, and there was an unnatural weighting of electrons promoted to high level virtual orbitals. This method seemed to temper that proclivity of the algorithm slightly while still allowing for alternate filling patterns.

Electronic filling directly followed the $\Delta$DFTB filling logic as in Listing 4.3. Listing 4.7 shows the necessary programming in its entirety. The projection vector $pMOM$ holds orbital indices in order of ascending projection, and this is used to reorder the binary filling indices according to maximum overlap with the defined previous space.

```fortran
if (tMom) then
  allocate(tmpMtx1(size(filling, dim=1)))
  call index_heap_sort(tmpMtx1, filling(:,1,1))
  do iSpin = 1, size(eigenvals, dim=3)
    do i = 1, kpts
      do j = 1, size(eigenvals, dim=1)
        p=tmpMtx1(j)
        m=pMom(j, iS)
        tmpMtx(m, i, iSpin)=filling(p,i,iSpin)
      end do
    end do
  end do
  filling=tmpMtx
end if
```

**Listing 4.7** TI-DFTB I/MOM and DAD filling routine.

# Chapter Five

# TRANSITION DIPOLE MOMENTS IN TI-DFTB 19.1

Transition dipole moments (TDM) of electronic transitions and their associated oscillator strengths correlate to the lineshape of emission and absorption spectra.[90,91] The ability of electronic structure methods to predict these values allows for more precise UV/vis spectral prediction which is an invaluable tool for experimentalists. This feature is available in many computational methods that boast high physical description at albeit high computational cost, however as it is sightly complex the TDM calculation is lacking in many lower resolution methods.

Time-dependent density functional theory (TD-DFT) is currently the most popular computational method for adiabatic description of electronic excitation due to its favorable cost to accuracy ratio.[92] TD-DFT calculates excited states via a time-dependant approach. This means that the ground-state electronic structure is fully described and perturbed with a sweep of simulated photons. The program reads which wavelength produces a linear response from the ground-state wavefunction. It then proceeds to describe the virtual states based entirely off of the derived energy gap, meaning that the full wavefunctions of the excited states are not described in this method. This approximation paired with the variety of available functionals leads to potentially substantial disagreement of predicted electronic

transitions.

Furthermore, this approach relies exclusively on the quality of the functional form used to describe the electronic density of the system. As a formally exact method, TD-DFT advocates need only await the elusive "perfect" density functional to correctly describe all systems in nature. As this has not yet been developed, a game of fitting functionals to specific inputs plagues the DFT community with inconsistencies. Newer functionals have not shown themselves to necessarily outperform older ones, and there are large variations in the performance of the group as a whole. As many of the available functionals are highly parameterized, there exist theoretical or conceptually complicated systems for which no experimental data is available. This method scales $O(N^3)$ and quickly becomes overwhelming for regularly accessible technology, requiring an incredible amount of memory as molecular systems exceed the 100 electron point.[93,94]

Equation of motion coupled-cluster singles and doubles (EOM-CCSD) provides a valuable alternative. This method has proven itself to be very accurate, and as a coupled-cluster calculation it has the option to be improved by expanding the range of allowed excitations.[95] There is no limiting factor like the functional choice in TD-DFT, however this method is very computationally expensive, scaling $O(N^6)$. This method is therefore limited to very small systems in the absence of a large scale computing facility.

In the age of functionalized materials and nanostructures, a more complete description of extended systems is imperative. Development of a time-independent density functional tight-binding (TI-DFTB) excited state approach is being actively pursued by this lab, and one of the functionalities of this method is dynamic TDM calculation. The tight binding approximation of density functional theory introduces higher parameterization and drastically reduced computational cost. The extension of this method to include full excited-state wavefunction description allows for direct transition information to be obtained, something that is lacking in perturbation type methods like TD-DFT.

## 5.1 The Hilbert Spaces Defined by TI-DFTB

A natural benefit to the aforementioned time-independent methodology is the even-handed treatment of the ground state (GS) and excited state (ES), allowing transition information to be interpreted directly. Linear response methods like TD-DFT, as well as configuration integration methods result in a series of allowed excitation energies and some series of coefficients that quantify each amplitude's contribution to the ES space. This, if paired with chemical intuition, can help answer the question of which electron is excited and where does it go, however the output system "orbitals" lack qualitative description and physical significance on their own. They are represented with X and Y vectors for TD-DFT, and CI coefficients in CI approaches.

In $\Delta$DFTB the GS and ES molecular orbitals are variationally described to the same level of accuracy, and the two spaces are defined under an identical treatment. The eigenvectors that would generally define the space of the GS are captured by $\Delta$DFTB and forced to relax into the ES. This treatment allows for an orbital response to excitation. When an electron is excited from the HOMO to the LUMO, the now de-occupied HOMO will relax slightly, and be described by a different spatial orientation as well as density. This same logic extends to all of the occupied orbitals below the HOMO, and to a lesser extent the virtual orbitals as well. Therefore, the MO space of the GS and ES will be intentionally different - and a higher level of physical description is offered beyond simply approximating the energy of the virtual orbital from the GS calculation.

In understanding the transition between these spaces one must capture the eigenvectors defining the space of the GS and the ES. These vectors form the bases of the subspaces in question, and as previously stated they define different physical spaces. In order to compare these subspaces one must make them mutually orthogonal. This is accomplished in this method by the corresponding orbital transformation (section 5.3), an extension of singular value decomposition (section 5.2). To rationalise this approach to the calculation of TDM,

let's step through a typical GS dipole moment calculation in DFTB.

## 5.1.1  Single State Dipole Moment Formalism and Requirements

The dipole moment is calculated by applying the dipole moment operator ($\hat{\mu}$) to the GS wavefunction ($\Psi_g$). The $\hat{\mu}$ operator for a molecule is composed of nuclear and electronic components. For example, $\hat{\mu}_e$ is the sum over electronic charges multiplied by their respective position operators, and $\hat{\mu}_N$ behaves analogously. Therefore, Equation 5.1 defines the GS dipole moment operator $\hat{\mu}$.

$$\hat{\mu} = \hat{\mu}_N + \hat{\mu}_e$$
$$\hat{\mu} = \sum_A Z_a \hat{R}_A - \sum_i \hat{r}_i \qquad (5.1)$$
$$\mu_{gg} = \langle \Psi_g | \hat{\mu} | \Psi_g \rangle$$

For an $n$ electron system, the GS dipole moment evaluation $\mu_{gg}$ can be represented as an integration over all electronic degrees of freedom of the GS wavefunction acted upon by the $\hat{\mu}$ operator.

$$\int \Psi_g(\vec{r_1}, \ldots, \vec{r_n}) \cdot \hat{\mu} \cdot \Psi_g^*(\vec{r_1}, \ldots, \vec{r_n}) dr_1 \ldots dr_n \qquad (5.2)$$

The integrals needed to evaluate Equation 5.2 are pretabulated in DFTB as a part of the parameterization, therefore this is a relatively simple calculation for one to request. The meat of this calculation lies in the construction of $\Psi_g$, which interestingly is never directly referenced in the DFTB+ program. Instead, the wavefunction is approximated as a Slater determinant over one electron wavefunctions as below.

$$\boldsymbol{det} \begin{bmatrix} \phi_1(\vec{r_1}) & \dots & \phi_1(\vec{r_n}) \\ \vdots & \ddots & \vdots \\ \phi_n(\vec{r_1}) & \dots & \phi_n(\vec{r_n}) \end{bmatrix}$$ 

$$\phi_i = \sum_\mu C_{i\mu} X_\mu$$

(5.3)

The column vectors of $\mathbf{C}$ form an orthogonal basis for the GS MO, where:

$$\langle i|j \rangle = \delta_{ij}$$

(5.4)

Equation 5.4 will be proven in the following section. The MO coefficients are used to calculate the Mulliken population of electrons on each atomic center. The population matrix $P_{\mu\nu}$ is calculated as described in Equation 5.5, and relies on the orthogonality of the MO vectors. The density matrix, $D_{\mu\nu}$ is calculated from the MO coefficient matrix, and $S_{\mu\nu}$ is the overlap matrix of the AO basis functions.

$$P_{\mu\nu} = D_{\mu\nu} S_{\mu\nu}$$

$$D_{\mu\nu} = 2 \sum_i C_{\mu i} C_{\nu i}^*$$

(5.5)

In Equation 5.5, the construction of $D_{\mu\nu}$ is a typical probability density according to the quantum mechanical postulate that one can relate it to the amplitude of the wavefunction squared, here represented in terms of the coefficients defining the MO in the AO basis. If the wavefunction (or the MO basis) is not orthogonal these probabilities can be distorted due to spatial overlap. Furthermore, these spaces need also to be normalized so that the sum of probabilities adds to one. DFTB constructs single electron Kohn-Sham-like molecular orbitals, therefore these orbitals are forced to obey these postulates and each $\mathbf{C}_{\mu\nu}$ is composed of orthonormal column vectors.

Once the charge density is used to construct the populations on each atomic center, $P_{\mu\nu}$ is summed over to calculate the charges. These are used to assign single orbital charges at each atomic center to calculate the dipole moment in DFTB.

$$\mu = \sum_A \Delta q_A R_A \tag{5.6}$$

## 5.1.2 Visualizing the SCC Pathway

Due to the stipulation that each LCAO molecular orbital vector must remain orthogonal to the other vectors in the set, the relaxation of the MO space in the SCC pathway looks like a rotating and twisting set of vectors that always remain perpendicular to their neighbors. This twisting is represented in Figure 5.1, where a selection of MO coefficients from a triplet-state $N_2$ relaxation is depicted. The MO coefficient matrix of the beta spin channel of a triplet state relaxation for $N_2$ is shown below for the first couple of SCC iterations in the final geometry step.

$$(Step\,1)\quad \mathbf{C}: \begin{matrix}
0.56 & 0.62 & 0.00 & 0.00 & 0.32 & 0.00 & 0.00 & -0.71 \\
0.09 & -0.20 & -0.08 & -0.53 & -0.35 & -0.55 & 0.31 & -0.53 \\
0.09 & -0.20 & -0.42 & 0.33 & -0.35 & 0.54 & 0.32 & -0.53 \\
0.09 & -0.20 & 0.50 & 0.20 & -0.35 & 0.00 & -0.63 & -0.53 \\
0.56 & -0.62 & 0.00 & 0.00 & 0.32 & 0.00 & 0.00 & 0.71 \\
-0.09 & -0.20 & -0.08 & -0.53 & 0.35 & \mathbf{0.55} & \mathbf{-0.31} & \mathbf{-0.53} \\
-0.09 & -0.20 & -0.42 & 0.33 & 0.35 & \mathbf{-0.54} & \mathbf{-0.32} & \mathbf{-0.53} \\
-0.09 & -0.20 & 0.50 & 0.20 & 0.35 & \mathbf{0.00} & \mathbf{0.63} & \mathbf{-0.53}
\end{matrix}$$

$$(Step\,2)\quad \mathbf{C}: \begin{matrix}
0.56 & 0.62 & 0.00 & 0.00 & 0.32 & 0.00 & 0.00 & -0.71 \\
0.09 & -0.20 & 0.26 & -0.47 & -0.35 & -0.55 & -0.30 & -0.53 \\
0.09 & -0.20 & -0.54 & 0.00 & -0.35 & 0.02 & 0.63 & -0.53 \\
0.09 & -0.20 & 0.27 & 0.46 & -0.35 & 0.54 & -0.33 & -0.53 \\
0.56 & -0.62 & 0.00 & 0.00 & 0.32 & 0.00 & 0.00 & 0.71 \\
-0.09 & -0.20 & 0.26 & -0.47 & 0.35 & \mathbf{0.55} & \mathbf{0.30} & \mathbf{-0.53} \\
-0.09 & -0.20 & -0.54 & 0.00 & 0.35 & \mathbf{-0.02} & \mathbf{-0.63} & \mathbf{-0.53} \\
-0.09 & -0.20 & 0.27 & 0.46 & 0.35 & \mathbf{-0.54} & \mathbf{0.33} & \mathbf{-0.53}
\end{matrix}$$

$$\tag{5.7}$$

For the purpose of visualization one must move to three-space, so to that end let us select the lower right indices depicted in bold in Equation 5.7 and construct two $3 \times 3$ matrices as in Equation 5.8. The $\mathbf{C}$ matrix from step one is used to construct $A$, and step two information is used to construct $B$. Let the columns of $A = [\vec{a_1}, \vec{a_2}, \vec{a_3}]$ and the columns of $B$ be defined

analogously to $A$.

$$A = \begin{bmatrix} 0.55 & -0.31 & -0.53 \\ -0.54 & -0.32 & -0.53 \\ 0.00 & 0.63 & -0.53 \end{bmatrix} B = \begin{bmatrix} 0.55 & 0.30 & -0.53 \\ -0.02 & -0.63 & -0.53 \\ -0.54 & 0.33 & -0.53 \end{bmatrix} \tag{5.8}$$

The column vectors of $A$ and $B$ are plotted in Figure 5.1. This figure depicts the transformation of $A \rightarrow B$, and as is shown this transformation is simply the negative (clockwise) rotation about the axis defined by $\vec{a_3}$ and $\vec{b_3}$, which in this example are identical. The four remaining vectors lie on a plane orthogonal to $\vec{a_3}$, and $\vec{a_1} \perp \vec{a_2}$ and $\vec{b_1} \perp \vec{b_2}$.

The vectors shown in Figure 5.1 represent the treatment of MO by DFTB in the SCC pathway. Each MO is represented by a column vector that is held orthogonal to all other MO vectors, and these vector spaces are rotated to correctly define the LCAO that describes the molecular orbitals of the system. In this example the space is simplified to be represented in three-space, or $\mathbb{R}^3$. Because this is real data, and only a subset of the overall matrix was selected, these vectors are only approximately normalized, however physical significance was not lost by being selective in this way. Physically the vectors shown above represent the contribution of the $3p$ atomic orbitals of each nitrogen to the $\pi^*$ molecular orbitals of $N_2$ for spin-down electrons. Selecting any identical $3 \times 3$ areas of the matrices depicted in Equation 5.7 will allow a similar visualization of AO contribution to MO space.

Hearkening back to Equation 5.4 in this new context, we can rewrite this equation as:

$$< \vec{a_i} | \vec{a_j} > = \delta_{ij} \tag{5.9}$$

This new equation is now simple to understand and visualize: The inner product of any vector, $\vec{a_i}$ is one if with itself and zero if with any other column vector of $A$. Now it has been settled that within any single SCC iteration the MO are orthogonal, and the inner product
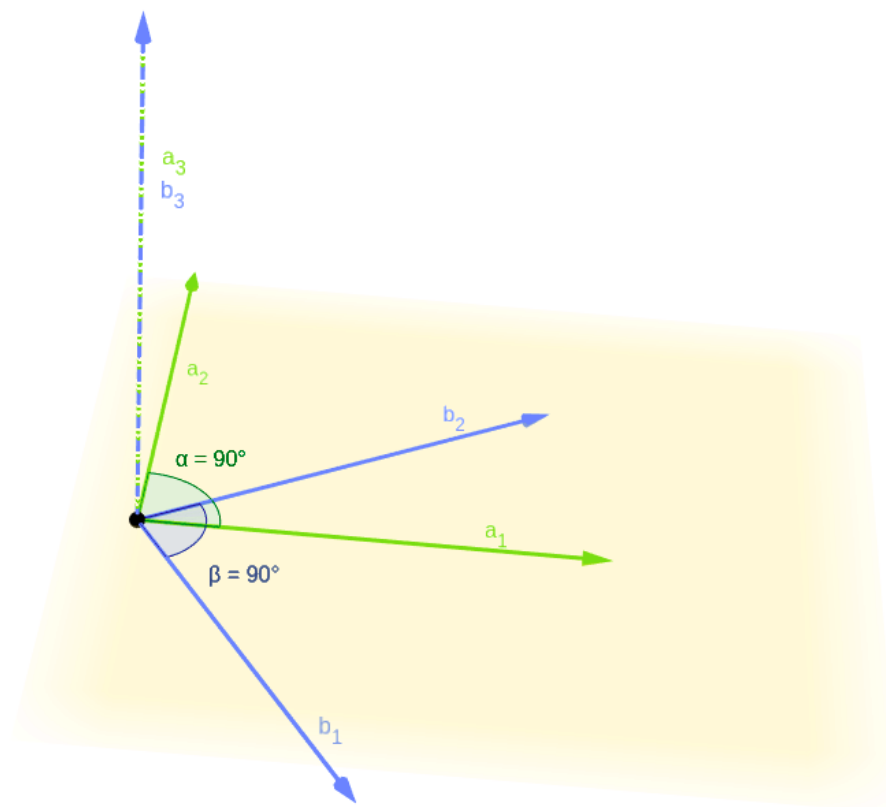
The columns of A and the columns of B are individually orthogonal, and differ by a $59^o$ rotation about $\vec{a_3}$ or $\vec{b_3}$

**Figure 5.1** SCC rotation of MO coefficients while maintaining orthogonality.

of that space with itself is identity. Thus it is visualized that the basis of the MO space defined by the columns of the MO coefficient matrix **C** from any one SCC iteration is an orthogonal basis.

However in this project we do not wish to compare the product of identical SCC pathways - we will be using entirely different states defined by many iterations of unique SCC manipulations. For simplicity, let us compare states different by only one SCC iteration.

What can be said about orthogonality of these spaces by comparing a column vector of $A$ ($\vec{a_i}$) with a column vector of $B$ ($\vec{b_j}$)? If $i = j = 3$ we have the desirable output that $\vec{a_3} \cdot \vec{b_3} = 1$, however if $i = j = 2$ then $\vec{a_2} \cdot \vec{b_2} = 0.31$, they are no longer identical because the

space rotated. Furthermore, if $i = 1$ and $j = 2$ then $\vec{a_1} \cdot \vec{b_2} = 0.50$, no longer zero as when the space rotated the columns of $A$ were not held orthogonal to the columns of $B$. Therefore, the inner product of $A$ and $B$ is not identity. Not only are the diagonal elements typically less than one, but there are non-zero off-diagonal elements to contend with as well. Let $\mathbb{M}$ represent this non-diagonal matrix.

$$\mathbb{M} = < \vec{a_i} | \vec{b_j} > \neq \delta_{ij} \tag{5.10}$$

Now it has been visualized that these two states are not necessarily mutually orthogonal. In this same way, the columns of the **C** matrices from a GS ($C_{GS}$) and ES ($C_{ES}$) $\Delta$DFTB calculation will also not be mutually orthogonal due to the rotations of the SCC routine. Let $i$ represent the columns of $C_{GS}$ and $\bar{i}$ represent the columns of $C_{GE}$.

$$\mathbb{M} = < \bar{i} | j > \neq \delta_{\bar{i}j} \tag{5.11}$$

In order to calculate a transition dipole moment in DFTB one must calculate the changing molecular charges according to Mulliken population analysis, as described by section 5.4. As stated in the previous section, calculating Mulliken populations is similar to calculating a probability density. Transition densities between the GS and ES MO spaces must rely on mutually orthonormal vector spaces in order to have any physical significance. Therefore, these two spaces will have to be rotated with respect to each other to offset the rotations of the SCC routine. In order to do this we will have to construct transformation matrices and apply them to these spaces. This process is called the corresponding orbital transformation (COT), and is closely related to singular value decomposition (SVD) - both of which are described below.

## 5.2 Singular Value Decomposition (SVD)

In linear algebra when one wishes to diagonalize a matrix $A$ they would factor it according to the general prescription $A = PDP^{-1}$. This form is useful in visualizing the eigenvalues (the diagonal matrix elements of $D$) and eigenvectors (the columns of $P$). The stipulation that $A$ be diagonalizable in this manner is that $A$ must be similar to a diagonal matrix, and that if $A$ is $n \times n$ it must have $n$ linearly independent eigenvectors. What this generally translates to is that $A$ must be composed of linearly independent column vectors.

Let the aforementioned theoretical matrix $A$ represent the specific matrix $A$ defined in Equation 5.8. $A$ is a portion of a molecular coefficient matrix, and has been shown to be composed of orthogonal column vectors, therefore linear independence is assured. Furthermore, it has been stated that any $\mathbf{C}$ matrix composed of Kohn-Sham MO coefficients will have mutually orthogonal column vectors. By this logic, all MO coefficient matrices will be diagonalizable according to this prescription. section 3.1 which describes the foundation of DFT (from which DFTB is derived) outlines that the MO coefficient matrix $\mathbf{C}$ is composed of the eigenvectors of the Fock matrix, $F$. The eigenvalues of $F$ relate to orbital energies.

Now let the theoretical $A$ be represented with $\mathbb{M}$ from Equation 5.10. Is this matrix necessarily diagonalizable? It certainly could be, but there is no assurance of linear independence in the overlap of two unique MO spaces. For this reason the $A = PDP^{-1}$ decomposition is not a suitable choice. Furthermore, the inverted matrix in that equation is quite computationally expensive to calculate.

Instead of $A = PDP^{-1}$ we use a related but more generalizable approach for this problem - singular value decomposition (SVD).[96,97] This approach factors a matrix $A$ according to Equation 5.12 into unitary transformation matrices $U$ and $V$ and a diagonal matrix $\Sigma$.[98] The superscript $T$ refers to the transpose of the matrix $V$.

$$A = U\Sigma V^T \tag{5.12}$$

Because $V$ is a unitary matrix, $V^{-1} = V^T$, and therefore expensive matrix inversion is

avoided. This method is often used in applied linear algebra in part due to this relationship, as well as its compatibility with rectangular matrices.

Let's dive into the composition of the diagonal matrix $\Sigma$. SVD is based on the property of eigenvectors and values that the absolute values of the eigenvalues ($|\lambda_1|$) measure the amount that a matrix $A$ will stretch or shrink its eigenvectors, $\vec{v_1}$, according to;

$$A\vec{v_i} = \lambda_i\vec{v_i} \tag{5.13}$$

Let $A$ be a rectangular ($m \times n$) matrix. $A^T A$ is symmetric. Let $\{\vec{v_1} \ldots \vec{v_n}\}$ be an orthonormal basis consisting of the eigenvectors of $A^T A$, and let $\{\lambda_1 \ldots \lambda_n\}$ be the associated eigenvalues.

Remembering that $\vec{v_i}$ is both a unit vector, and an eigenvector of $A^T A$, let us follow a derivation adapted from Lay 2003.[99]

$$
\begin{aligned}
||A\vec{v_i}||^2 &= (A\vec{v_i})^T A\vec{v_i} \\
&= \vec{v_i}^T A^T A\vec{v_i} \\
&= \vec{v_i}^T (\lambda_i\vec{v_i}) \\
&= \lambda_i
\end{aligned}
\tag{5.14}
$$

One can see that the eigenvalues of $A^T A$ are all non-negative. The elements ($\sigma_i$) which make up the diagonal indices of $\Sigma$ from Equation 5.12 are called **singular values**, and are the square root of the eigenvalues of $A^T A$ and are the lengths of the vectors $A\vec{v_i}$. These singular values are uniquely determined by $A$.

$$
\begin{aligned}
\sigma_i &= \sqrt{\lambda_i} \\
\sigma_i &= ||A\vec{v_i}||
\end{aligned}
\tag{5.15}
$$

Any process in which the factorization $A = U\Sigma V^T$ produces orthogonal $U$ and $V$, and diagonal entries in $\Sigma$ where $0 \leq \sigma_i$ is considered SVD. Although the diagonal entries of $\Sigma$ are necessarily the singular values of $A$, $A$ does not uniquely determine $U$ and $V$. The columns of $U$ are termed the **left singular vectors** of $A$ and the columns of $V$ are termed the **right**

**singular vectors** of $A$. The right singular vectors of $A$ are the orthogonal eigenvectors of $A^T A$, and the left singular values form an orthonormal basis that spans $\mathrm{Col}A$.

## 5.2.1   Example SVD Calculation

Our computational approach to evaluating TDMs through $\Delta$DFTB relies on SVD, so lets walk through an example SVD of $A$ described in Equation 5.8.

$$\mathbf{A} = \begin{bmatrix} \mathbf{0.55} & \mathbf{-0.31} & \mathbf{-0.53} \\ \mathbf{-0.54} & \mathbf{-0.32} & \mathbf{-0.53} \\ \mathbf{0.00} & \mathbf{0.63} & \mathbf{-0.53} \end{bmatrix} = \mathbf{U\Sigma V^{T}} \tag{5.16}$$

*Step One: Find the eigenvalues $A^T A$, then solve for singular values to create $\Sigma$-* After calculating $A^T A$ one has a symmetric matrix. This is significant because symmetric $n \times n$ matrices possess exactly $n$ eigenvectors, though they might not necessarily be distinct.[100] We will calculate the eigenvalues ($\lambda_i$) by finding the roots of the characteristic equation defined by $det(A^T A - k\mathbb{I}) = 0$. $\Sigma$ will be a diagonal matrix with the square roots of the eigenvalues (called the singular values) on the diagonal.

$$\mathbf{A^T A} = \begin{bmatrix} 0.594 & 0.002 & -0.005 \\ 0.002 & 0.595 & 0.000 \\ -0.005 & 0.000 & 0.843 \end{bmatrix}$$

$$\Lambda = \left\{ \lambda_1, \lambda_2, \lambda_3 \right\}$$
$$\Lambda = \left\{ 0.842,\ 0.592,\ 0.597 \right\} \tag{5.17}$$
$$\sigma_i = \sqrt{\lambda_i}$$
$$\Sigma = \mathbb{I} * \left[ \sigma_1, \sigma_2, \sigma_3 \right]$$
$$\mathbf{\Sigma} = \begin{bmatrix} 0.918 & 0 & 0 \\ 0 & 0.770 & 0 \\ 0 & 0 & 0.773 \end{bmatrix}$$

*Step Two: Determine the n orthogonal eigenvectors from the eigenvalues to create the right singular vectors, V* - Because $A^T A$ is symmetric, the $n$ distinct eigenvectors corresponding to the eigenvalues will be orthogonal to each other. Therefore the columns of $V$ will all be orthogonal. In our example, we solve for the eigenvectors $(\vec{v}_i)$ by solving $(A^T A)\vec{v}_i = \lambda_i \vec{v}_i$.

$$V = \left[ \vec{v}_1, \vec{v}_2, \vec{v}_3 \right]$$
$$\mathbf{V^T} = \begin{bmatrix} -0.021 & 0.000 & 1.000 \\ -0.804 & 0.594 & -0.017 \\ 0.594 & 0.804 & -0.013 \end{bmatrix} \tag{5.18}$$

*Step Three: Determine the left singular vectors, or the columns of U, by normalizing the vectors $A\vec{v}_i$* - Because $A^T A$ is symmetric, the eigenvectors of $A^T A$ are orthogonal. The basis $\mathcal{U} = \{A\vec{v}_1, \ldots, A\vec{v}_n\}$ is therefore an orthogonal basis for $\text{Col}A$, and normalising these vectors produces an orthonormal basis of $\text{Col}A$ composed of the eigenvectors of $AA^T$. The orthonormal basis vectors are used to construct $U$.

$$\vec{u_i} = \frac{1}{||A\vec{v_i}||} A\vec{v_i} = \frac{1}{\sigma_i} A\vec{v_i}$$

$$U = \left[ \vec{u_1}, \vec{u_2}, \vec{u_3} \right]$$

$$\mathbf{U} = \begin{bmatrix} -0.590 & -0.802 & 0.091 \\ -0.565 & 0.329 & -0.757 \\ -0.577 & 0.498 & 0.647 \end{bmatrix} \tag{5.19}$$

Now when we consider the matrix equation $U\Sigma V^T$, we can visualize describing $A$ as follows.

> *A grounding conceptual synopsis* - An orthonormal basis for Col$A$, or $U$, is stretched according to the singular values of $A$ which are calculated from the eigenvectors of $A^T A$. This space is then transformed by the transpose of the eigenvectors of $A^T A$, that is, $V$, which because $V$ is unitary (or composed of orthonormal vectors) is equivalent to the inverse of $V$.[101] Notice also that $V$ is an improper rotation matrix wit the generic form $\left( \begin{smallmatrix} \cos\theta & \sin\theta \\ \sin\theta & -\cos\theta \end{smallmatrix} \right)$ appearing in the lower left.

Figure 5.2 plots the columns of the matrices described by Equation 5.17 through Equation 5.19. In Figure 5.2a one can see that though the columns of $U$ span all of Col$A$ they are not identical vectors to the columns of $A$. Figure 5.2b shows how multiplying $U$ by $\Sigma$ alters the length of the vectors but not their span. This is consistent with fact that $\Sigma$ is a diagonal matrix. The statement that $V^T$ is a transformation matrix that brings about an improper rotation is demonstrated in Figure 5.2c. This figure shows the mapping of the previous vectors (in grey) onto $A$ (in red) by way of a reflection followed by a rotation.

Being familiar with the components of SVD will be essential to understand the following section on the corresponding orbital transformation. Much of this section was straightforward as we dealt with a symmetric matrix $A^T A$ - but does this system hold up if considering a non-
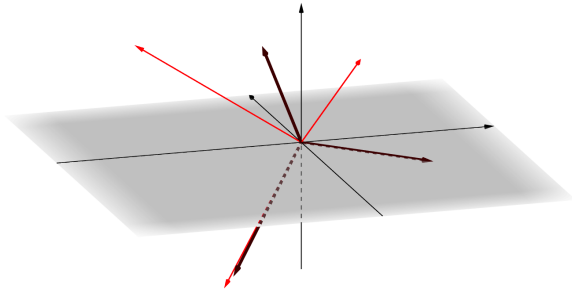
**(a)** Columns of $U$ shown in red, and columns of $A$ shown in black.
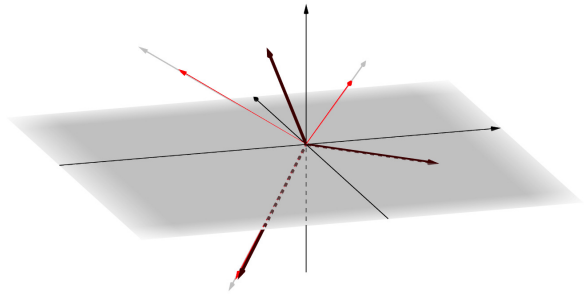
**(b)** Columns of $U\Sigma$ shown in red, columns of $A$ shown in black. Columns of $U$ in grey to show vector shrinkage with application of $\Sigma$.
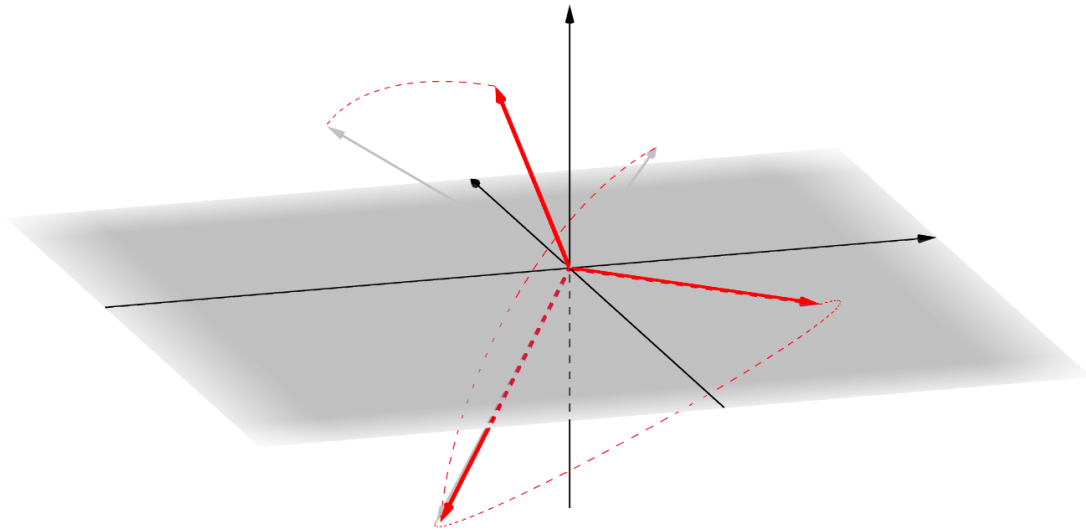


**(c)** $U\Sigma V^T$ shown in red, also shown in red with dashed lines is rotation from $U\Sigma$ onto $A = U\Sigma V^T$. Columns of $U\Sigma$ in grey to show rotation with application of $V^T$

**Figure 5.2** $A = U\Sigma V^T$ shown step-wise, where a shows $U \neq A$, b shows $U\Sigma$ is a shrinking transformation, and c shows $V^T$ is a rotation matrix and maps $V^T : U\Sigma \to A$.

symmetric matrix $A^T B$? Demonstration of the affirmative can be found in subsection 6.3.1 where a real data output from the TDM functionality of $\Delta$DFTB is shown as a proof of concept.

## 5.3   The Corresponding Orbital Transformation (COT)

A canonical orbital set is one that is composed of orthonormal orbital vectors, such as the MO coefficient matrices we have seen above. These types of canonical orbitals have the mathematical property of being spatially orthogonal and normalized. When faced with two sets of canonical orbitals that are not mutually orthogonal, one must transform these orbitals into a space where they are. These new orbitals will now also have a diagonal overlap, enabling calculations that can probe transitions between these spaces in a quantum mechanical framework. To transform canonical orbitals one must hold their wavefunction, $\Psi$ unaltered in order to retain physical significance. In single determinant methods, $\Psi$ has been defined as a determinant over occupied spin orbitals that are themselves canonical. Transforming canonical orbitals while holding the determinant $\Psi$ constant requires unitary transformations.

Unitary transformations $(\mathscr{U}_i)$ are those that hold the inner product constant. In this way, the original space is isomorphic to the transformed space, and the transformation itself is considered a bijective function in which each element of the first space maps directly to its pair in the transformed space. In chemical terms, we can define two sets of canonical orbitals ($\Phi_a$ and $\Phi_b$) as isomorphisms of themselves in such a way that that the transformed MO spaces ($\chi_a$ and $\chi_b$) have a diagonal spatial overlap integral ($\mathscr{T}$).[102]

$$\Phi_i \mathscr{U}_i = \chi_i$$

$$\mathscr{T}_{ab} = \langle \chi_a | \chi_b \rangle$$

$$= \int \chi_a^* \chi_b \mathrm{d}\tau \tag{5.20}$$

$$= \mathscr{T}_a \delta_{ab}$$

The isomorphisms $\chi_i$ are also canonical orbitals, and due to the relationship described in Equation 5.20 they are called **corresponding orbitals**.

These types of transformed orbitals have been used in a variety of applications including describing a subset of electrons as "froze" during large scale effective core potential calculations[103] and adsorbate-substrate chemisorbtion calculations,[104] as well as calculating magnetic coupling between spin-up and spin-down wavefunctions in broken-symmetry calculations.[105,106] The values along the diagonal of $\mathscr{T}$ have been related to particle-hole amplitudes of TD-DFT calculations[107] and identifying MO that are inherently closed-shell.[105] This method can be used in order to implement exciton models between excited monomers in a molecular cluster[108] and in solar cells,[109] and has been expanded upon to create Maximal Orbital Analysis which allows key aspects of chemical bonding from the relationship between the MO and AO of a given fragment.[110]

### 5.3.1 Corresponding Orbitals in Terms of SVD

Although any Hermitian matrix can be diagonalized by a unitary transformation, the overlap between matrices that are neither orthogonal nor identical is not generally Hermitian.

Let us follow the King 1967 derivation[111] and consider two wavefunctions, $\psi_a$ and $\psi_b$ as single Slater determinants over orbitals $i = a, b$ with a non-diagonal overlap matrix $\mathscr{A}$. $\mathscr{C}$ is an antisymmetrizing operator, a projection that forces systems to satisfy the Pauli

principle.[112]

$$a = \{a_1, \ldots, a_n\}$$

$$b = \{b_1, \ldots, b_n\}$$

$$\psi_a = \mathscr{C} |a_1(1), \ldots, a_n(n)| \tag{5.21}$$

$$\psi_b = \mathscr{C} |b_1(1), \ldots, b_n(n)|$$

$$\mathscr{A} = \int a^* b \, \mathrm{d}\tau$$

Our goal is to perform unitary transformations on the orbitals such that;

$$\hat{a} = aU$$

$$\hat{b} = bV \tag{5.22}$$

$$\int \hat{b}^* \hat{a} \, \mathrm{d}\tau = U^* \mathscr{A} V = \Sigma \delta_{\hat{a}\hat{b}}$$

where $\Sigma$ is a diagonal matrix. While the overlap matrix has been transformed into a diagonal matrix, the resulting wavefunctions will remain unchanged beyond stretching.

$$\psi_a = \det(U^*) \mathscr{C} |\hat{a}_1, \ldots, \hat{a}_n|$$
$$\tag{5.23}$$
$$\psi_b = \det(V^*) \mathscr{C} |\hat{b}_1, \ldots, \hat{b}_n|$$

Choosing the correct $U$ and $V$ looks very much like SVD. We define $V$ as composed of orthonormal eigenvectors of $\mathscr{A}^* \mathscr{A}$, such that $\mathscr{A}^* \mathscr{A} V = V \Lambda$. Solving for the eigenvalues, $\Lambda$ gives:

$$\Lambda = V^* \mathscr{A}^* \mathscr{A} V$$
$$\tag{5.24}$$
$$= (\mathscr{A} V)^* (\mathscr{A} V)$$

Because $\Lambda$ is diagonal, the columns of $\mathscr{A} V$ must be orthogonal, and the eigenvalues are positive as the squares of the indices of $\Lambda$. We can now use these values to construct a second unitary matrix $U$ such that;

$$U = \mathscr{A} V \Lambda^{1/2} \tag{5.25}$$

wherein $U$ is composed of the eigenvectors of $\mathscr{A}\mathscr{A}^*$. This definition indicates that the aforementioned procedure is necessarily symmetric with regards to $\psi_a$ and $\psi_b$. The previously unknown diagonal matrix, $\Sigma$, can therefore be derived as follows.

$$
\begin{aligned}
\Sigma &= U^* \mathscr{A} V \\
&= \Lambda^{1/2} V^* \mathscr{A}^* \mathscr{A} V \\
&= \Lambda^{1/2}
\end{aligned}
\tag{5.26}
$$

And thus the earlier prescription of the singular values has been procured, as well as the left and right singular vectors.

> Therefore, the products of SVD are chemically relevant spaces that can be used to re-orient the GS and ES produced by TI-DFTB to calculate TI-TDM.

## 5.3.2 Mathematical Formalism of COT in TI-DFTB

Let's first describe the vector-spaces obtained from TI-DFTB and SVD, and how they can be used. A generic $\Delta$DFTB calculation with a ground-state guess and spin purification describes the MO spaces of three distinct states: the GS, the triplet-state, and the mixed-state. For the remainder of this chapter we will refer to the SCC optimized GS MO coefficient matrix as $G$, and the optimized mixed-state MO coefficient matrix as $E$.

Once we calculate $G^T E = \mathbb{M}$ and perform SVD we have calculated $U$, $V$, and $\Sigma$. Because MO spaces are defined by orthonormal column vectors in the MO coefficient matrix, $G$ and $E$ are unitary matrices along with $U$ and $V$, such that:

$$
U^T U = G^T G = V^T V = E^T E = \mathbb{I}
\tag{5.27}
$$

(The transpose of these equations are also true.)

$\mathbb{M}$ and $\Sigma$ also possess intrinsic qualities that are useful. $\Sigma$ is a diagonal matrix such that;

$$\Sigma = \Sigma^T = \sigma_i \delta_{ij} \tag{5.28}$$

and contains the uniquely determined singular values of $\mathbb{M}$ which have already been linked to the stretching effect of an electronic transition section 5.2. Singular values close to unity indicate little change has occurred between the two calculations for a particular MO, and values significantly above or below unity will identify MO that have changed the most.[104] $\mathbb{M}$ is not necessarily unitary nor diagonal, however it can be related to the unitary matrices $U$ and $V$ as follows.[98]

$$\mathbb{M} = U\Sigma V^T$$
$$\mathbb{M}^T\mathbb{M} = (U\Sigma V^T)^T(U\Sigma V^T) = V\Sigma^T U^T U\Sigma V^T = V(\Sigma^T\Sigma)V^T = V\Sigma^2 V^T$$
$$\mathbb{M}\mathbb{M}^T = (U\Sigma V^T)(U\Sigma V^T)^T = U\Sigma V^T V\Sigma^T U^T = U(\Sigma\Sigma^T)U^T = U\Sigma^2 U^T$$
$$\tag{5.29}$$

In subsection 6.3.1 an example $U$ and $V$ are shown for an an excitation in $N_2$.

Equation 5.30 shows the mathematical basis of the assertion that; **two MO spaces that are not mutually orthogonal can be made mutually orthogonal by transforming the MO bases with the products of SVD.** Bearing in mind all that has been discussed in this chapter, this notion is perhaps not so difficult to believe. The effect of $U$, $V$ and $\Sigma$ are shown in Figure 5.2, and the unitary transformation matrices $U$ and $V$ were shown to have rotational properties. When comparing to the SCC operation visualized in Figure 5.1 it made intuitive sense that these unitary matrices contained information about the rotational transformations between the GS and ES. In subsection 6.3.1 an example $U$ and $V$ are shown for an an excitation in $N_2$, and in this more tangible example these rotational regions of these matrices are visible. COT assigns the left singular vectors of $\mathbb{M}$ to transform the left multiplied matrix used to form $\mathbb{M}$, and the same with the right singular vectors and matrix. By using these rotational matrices, one is able to redefine the MO spaces within a

## The Corresponding Orbital Transformation

Let the MO column vectors of $G = \left[a_1, \ldots, a_n\right]$ and $E = \left[\bar{a}_1, \ldots, \bar{a}_n\right]$, and the diagonal elements of $\Sigma = \left\{\sigma_1, \ldots, \sigma_n\right\}$ as per Equation 5.28. Let $\mathbb{M} = G^T E = U\Sigma V^T$ as per Equation 5.12, and $\mathbb{M}^T\mathbb{M} = V\Sigma^2 V^T$ as per Equation 5.29. Recall from Equation 5.4 that for mutually orthogonal bases $< i|j >= \delta_{ij}$.

$$\mathbb{M} = U\Sigma V^T$$

$$\mathbb{M}^T\mathbb{M} = \mathbb{M}^T U\Sigma V^T$$

$$V\Sigma^2 V^T = \mathbb{M}^T U\Sigma V^T$$

$$V\Sigma^2 V^T V = \mathbb{M}^T U\Sigma V^T V$$

$$V\Sigma^2 = (G^T E)^T U\Sigma$$

$$V\Sigma^2 = E^T G U\Sigma$$

$$V\Sigma = E^T G U$$

$$EV\Sigma = EE^T G U \tag{5.30}$$

$$EV\Sigma = GU$$

$$(EV)^T EV\Sigma = (EV)^T G U$$

$$\boldsymbol{\Sigma} = (\mathbf{EV})^{\mathbf{T}}\mathbf{GU}$$

$$\vdots$$

$$\left\langle a_i\middle|\hat{U} = \middle\langle i\right.$$

$$\left\langle \bar{a}_i\middle|\hat{V} = \middle\langle \bar{i}\right.$$

$$\boldsymbol{\Sigma} = \left\langle\mathbf{i}\middle|\bar{\mathbf{j}}\right\rangle = \sigma_{\mathbf{i}}\delta_{\mathbf{i}\bar{\mathbf{j}}}$$

mutually orthogonal basis to rectify the issue of non-orthogonality posed in Equation 5.11. Equation 5.30 shows that $U$ and $V$ can be interpreted as operators $\hat{U}$ and $\hat{V}$ that rotate the column vectors in $G$ and $E$ so that the spaces are mutually orthogonal.

90

## 5.4 TDM in TI-DFTB+

The MO coefficient matrices that have now been made orthogonal with COT must be used to evaluate the transition dipole moment. As per Equation 5.6, the permanent dipole moment is approximated as a summation of partial Mulliken charges on each atomic center. The wavefunctions are not used directly for this calculation as the MO described by the SCC routine of DFTB are auxiliary and have an inherently unknown relation to the true many-body wavefunction. The meaningful quantity from these MO is the electronic density in DFTB as well as DFT, in which a theoretical perfect functional exists wherein the wavefunction is perfectly described by this density. In Casida TD-DFTB (or linear response DFTB) one approximates the TDM by assigning individual orbitals with a transition charge at each atomic center. Here $\mathbf{C}$ is the GS MO coefficient matrix and $S$ is the AO overlap matrix.

$$\Delta q_{ia,A} = \frac{1}{2}\Big(\sum_{\mu \in A}\sum_{\nu} C_{\mu i}^{\ddagger} S_{\mu\nu} C_{\nu a} + C_{\nu i}^{\ddagger} S_{\nu\mu} C_{\mu a}\Big) \tag{5.31}$$

The charges, $\Delta q_{ia,A}$, are weighted by transition vectors from the linear response calculation.

How do TDM in TD-DFTB compare to the TI-DFTB procedure? Firstly, TI-DFTB is not a linear response method, therefore transition vectors are not calculated and cannot be used to weight the sum. The MO spaces from ES calculations in $\Delta$DFTB are optimized fully under SCC procedure, and as described above will need to be transformed by COT with respect to their GS analogues before direct comparison. Once transformed, however, the isomorphisms ($G'$ and $E'$) of the original MO spaces ($G$ and $E$) can be directly implemented in an analogous sum. $\Sigma$ is the diagonal overlap matrix between these states described by Equation 5.17.

$$\Delta q_{ia,A} = \frac{1}{2}\Big(\sum_{\mu \in A}\sum_{\nu}(G_{\mu i}')^{\ddagger}\Sigma_{\mu\nu}E_{\nu a}' + (G_{\nu i}')^{\ddagger}\Sigma_{\nu\mu}E_{\mu a}'\Big) \tag{5.32}$$

### 5.4.1 Code Description

Listing 5.1 shows an excerpt of the outermost TDM subroutine, nested within is the call for *tiTDM()* where the SVD and COT occurs. The approximate placement of this routine in the overall DFTB+ structure can be found in Figure 5.3.

```fortran
1   ! Transform saved MO coefficient matrices using COT (SVD)
2   do iSpin = 1, size(gfilling, dim=3)
3     call tiTDM(tiMatG(:,:,iSpin), tiMatE(:,:,iSpin), tiMatS, gfilling
          (:,1,iSpin), mfilling(:,1,iSpin))
4     ! Make transition density lower triangular
5     do i = 1, n
6       forall (j=1:i) tiTransitionDensity(i,j, iSpin) = tiMatS(i,j)
7     enddo
8     ! Pack transition density matrix
9     rhoPrim(:,iSpin)=0.0_dp
10    call packHS(rhoPrim(:,iSpin), tiTransitionDensity(:,:,iSpin),
          neighbourlist%iNeighbour, nNeighbourSK, orb%mOrb, denseDesc%
          iAtomStart, iSparseStart, img2CentCell)
11    titracharges(:,:)=0.0_dp
12    call mulliken(tiTraCharges,over,rhoPrim(:,iSpin),orb,neighbourlist%
          iNeighbour,nNeighbourSK,img2CentCell,iSparseStart)
13    !Calculate Dipole
14    nAtom = size(tiTraCharges, dim=2)
15    do ii = 1, size(iAtInCentralRegion)
16      iAtom = iAtInCentralRegion(ii)
17      tiTDMom(:) = tiTDMom(:)&
18          & + sum(q0(:,iAtom,iSpin)-tiTraCharges(:,iAtom))*coord(:,iAtom)
19    enddo
20  enddo
```

**Listing 5.1** TI-DFTB TDM outer routine; calls COT, density packing, Mulliken analysis, and sums dipole moment.

92
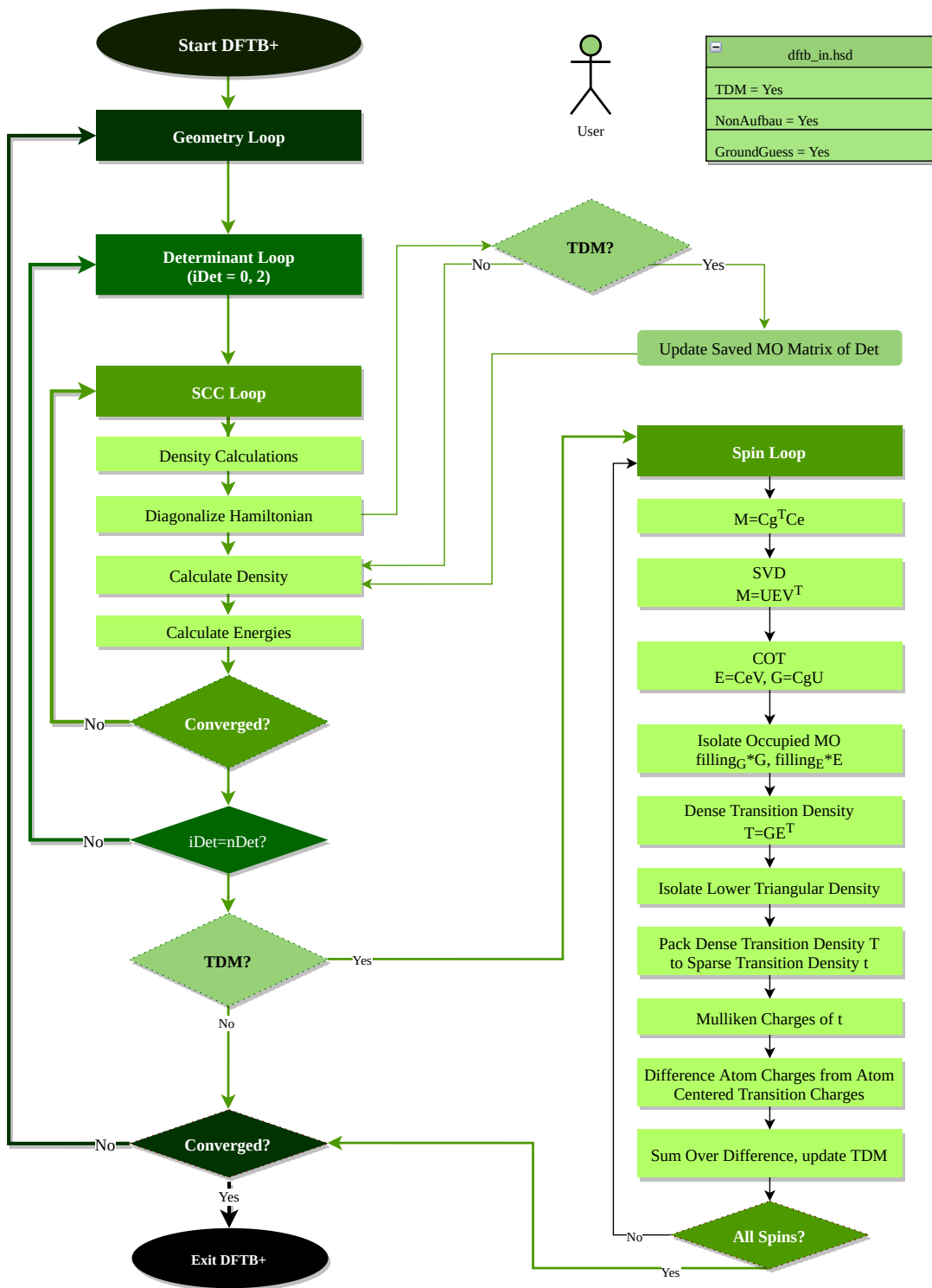
**Figure 5.3** TI-DFTB Transition dipole moment (TDM) calculation work-flow, highlighting how TI-TDM fits into the established ΔDFTB determinant loop, and algorithmic targets achieved in this implementation as described in Equation 5.30.

Listing 5.2 is an excerpt from the subroutine *tiTDM()* where SVD and COT are used to create the mutually orthogonal ES and GS vector spaces. SVD is accomplished with a **LAPACK** routine called *gesvd()*.[113]

```fortran
1   M=matmul(transpose(g),e)
2   !> Lapack routine SVD
3   call gesvd(M,u,sigma,vt)
4   !Transforms e with singular vectors and isolate occupied MO
5   M=matmul(e,transpose(vt))
6   do jj = 1, nElec
7     if (abs(mfilling(jj)) >= epsilon(1.0_dp)) then
8       Ce(:,jj) = mfilling(jj)*M(:,jj)
9     endif
10  end do
11  if (mfilling(nElec)==0.0_dp) then
12    do jj = nElec, na
13      if (abs(mfilling(jj)) >= epsilon(1.0_dp)) then
14        Ce(:, nElec) = mfilling(jj)*M(:,jj)
15      endif
16    enddo
17  endif
18  !Transforms g with singular vectors and isolate occupied MO
19  M=matmul(g,u)
20  do jj = 1, na
21    if (abs(gfilling(jj)) >= epsilon(1.0_dp)) then
22      Cg(:,jj) = gfilling(jj)*M(:,jj)
23    endif
24  end do
25  !> Cet*Cg, Transition Density of Excitation
26  M=matmul(Cg, transpose(Ce))
```

**Listing 5.2** TI-DFTB TDM subroutine which performs SVD and COT.

The general structure of these TDM subroutines was accomplished by closely emulating existing code structures for density, Mulliken population, dipole moment calculations already present in the DFTB+ main code. Interestingly, a difference between lines 26 of Listing 5.2 and Equation 5.32 arose when application of neither the DFTB+ overlap matrix (*SSqrReal*) nor the diagonal matrix form of the singular vectors ($S_{eg}$) produced reasonable values for transition dipole moments and were left out of the calculation. Looking deeper into the structure of DFTB it was noted that the overlap matrix was not used in calculating the density, therefore that structure was not used in our part of the code as well. Listing 5.3 shows a snippet of this main-code structure where the variables are declared for the *fullDensityMatrix_real()* subroutine. Note that only the eigenvectors and fillings are called.

```
1    !> the resulting nOrb*nOrb density matrix
2    real(dp), intent(out) :: dm(:,:)
3    !> the eigenvectors of the system
4    real(dp), intent(inout) :: eigenvecs(:,:)
5    !> the occupation numbers of the orbitals
6    real(dp), intent(in) :: filling(:)
```

**Listing 5.3** DFTB+ variables used in main-code density calculation.

This structure was therefore replicated in *tiTDM()* where as per Listing 5.2 lines 6-16 and 20-24 the electron occupancy is used to select only columns of the transformed MO coefficient matrices that are occupied. The sparse packing of *tiTransitionDensity(:,:,:)* and Mulliken population analysis (*mulliken()*) shown in Listing 5.1 are both subroutines local to the DFTB+ software package and were called as "black-boxes" such that no substantive alteration of the code occurred there. Lines 14-19 of Listing 5.1 is a direct translation of the local code structure for calculating ground state dipole moments in DFTB+.

A step by step printout of this type of calculation is described in subsection 6.3.1.

# Chapter Six

# PROOF OF CONCEPT (Representative Calculations in TI-DFTB 19.1)

## 6.1 Earlier Versions of the Code

To discuss the differences in coding organization between TI-DFTB 1.2 and 19.1 is like the colloquialism "apples and oranges" - which is to say that DFTB 1.2 and 19.1 are very different! This extends to their efficacy as well. In Table 6.1 the eye is somewhat befuddled by the sheer amount of different solutions, and the amount of solutions which could not lead to a stable final geometry (shown with italics). This data is admittedly not very lovely to look at, but it is included in full to communicate several ideas that will be focused and expanded upon. It is also included as a nod to the fact that the this was the first time I had ever used a terminal, and as such each of these calculations was individually and painstakingly executed by hand. I mention this to encourage future students that though the results are sometimes ugly and difficult at first, things do get easier. And ask your lab-mates to help you write a script, ASAP.

Let us look at the first two lines, where DFTB (a GS calculation) and TD-DFTB (an ES

|          | Coronene | Benzene | Butadiene | Indigo  | Fluorescein | Tetracene |
|----------|----------|---------|-----------|---------|-------------|-----------|
| DFTB     | -45.94   | -12.57  | -9.08     | -42.70  | -55.60      | -35.51    |
| TD-DFTB  | -45.89   | -12.57  | -9.06     | -42.70  | -55.56      | -35.51    |
| ΔDFTB    | *-45.78* | *-12.35*| -8.94     | -42.64  | -55.46      | -35.44    |
| MOM      | *-44.58* | -12.38  | -8.94     | -42.64  | *-44.89*    | -35.44    |
| IMOM     | -45.32   | -12.60  | -8.86     | *-40.84*| *-221.39*   | *-34.06*  |
| DAD1     | -43.68   | -12.60  | -8.86     | *-40.37*| *-325.35*   | *-33.65*  |
| DAD2     | -43.68   | -12.60  | -8.86     | *-40.37*| *-325.35*   | *-33.65*  |
| DAD3     | -43.68   | -12.60  | -8.86     | *-40.37*| *-325.35*   | *-33.65*  |
| DAD4     | -43.68   | -12.60  | -8.86     | *-40.37*| *-325.35*   | *-33.65*  |
| DAD5     | -43.68   | -12.60  | -8.86     | *-40.37*| *-325.35*   | *-33.65*  |
| DAD6     | -43.68   | -12.60  | -8.86     | *-40.37*| *-325.35*   | *-33.65*  |
| DAD7     | -43.68   | -12.60  | -8.86     | *-40.37*| *-325.35*   | *-33.65*  |
| DAD8     | -43.68   | -12.57  | -8.86     | *-40.37*| *-325.35*   | *-33.65*  |
| DAD9     | -43.68   | -12.52  | -8.75     | *-40.37*| *-325.35*   | *-33.65*  |
| DAD10    | *-42.93* | *-30.55*| -8.86     | *-40.37*| *-325.35*   | *-33.48*  |
| DAD11    | -44.13   | -12.53  | -8.98     | *-40.79*| *-325.35*   | *-33.85*  |
| DAD12    | -44.46   | *-28.29*| -8.61     | *-40.24*| *-325.35*   | *-33.85*  |
| DAD13    | -44.77   | -12.70  | -8.82     | *-40.64*| *-326.93*   | *-33.85*  |
| DAD14    | -44.77   | -12.19  | -8.83     | *-40.64*| -52.91      | -33.85    |
| DAD15    | -44.39   | -12.19  | -8.68     | *-40.64*| -52.91      | -33.85    |

**Table 6.1** Example final energy outputs (H) from geometry optimizations using TI-DFTB 1.2 for test-set of conjugated small molecules. The italicized numbers indicate a geometry optimization where the SCC converged at each geometry step, but the final geometry could not converge in 2000 steps using the Broyden mixer and Conjugate Gradient driver.

calculation) outputs are recorded. The perturbative excited-state method housed in DFTB+ could not faithfully account for reasonably spaced singlet excited-states in many of these small conjugated molecules, and for tetracene and indigo it predicted no stable excited-state. ΔDFTB 1.2 was able to predict reasonable excited states for butadiene, indigo, fluorescein and tetracene, but failed for the other two. Using MOM 1.2 one could find a solution for benzene, but fluorescein now fails. MOM 1.2 is able to reproduce ΔDFTB values for three molecules. IMOM 1.2 finds a solution for coronene, however the solutions for benzene and butadiene do not match ΔDFTB values, and the benzene excited-state is predicted to be lower energy than the ground-state! The DAD1-DAD15 data is particularly unwieldy, predicting many different converging solutions. Most notably, what happened to fluorescein?

This data does not make physical sense in the slightest, and riddling out what particularly was happening to cause such an upset was the focus of investigation for many months. It was eventually decided that what was happening was a continual update of the geometry loop from the ground-state eigenvectors, the triplet-state eigenvectors and then the mixed-state eigenvectors. As many as three geometry updates would happen in a single iteration of the geometry loop, and as such the eigenvectors of the previously calculated state were passed into the next as an initial guess. An optimized ground-state would update the geometry of the molecule and form the initial guess for the triplet-state, and that when optimized would again update the geometry and form the guess for the mixed. When the mixed was optimized, the geometry would be updated for the third time and written in the optimized geometry file. In larger systems like fluorescein this caused major upset, as shown in Figure 6.1.

The geometry for several selected steps are shown in Figure 6.1. It is unclear what happens to the eigenvectors in the last step to cause the energy to fall so low, as steps 2595 and 2644 look very similar. Perhaps in this step the hydrogens dissociated completely as they seem to be attempting throughout the calculation.

This dissociation of hydrogen was common in DAD and IMOM calculations, and it was later found that the eigenvectors were not sorted in such a way that affected the electron
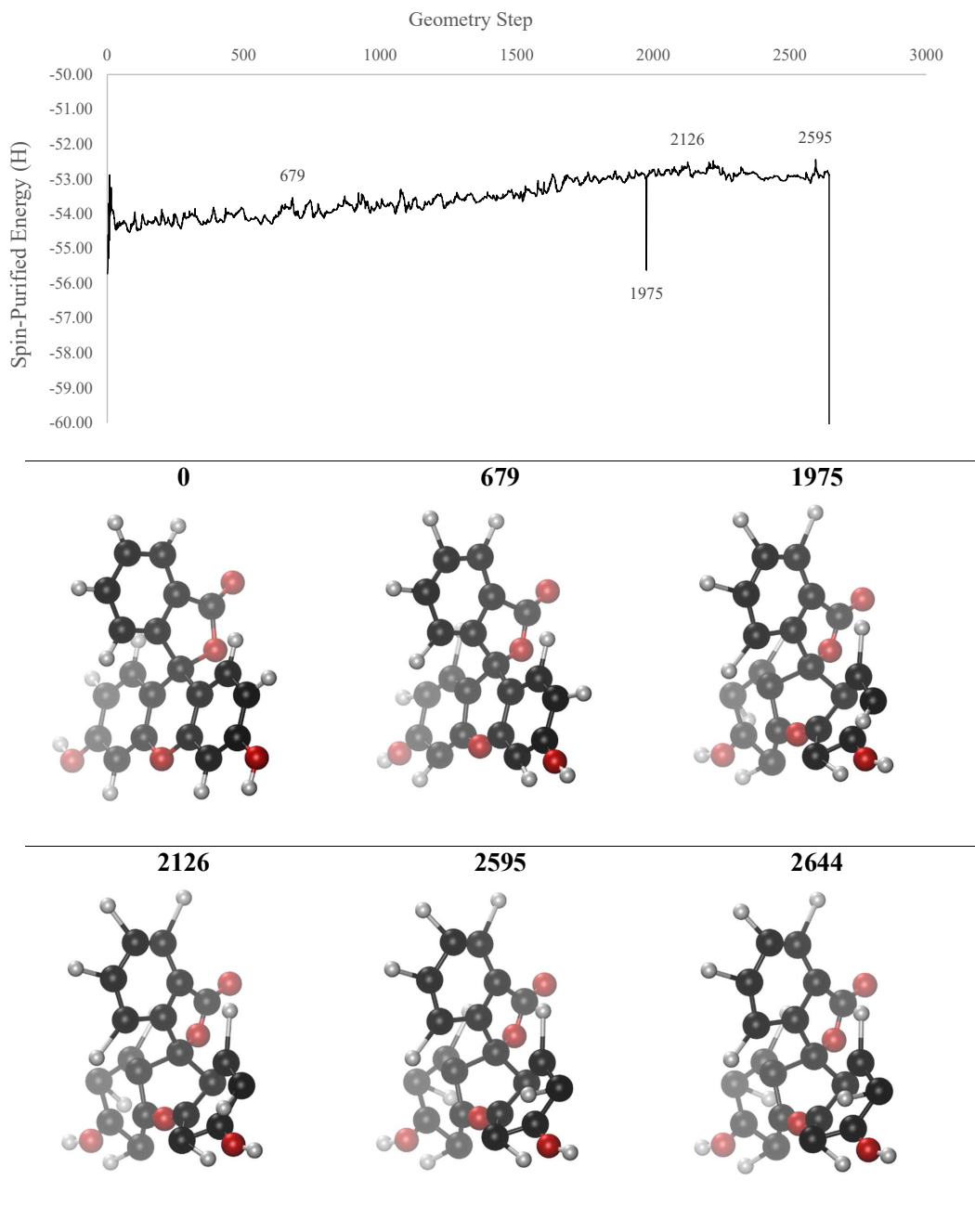
**Figure 6.1** DAD10 1.2 geometry optimization of fluorescein with several geometries from peaks or valleys shown. Geometry does not update correctly, and affects strange crumpled structure, leading to an overall rising energy that will not converge.

filling, only the diagonalization and assignment of eigenvalues. Another frightening example of geometry upset was found in tetracene examples where the code had been updated into DFTB+ 17.1. Unfortunately, the code did tend to update before complete programming efforts had been completed a number of times throughout this project, but this total rehauling of efforts allowed for a very thorough reevaluation of what elements of our code caused problems, as well as an strong familiarity with the general structure of the DFTB+ program.

In Figure 6.2 the final geometries of multiple tetracene calculations are shown, as well as the final printed geometries from the current SCC cycle in Table 6.2. Values corresponding to geometries in red were the final total energy of the SCC cycle where the calculation stopped.



| | |
|---|---|
| DAD 10 | -33.4803 H |
| IMOM | -33.5661 H |
| DAD 1 -9 | -33.6905 H |
| DAD 11 -15 | -33.7363 H |
| MOM | -35.4484 H |
| ΔDFTB | -35.4484 H |
| TD-DFTB | -35.5076 H |
| DFTB+ (ground) | -35.5076 H |
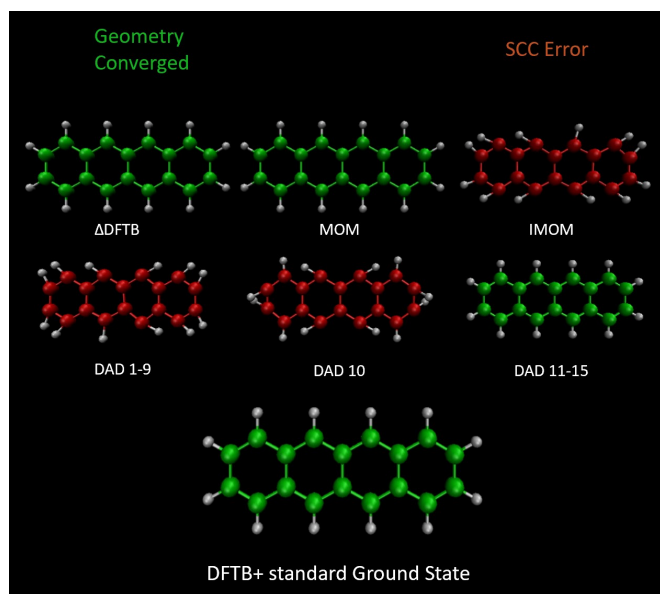
**Figure 6.2** Final geometry of optimization, showing clear issues with IMOM and DAD methods in DFTB+ 17.2.

**Table 6.2** Final converged energies of multiple methods, shows an excited state that MOM 17.2 and ΔDFTB 17.2 were able to capture that TD-DFTB could not, as well as higher energies of strained structures.

In this iteration of the code, there was not an issue of erroneous SCC convergence, and the failed calculations produced errors relating to a lack of SCC convergence. The final energies were taken from the last successful SCC iteration for the table above.

This approach was carefully reworked in DFTB+ 19.1 so as to avoid the pitfalls that have been presented here. Once the determinant loop was added, there was explicit logic that allowed the eigenvectors from the previous determinant to be explicitly overwritten with a new initial guess. Also, the determinants previous would not affect the geometry of that iteration of the geometry cycle. These together solved the issues of hydrogen migration, node formation, and general wadding up that tended to happen before.

## 6.2   TI-DFTB 19.1

### 6.2.1   Numerical Gradients of Hydrogen
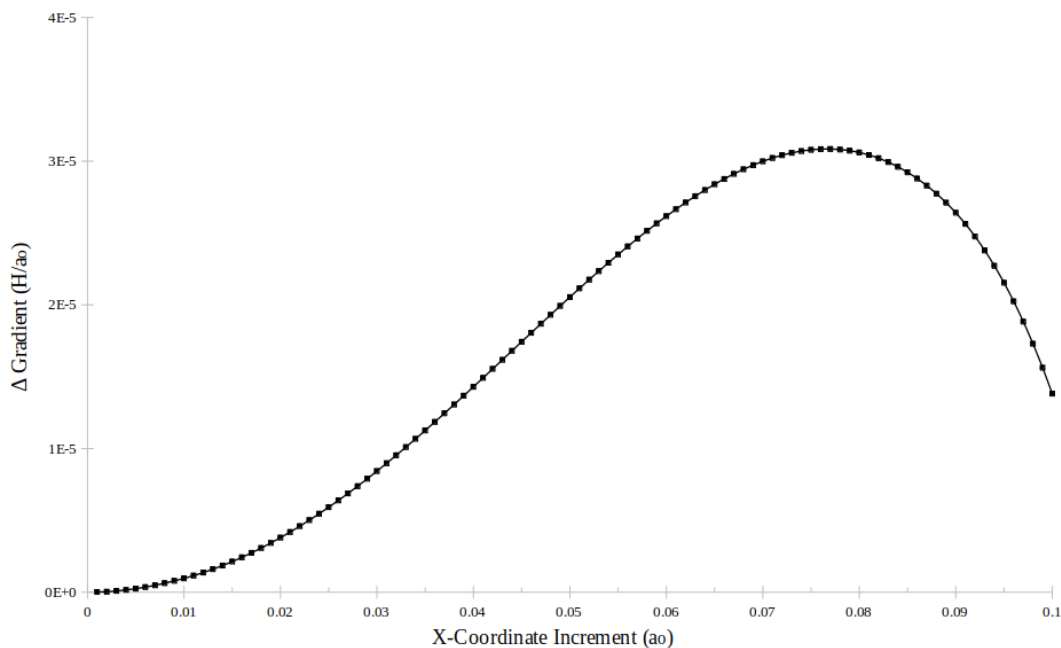


**Figure 6.3** Difference between analytically and numerically calculated gradients of TI-DFTB energy for $H_2$ showing smooth convergence at zero.

A hydrogen ($H_2$) molecule with a reference bond length of 1.000Å was evaluated with $\Delta$DFTB for the analytical gradient ($\nabla_0 E$=-0.14 H/$a_0$). The numerical gradients were calculated by evaluating the $\Delta$DFTB energy for $H_2$ at 100 increments ($x$) of $\pm 0.001x$ Å past the reference bond length. These energies ($E_{(\pm x)}$) were used to calculate the numerical gradients as follows:

$$\nabla_n E = \frac{E_{(-x)} - E_{(+x)}}{2 \times 0.001x} \tag{6.1}$$

The difference between $\nabla_0 E$ and $\nabla_n E$ is plotted in Figure 6.3. This chart shows a smooth convergence at zero on the x-axis, which indicates that for $\Delta$DFTB:

$$\lim_{\Delta x \to 0} \frac{\Delta E}{\Delta x} = \frac{\delta E}{\delta x} \tag{6.2}$$

102

## 6.2.2 Geometry Optimization of Acridinium Salts

In TI-DFTB 19.1, geometry optimizations of six acridinium salts were run, calling non-Aufbau fillings, spin-purification and the ground-guess functions. These molecules are promising organic catalysts,[114,115] have been investigated by our lab in the past,[116] and are a good size for methodological speed comparisons and also possess high levels of conjugation to test convergence strategies. These optimizations were performed with the Broyden mixer and Conjugate Gradient as above, and allowed to run for up to 1,000 steps although many converged at the excited state in under 300 steps. Their final GS and spin-purified ES energies are shown in Table 6.3, and the geometry optimization paths are plotted in Figure 6.4 to show a general proof of concept for $\Delta$DFTB 19.1 and the ground-guess function.

| | A | B | C | D | E | F |
|---|---|---|---|---|---|---|
| Functional Group | naphthalene | benzene | toluene | mesitylene | anthracene | xylene |
| Ground-State Energy (H) | -50.24 | -42.59 | -45.07 | -50.25 | -57.89 | -47.56 |
| Excited-State Energy (H) | -50.18 | -42.52 | -45.00 | -50.21 | -57.83 | -47.49 |
| HOMO-LUMO Gap (eV) | 1.765 | 1.967 | 1.913 | 1.056 | 1.438 | 1.903 |

**Table 6.3** Final excited- and ground-state energies of six acridinium salts and excitation energies in eV.

These figures show a clear and dramatic difference when compared to the figures in section 6.1. Figure 6.4 has clean smooth total energy values near the end of the calculation, and after the initial changes to the geometry are constantly decreasing in value. These calculations have a three-determinant loop called due to the spin-purification and ground-guess functions, yet manage to maintain discrete energy calculations for each state.
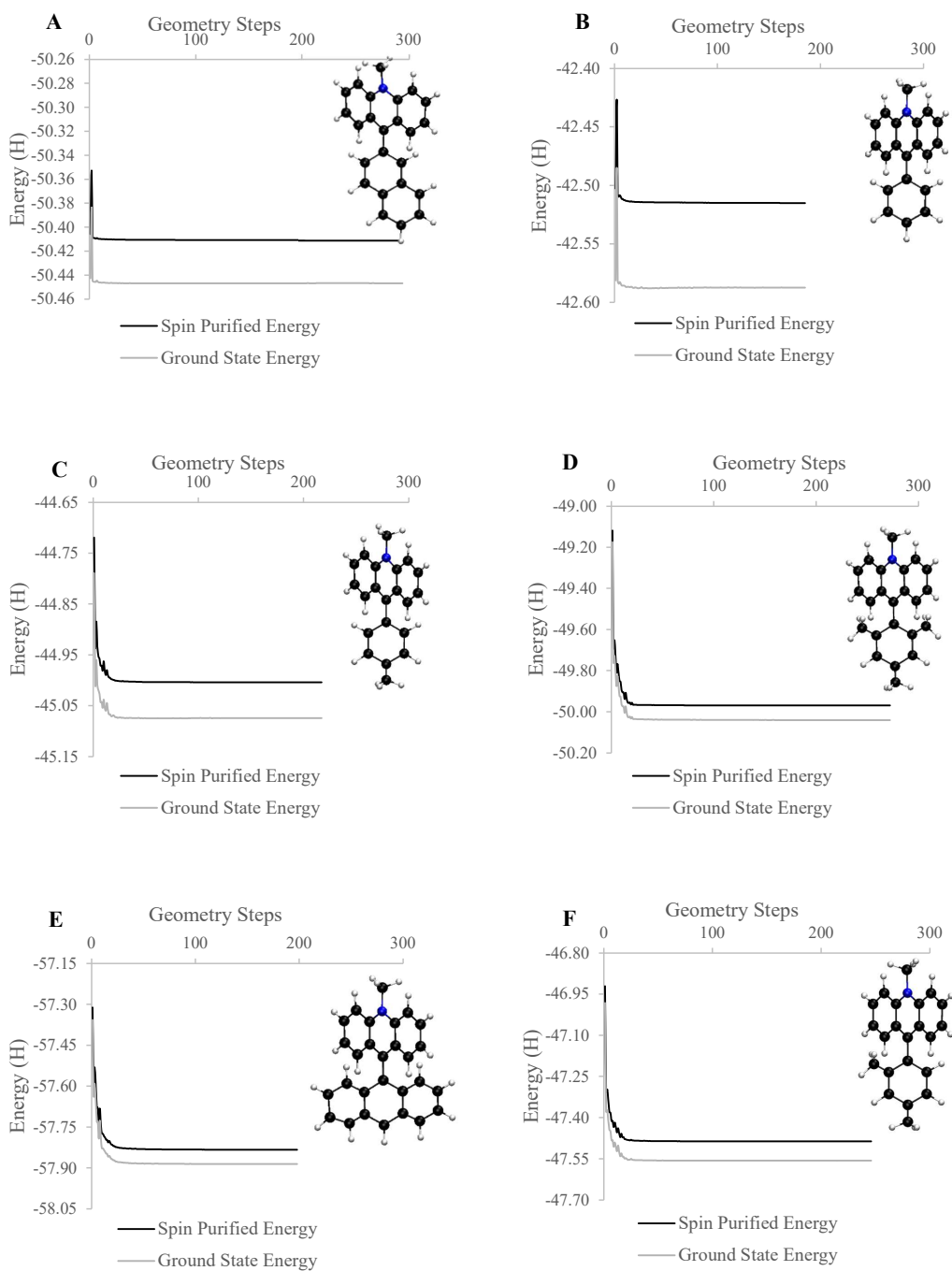
**Figure 6.4** TI-DFTB geometry optimizations of six acridinium salts showing functionality of the ground-guess, and preservation of the HOMO-LUMO gap throughout geometry changes. Geometry optimizations are driven by the geometry of the excited-state, and 4 examples were able to converge in less than 300 steps. C and F required more steps; 825 and 1133 respectively.

Qualitatively, one can observe in these representations a relative proportionality between HOMO-LUMO gaps and total energy that are consistent with chemical intuition. In Figure 6.4F we find the lowest overall energy for both the ES and GS, which would be expected from something so highly conjugated as the anthracene group. This example also has one of the lower HOMO-LUMO gaps at 1.77 eV, second only to the mesitylene functionalized salt (Table 6.3). Acridinium salt D functionalized with mesitylene has a higher energy than E, but a lower vertical excitation energy potentially due to the favorably placed electron donating groups. Conversely, Figure 6.4B shows the energy of an acridinium salt with a basic phenyl group that has one of the highest energies, that is the least stable of the set. This instability is consistent with the largest vertical excitation energy of nearly 2 eV.

Possible future work involves varying the driver and basis sets used for these kind of calculations. There has been studies that find there are accelerated drivers that might speed the optimization even more,[117,118] and different basis sets or higher levels of parameterization may positively affect the accuracy of this data.[119,120]

### 6.2.3 Single Point Energy Calculation of Coronene

Along with the new determinant loop in DFTB+ 19.1 removing the earlier code's error when updating the geometry cycle, new efforts to implement MOM, IMOM and DAD resulted in much higher fidelity when using these methods. In DFTB+ 1.2, coronene geometry optimizations failed for $\Delta$DFTB, MOM, and DAD 10. IMOM, DAD1-DAD9, and DAD11-DAD15 all converged, but these methods resulted in six different final energies for singly excited coronene (Table 6.1). Using TI-DFTB 19.1, single point calculations for coronene from the same initial geometry as used for Table 6.1 were used to construct the plots in Figure 6.5.

In Figure 6.5-Delta, $\Delta$DFTB fails after 100 SCC iterations due to evident trapping of the calculation in some potential well. The steps taken in this example show the calculated energy bouncing back and forth between two solutions with some periodicity. A possible reason for this phenomenon could be a poor initial guess, which is evidenced by the three large and distinct energy spikes in the first 10 iterations of the calculation.

Figure 6.5-MOM shows that with the addition of MOM to this calculation, the previously difficult to converge SCC energy is optimized in under 20 iterations. By influencing the subsequent SCC iterations with the eigenvectors previous, the calculation does not make such dramatic swings in energy as the space is optimized. Because this system is large and conjugated the virtual orbitals are low-lying and nearly degenerate, so allowing population of different virtual orbitals results in the optimization more easily finding the lowest energy solution.

In a visually stimulating reinforcement of the hypothesis about a poor initial guess, Figure 6.5-IMOM shows a compounding oscillation about the theorized potential well. Continually projecting onto the initial space, which was probably defined poorly, exacerbated the periodic energy spikes seen by using $\Delta$DFTB for this system.

DAD was employed slightly differently than previously reported in Table 6.1, for instead

106
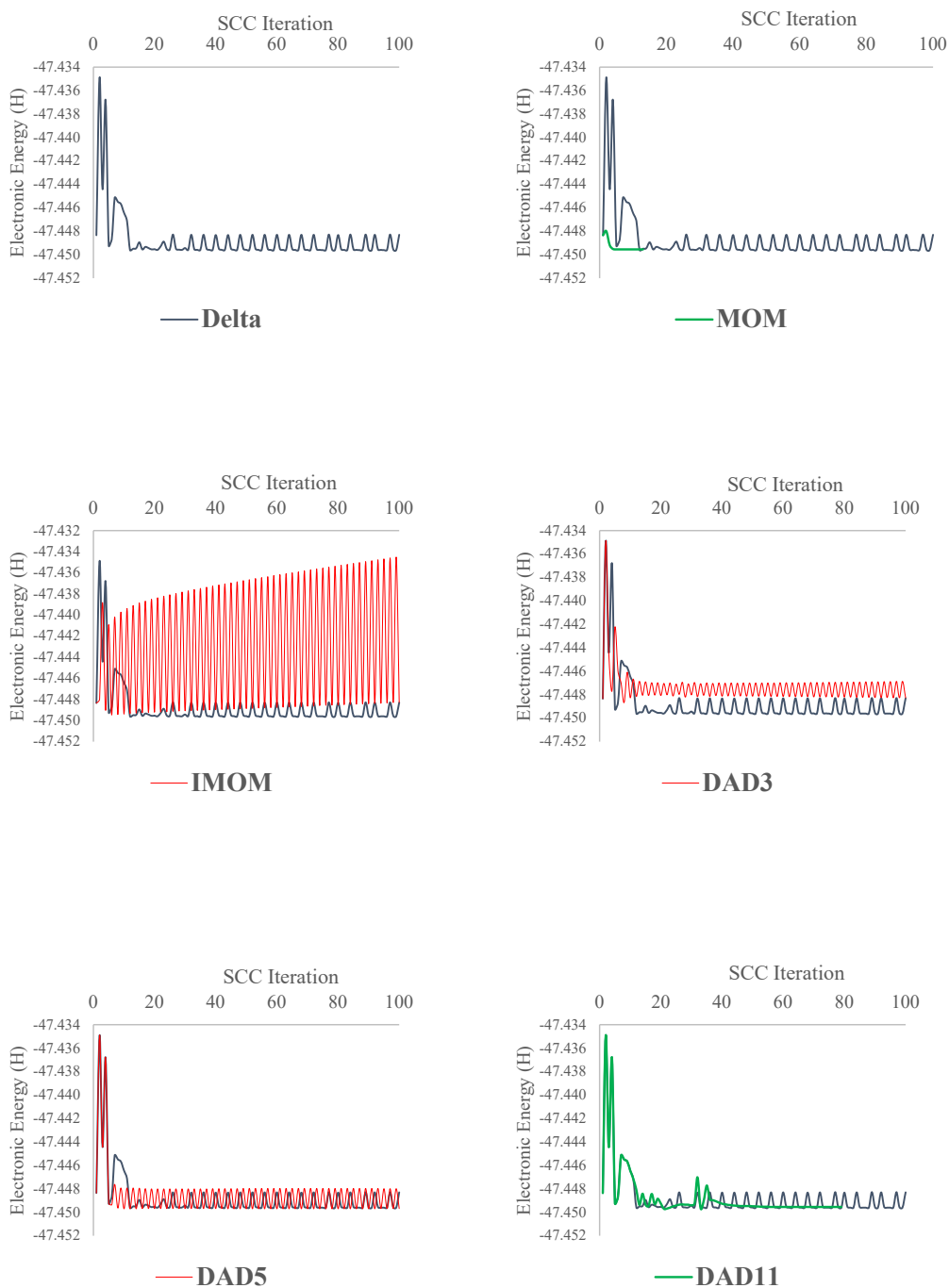
**Figure 6.5** TI-DFTB geometry optimizations of six acridinium salts showing functionality of the ground-guess, and preservation of the HOMO-LUMO gap throughout geometry changes. Geometry optimizations are driven by the geometry of the excited-state, and 4 examples were able to converge in less than 300 steps. C and F required more steps; 825 and 1133 respectively.

of blindly projecting onto any of the first several spaces, DAD was used strategically to project onto a local minimum present in the first steps of the $\Delta$DFTB calculation. Local minima were found at step 3, 5 and 11, therefore DAD3, DAD5 and DAD11 were calculated for this system. As shown in Figure 6.5-DAD3, this higher energy minimum trapped the calculation in a higher energy state along the well compared to the $\Delta$DFTB path, while Figure 6.5-DAD5 shows an increased frequency and amplitude of the energy oscillation from $\Delta$DFTB. These two representations are a strong proof of concept for the functionality of DAD, as well as a beautiful representation of a small and mysterious piece of the multi-dimensional potential energy surface. Figure 6.5-DAD11 converges at the energy minimum found by using MOM on this system (Figure 6.5-MOM).

This data, compared to the data from section 6.1, shows a much more clear physical representation of the mathematical intention behind the programming of MOM, IMOM and DAD. These functions of TI-DFTB 19.1 allow the user to make informed guesses as to how to calculate the ES energy of their systems, and how to overcome convergence issues in even large conjugated systems like coronene.

## 6.3 Transition Dipole Moments in TI-DFTB 19.1

### 6.3.1 TDM Analysis of Nitrogen

Let's jump right in to a real example of SVD and COT being applied to a $\Delta$DFTB output of the $\alpha$ spin channel of $N_2$, using a mixed-state ($E$) and a GS ($G$) MO coefficient matrix to calculate the non-diagonal overlap matrix, $\mathbb{M}$. For each $\mathbf{C}$ matrix, the rows indicate the AO contribution to each MO. From top to bottom the AO index of the rows for dinitrogen $\mathbf{C}$ are: from $N_1\{2s, 2p_x, 2p_y, 2p_z\}$, and from $N_2\{2s, 2p_x, 2p_y, 2p_z\}$. The columns indicate the MO's comporised of AO character. The columns from right to left for dinitrogen $\mathbf{C}$ are: $\{1\sigma_g, 1\sigma_u, \pi_u^x, \pi_u^y, 2\sigma_g, \pi_g^x, \pi_g^y, 2\sigma_u\}$.

$$
G = \begin{bmatrix}
0.56 & 0.62 & \mathbf{0.00} & \mathbf{0.00} & 0.32 & \mathbf{0.00} & \mathbf{0.00} & -0.71 \\
0.09 & -0.20 & \mathbf{0.01} & \mathbf{-0.54} & -0.35 & \mathbf{-0.61} & \mathbf{0.17} & -0.53 \\
0.09 & -0.20 & \mathbf{-0.47} & \mathbf{0.26} & -0.35 & \mathbf{0.16} & \mathbf{-0.61} & -0.53 \\
0.09 & -0.20 & \mathbf{0.46} & \mathbf{0.28} & -0.35 & \mathbf{0.45} & \mathbf{0.44} & -0.53 \\
0.56 & -0.62 & \mathbf{0.00} & \mathbf{0.00} & 0.32 & \mathbf{0.00} & \mathbf{0.00} & 0.71 \\
-0.09 & -0.20 & \mathbf{0.01} & \mathbf{-0.54} & 0.35 & \mathbf{0.61} & \mathbf{-0.17} & -0.53 \\
-0.09 & -0.20 & \mathbf{-0.47} & \mathbf{0.26} & 0.35 & \mathbf{-0.16} & \mathbf{0.61} & -0.53 \\
-0.09 & -0.20 & \mathbf{0.46} & \mathbf{0.28} & 0.35 & \mathbf{-0.45} & \mathbf{-0.44} & -0.53
\end{bmatrix}
$$

$$
E = \begin{bmatrix}
0.56 & 0.62 & \mathbf{0.00} & \mathbf{0.00} & 0.32 & \mathbf{0.00} & \mathbf{0.00} & -0.71 \\
0.09 & -0.20 & \mathbf{-0.51} & \mathbf{-0.16} & -0.35 & \mathbf{0.18} & \mathbf{-0.60} & -0.53 \\
0.09 & -0.20 & \mathbf{0.39} & \mathbf{-0.37} & -0.35 & \mathbf{0.43} & \mathbf{0.46} & -0.53 \\
0.09 & -0.20 & \mathbf{0.12} & \mathbf{0.52} & -0.35 & \mathbf{-0.61} & \mathbf{0.14} & -0.53 \\
0.56 & -0.62 & \mathbf{0.00} & \mathbf{0.00} & 0.32 & \mathbf{0.00} & \mathbf{0.00} & 0.71 \\
-0.09 & -0.20 & \mathbf{-0.51} & \mathbf{-0.16} & 0.35 & \mathbf{-0.18} & \mathbf{0.60} & -0.53 \\
-0.09 & -0.20 & \mathbf{0.39} & \mathbf{-0.37} & 0.35 & \mathbf{-0.43} & \mathbf{-0.46} & -0.53 \\
-0.09 & -0.20 & \mathbf{0.12} & \mathbf{0.52} & 0.35 & \mathbf{0.61} & \mathbf{-0.14} & -0.53
\end{bmatrix}
$$

$$(6.3)$$

Notice the bold columns in Equation 6.3. The difference between these columns in $G$ and $E$ indicate where the $\Delta$DFTB excitation from GS to ES affected the shape of the $\pi_u^{xy}$ and $\pi_g^{xy}$ molecular orbitals. The predicted HOMO in this system is column 5, the $2\sigma_g$ orbital, and the LUMO is column 6, one of the degenerate $\pi_g^{xy}$. The inner products of the columns of $G$ called $\vec{g}_i$ and the columns of $E$, $e_j$ indicate that these two matrices though individually orthogonal are not mutually orthogonal, that is $\langle \vec{g}_i | \vec{e}_j \rangle \neq \delta_{ij}$. For example, the inner product of $\vec{g}_4$ and $\vec{e}_4$ is not 1 as would be necessary, the value of $\vec{g}_4 \times \vec{e}_4 = 0.27$. The inner product of $\vec{g}_3$ and $\vec{e}_4$ is not 0, the value of $\vec{g}_3 \times \vec{e}_4 = 0.82$.

Now let us calculate $G^T E = \mathbb{M}$.

$$\mathbb{M} = \begin{bmatrix} \mathbf{0.69} & 0.00 & 0.00 & 0.00 & \mathbf{0.16} & 0.00 & 0.00 & 0.00 \\ 0.00 & \mathbf{1.01} & 0.00 & 0.00 & 0.00 & 0.00 & 0.00 & \mathbf{-0.26} \\ 0.00 & 0.00 & \mathbf{-0.27} & \mathbf{0.82} & 0.00 & 0.00 & 0.00 & 0.00 \\ 0.00 & 0.00 & \mathbf{0.82} & \mathbf{0.27} & 0.00 & 0.00 & 0.00 & 0.00 \\ \mathbf{0.16} & 0.00 & 0.00 & 0.00 & \mathbf{0.95} & 0.00 & 0.00 & 0.00 \\ 0.00 & 0.00 & 0.00 & 0.00 & 0.00 & \mathbf{-0.64} & \mathbf{1.00} & 0.00 \\ 0.00 & 0.00 & 0.00 & 0.00 & 0.00 & \mathbf{-1.00} & \mathbf{-0.64} & 0.00 \\ 0.00 & \mathbf{-0.26} & 0.00 & 0.00 & 0.00 & 0.00 & 0.00 & \mathbf{2.69} \end{bmatrix} \qquad (6.4)$$

This matrix $\mathbb{M}$ tells us a lot of what has happened by this excitation. Columns $3, 4, 6$ and $7$ inform us that the effect of excitation upon the $\pi_u^{xy}$ and $\pi_g^{xy}$ were rotations of these MO. Columns 3 and 4 show an improper rotation of $\pi_u^{xy}$ with the matrix form $\left( \begin{smallmatrix} \cos\theta & \sin\theta \\ \sin\theta & -\cos\theta \end{smallmatrix} \right)$, and columns 6 and 7 show a proper rotation of $\pi_g^{xy}$ with the matrix form $\left( \begin{smallmatrix} \cos\theta & -\sin\theta \\ \sin\theta & \cos\theta \end{smallmatrix} \right)$. Rotations of these MO indicate a rotation of the $N_2$ bond in response to excitation. Math is beautiful!

Notice too column and row 5. This is the HOMO from which the electron was excited, so it is in $G$ an occupied orbital and in $E$ a virtual orbital. The off diagonal elements of these indices are therefore important information when calculating transition properties.

However, concerning SVD, this matrix is not symmetric. It is nearly so however columns 6 and 7 have a discrepancy. How does this affect SVD?

Let us first construct the rows of $\mathbb{V}^{\mathbb{T}}$ which will be composed of orthonormal eigenvectors of $\mathbb{M}^{\mathbb{T}}\mathbb{M}$. In Equation 6.5 again we see many pairs of vectors forming rotation matrices.

$$\mathbb{V}^{\mathbb{T}} = \begin{bmatrix} \mathbf{0.91} & 0.00 & 0.00 & 0.00 & \mathbf{-0.42} & 0.00 & 0.00 & 0.00 \\ \mathbf{-0.42} & 0.00 & 0.00 & 0.00 & \mathbf{-0.91} & 0.00 & 0.00 & 0.00 \\ 0.00 & \mathbf{0.15} & 0.00 & 0.00 & 0.00 & 0.00 & 0.00 & \mathbf{-0.99} \\ 0.00 & \mathbf{-0.99} & 0.00 & 0.00 & 0.00 & 0.00 & 0.00 & \mathbf{-0.15} \\ 0.00 & 0.00 & \mathbf{-0.97} & \mathbf{-0.26} & 0.00 & 0.00 & 0.00 & 0.00 \\ 0.00 & 0.00 & \mathbf{0.26} & \mathbf{-0.97} & 0.00 & 0.00 & 0.00 & 0.00 \\ 0.00 & 0.00 & 0.00 & 0.00 & 0.00 & \mathbf{0.97} & \mathbf{-0.25} & 0.00 \\ 0.00 & 0.00 & 0.00 & 0.00 & 0.00 & \mathbf{-0.25} & \mathbf{-0.97} & 0.00 \end{bmatrix} \qquad (6.5)$$

Then we solve for the singular values of $\mathbb{M}^{\mathbb{T}}\mathbb{M}$, or the eigenvalues of $\mathbb{M}$ as described by Equation 6.6. The HOMO and LUMO are in bold. The depopulated HOMO has shrunk, and the newly populated LUMO has grown. The other virtual orbitals have also been stretched, and the $\pi_u^{xy}$ and $\pi_g^{xy}$ have equally shrunk and stretched respectively.

$$\sigma_i = \left\{ 0.61 \quad 1.03 \quad 0.86 \quad 0.86 \quad \mathbf{0.97} \quad \mathbf{2.73} \quad 1.18 \quad 1.18 \right\} \tag{6.6}$$

Now we calculate the column vectors of $\mathbb{U}$ which will form an orthonormal basis of ColM. Here is where the asymmetry plays a part. Notice in Equation 6.7 that the columns of $\mathbb{U}$ also form rotation matrices!

$$\mathbb{U} = \begin{bmatrix} \mathbf{0.15} & 0.00 & 0.00 & 0.00 & \mathbf{-0.99} & 0.00 & 0.00 & 0.00 \\ \mathbf{-0.99} & 0.00 & 0.00 & 0.00 & \mathbf{-0.15} & 0.00 & 0.00 & 0.00 \\ 0.00 & \mathbf{-0.74} & \mathbf{-0.68} & 0.00 & 0.00 & 0.00 & 0.00 & 0.00 \\ 0.00 & \mathbf{-0.68} & \mathbf{0.74} & 0.00 & 0.00 & 0.00 & 0.00 & 0.00 \\ 0.00 & 0.00 & 0.00 & \mathbf{-0.42} & 0.00 & 0.00 & 0.00 & \mathbf{0.91} \\ 0.00 & 0.00 & 0.00 & \mathbf{-0.91} & 0.00 & 0.00 & 0.00 & \mathbf{-0.42} \\ 0.00 & 0.00 & 0.00 & 0.00 & 0.00 & \mathbf{0.06} & \mathbf{-1.00} & 0.00 \\ 0.00 & 0.00 & 0.00 & 0.00 & 0.00 & \mathbf{-1.00} & \mathbf{-0.06} & 0.00 \end{bmatrix} \tag{6.7}$$

What does this tell us about the fundamental difference between the ground state $G$ and the excited state $E$? As described in subsection 5.1.2, the SCC pathway rotates the MO spaces within an AO basis to correctly describe the electronic space in question. We have formed two rotation transformation matrices in the pursuit of the left singular vectors and right singular vectors of the overlap matrix $\mathbb{M}$ between the GS and ES of $N_2$. These results make intuitive sense in light of a rotating SCC pathway. Also, we have calculated singular values for the overlap matrix $\mathbb{M}$ that make chemically intuitive sense with regards to how the MO will react to an excited electron.

These transformation matrices and the singular values will play the integral part in calculating the information about transition between these two states. Applying these matrices to $G$ and $E$ as described in Equation 5.30 rotates these spaces so that they are mutually orthogonal.

$$G\mathbb{U} = C_g = \begin{bmatrix} \mathbf{0.79} & \mathbf{0.00} & \mathbf{0.00} & \mathbf{-0.53} & \mathbf{-0.51} & 0.00 & 0.00 & 0.38 \\ \mathbf{0.49} & \mathbf{0.33} & \mathbf{0.53} & \mathbf{0.28} & \mathbf{0.27} & 0.54 & 0.02 & 0.23 \\ \mathbf{0.49} & \mathbf{0.30} & \mathbf{-0.55} & \mathbf{0.28} & \mathbf{0.27} & -0.28 & 0.46 & 0.23 \\ \mathbf{0.49} & \mathbf{-0.63} & \mathbf{0.02} & \mathbf{0.28} & \mathbf{0.27} & -0.25 & -0.47 & 0.23 \\ \mathbf{-0.79} & \mathbf{0.00} & \mathbf{0.00} & \mathbf{-0.53} & \mathbf{0.51} & 0.00 & 0.00 & 0.38 \\ \mathbf{0.49} & \mathbf{-0.33} & \mathbf{-0.53} & \mathbf{-0.28} & \mathbf{0.27} & 0.54 & 0.02 & -0.23 \\ \mathbf{0.49} & \mathbf{-0.30} & \mathbf{0.55} & \mathbf{-0.28} & \mathbf{0.27} & -0.28 & 0.46 & -0.23 \\ \mathbf{0.49} & \mathbf{0.63} & \mathbf{-0.02} & \mathbf{-0.28} & \mathbf{0.27} & -0.25 & -0.47 & -0.23 \end{bmatrix}$$

$$E\mathbb{V} = C_e = \begin{bmatrix} \mathbf{0.79} & \mathbf{0.00} & \mathbf{0.00} & \mathbf{-0.53} & -0.51 & \mathbf{0.00} & 0.00 & 0.38 \\ \mathbf{0.49} & \mathbf{0.33} & \mathbf{0.53} & \mathbf{0.28} & 0.27 & \mathbf{0.54} & 0.02 & 0.23 \\ \mathbf{0.49} & \mathbf{0.30} & \mathbf{-0.55} & \mathbf{0.28} & 0.27 & \mathbf{-0.28} & 0.46 & 0.23 \\ \mathbf{0.49} & \mathbf{-0.63} & \mathbf{0.02} & \mathbf{0.28} & 0.27 & \mathbf{-0.25} & -0.47 & 0.23 \\ \mathbf{-0.79} & \mathbf{0.00} & \mathbf{0.00} & \mathbf{-0.53} & 0.51 & \mathbf{0.00} & 0.00 & 0.38 \\ \mathbf{0.49} & \mathbf{-0.33} & \mathbf{-0.53} & \mathbf{-0.28} & 0.27 & \mathbf{0.54} & 0.02 & -0.23 \\ \mathbf{0.49} & \mathbf{-0.30} & \mathbf{0.55} & \mathbf{-0.28} & 0.27 & \mathbf{-0.28} & 0.46 & -0.23 \\ \mathbf{0.49} & \mathbf{0.63} & \mathbf{-0.02} & \mathbf{-0.28} & 0.27 & \mathbf{-0.25} & -0.47 & -0.23 \end{bmatrix}$$

(6.8)

Notice that $Cg = Ce$, and therefore a linearly independent set of column vectors have been produced that span all of $\mathbb{R}^8$. The individually orthogonal vectors of $G$ and $E$ have been rotated onto a space that can be loosely interpreted as the discrete electronic densities, or orbitals of transition. These orbitals are then used to calculate the electronic density of transition ($\rho_{g \to e}$) by selecting only the occupied transition orbitals (in bold in Equation 6.8) according to Equation 6.9.

$$\rho_{g \to e} = C_g^{\text{occ}} (C_e^{\text{occ}})^T$$

$$\rho_{g \to e} = \begin{bmatrix} 0.79 & 0.00 & 0.00 & -0.53 & -0.51 \\ 0.49 & 0.33 & 0.53 & 0.28 & 0.27 \\ 0.49 & 0.30 & -0.55 & 0.28 & 0.27 \\ 0.49 & -0.63 & 0.02 & 0.28 & 0.27 \\ -0.79 & 0.00 & 0.00 & -0.53 & 0.51 \\ 0.49 & -0.33 & -0.53 & -0.28 & 0.27 \\ 0.49 & -0.30 & 0.55 & -0.28 & 0.27 \\ 0.49 & 0.63 & -0.02 & -0.28 & 0.27 \end{bmatrix} \begin{bmatrix} 0.79 & 0.00 & 0.00 & -0.53 & 0.00 \\ 0.49 & 0.33 & 0.53 & 0.28 & 0.54 \\ 0.49 & 0.30 & -0.55 & 0.28 & -0.28 \\ 0.49 & -0.63 & 0.02 & 0.28 & -0.25 \\ -0.79 & 0.00 & 0.00 & -0.53 & 0.00 \\ 0.49 & -0.33 & -0.53 & -0.28 & 0.54 \\ 0.49 & -0.30 & 0.55 & -0.28 & -0.28 \\ 0.49 & 0.63 & -0.02 & -0.28 & -0.25 \end{bmatrix}^T$$

$$\rho_{g \to e} = \begin{bmatrix} 0.91 & -0.03 & 0.39 & 0.37 & -0.36 & 0.27 & 0.69 & 0.67 \\ 0.24 & 0.87 & 0.05 & 0.06 & -0.54 & -0.08 & 0.28 & 0.29 \\ 0.24 & 0.27 & 0.64 & 0.06 & -0.54 & 0.51 & -0.31 & 0.29 \\ 0.24 & 0.27 & 0.05 & 0.65 & -0.54 & 0.51 & 0.28 & -0.30 \\ -0.36 & -0.27 & -0.69 & -0.67 & 0.91 & 0.03 & -0.39 & -0.37 \\ 0.54 & -0.08 & 0.28 & 0.29 & -0.24 & 0.87 & 0.05 & 0.06 \\ 0.54 & 0.51 & -0.31 & 0.29 & -0.24 & 0.27 & 0.64 & 0.06 \\ 0.54 & 0.51 & 0.28 & -0.30 & -0.24 & 0.27 & 0.05 & 0.65 \end{bmatrix}$$

(6.9)

$\rho_{g \to e}$ is then packed into a sparse matrix representation, and fed into a subroutine that calculates the transition Mulliken populations on each atom. For $N_2$ these transition charges for this alpha spin channel ($q_\alpha$) are shown below in Table 6.4, as well as the neutral atomic charge populations ($q_0$).

|  | $q_\alpha$ |  | $q_0$ |  |
|---|---|---|---|---|
| $\sigma$ | N1 | N2 | N1 | N2 |
| $2s$ | 0.50 | 0.50 | 2.00 | 2.00 |
| $2p_x$ | 0.65 | 0.67 | 1.00 | 1.00 |
| $2p_y$ | 0.42 | 0.41 | 1.00 | 1.00 |
| $2p_z$ | 0.43 | 0.42 | 1.00 | 1.00 |

**Table 6.4** TI-DFTB calculated charge per atomic orbital for $N_2$

These charges were used to calculate the TDM in accordance with ground state dipole moment calculations from other parts of the program. The final TDM of $N_2$ was calculated to be 0.94 au, and is depicted visually below showing transition charge localization on N1.
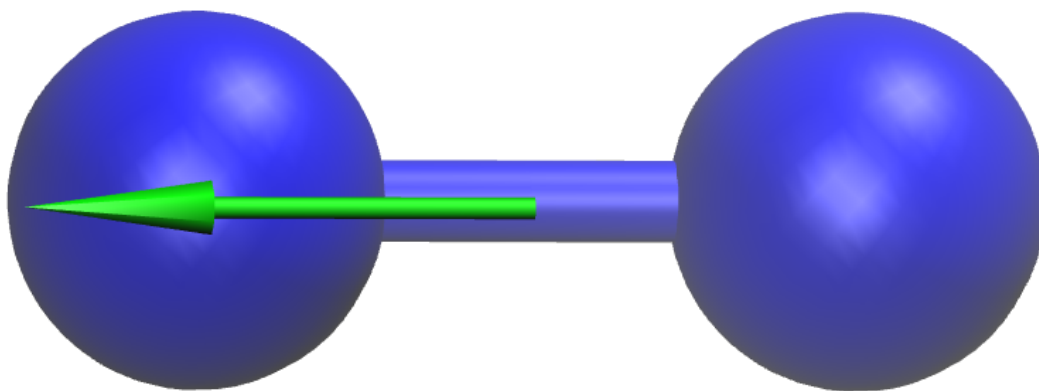
## 6.3.2 Charge Analysis of 1-methyl-thymine

TI-DFTB was used to optimize the ES energy of 1-methyl-thymine so that the transition dipole moment (TDM) could be analyzed. This molecule was chosen due to a recent study by Kistler et al.[121] which decomposed this molecules atom centered Mulliken population of transition charge from the total transition density. The natural product of the TI-DFTB TDM routine results in atom centered Mulliken populations that are subsequently summed in order to calculate the TDM, therefore this was an excellent reference to compare early coding efforts against, as shown in Figure 6.6.
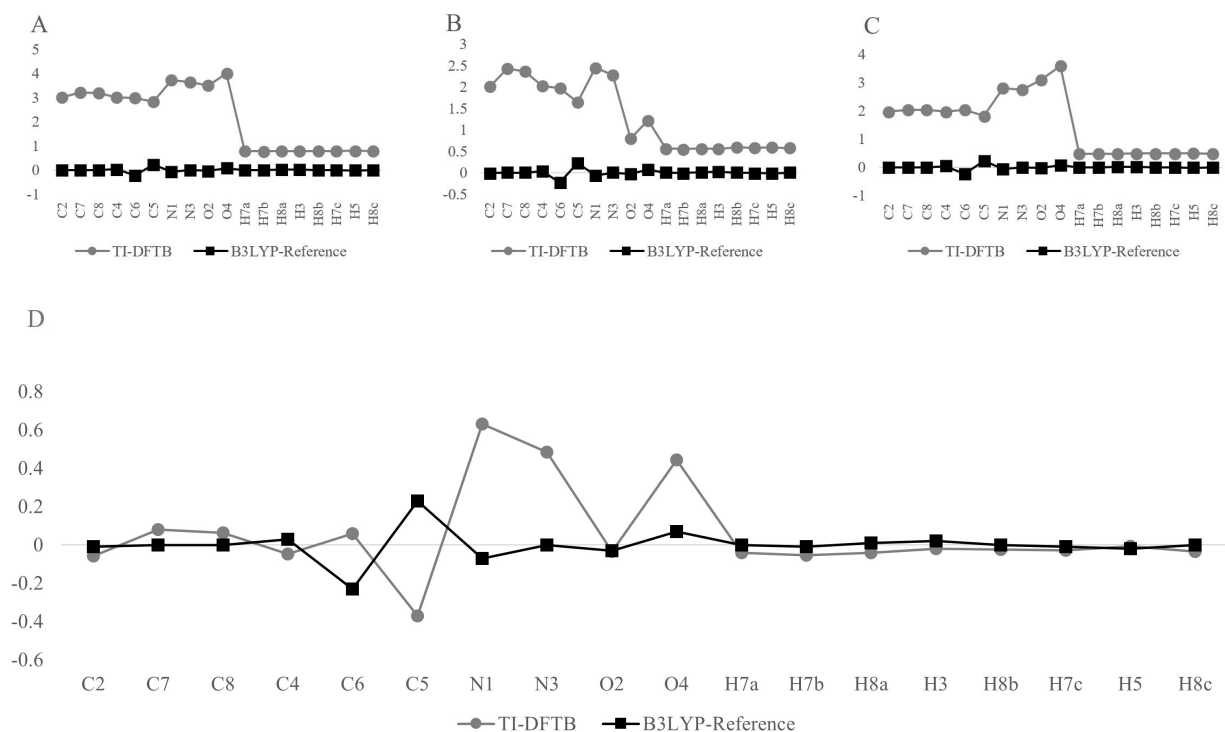


**Figure 6.6** Total atom centered transition charges calculated by TD-DFT using the B3LYP functional in [121] compared to transition charges calculated with TI-DFTB for four different charge mixing schemes. A.) UD density and $\alpha$ channel, B.) UD density with $\alpha$ and $\beta$ contributions, C.) QM density with $\alpha$ channel, D.) QM density with $\alpha$ and $\beta$ contributions.

Using data similar to what is represented in Table 6.4, 1-methyl-thymine was used to test a few charge mixing schemes for the ultimate TDM summation shown in Listing 5.1. There

was some ambiguity as to the form of the sparse density matrix during TDM calculation, namely whether the variable should be in a charge/magnetization (QM) or in a spin-up/spin-down (UD) form during the summation. The general concept represented by the two columns that form the sparse density matrix have been referred to thus far as the $\alpha$- and $\beta$-channel, which evokes a UD framework with its connotation. However, it was discovered that the ground state dipole moment calculation in DFTB+ only used the previously termed $\alpha$-channel in the summation. This is nonsensical given the general notion of dual-spin systems.

The total atom centered transition charges were amassed for 1-methyl-thymine using the sparse transition density in both a QM and UD form (as the variable was altered easily using a local subroutine to DFTB+ called $qm2ud()$). It was then tested whether both the $\alpha$ and $\beta$ spin-channels should be used. Figure 6.6A shows the total charges from a UD density using only the $\alpha$-channel, Figure 6.6B shows the same but with a summation of both $\alpha$ and $\beta$ contributions. Figure 6.6C uses a QM density form, but only calculates a TDM with values from the $\alpha$ spin-channel. Figure 6.6A-C are all clearly different than the literature values for 1-methyl-thymine atom centered transition charges. The final programming form was decided upon with creation of Figure 6.6D which used a QM transition density and both spin-channels.

### 6.3.3  TDM Benchmarking for Small Molecule Test Set

A benchmarking of TDM calculated using the wave function (WF) approach EOM-CCSD (section 2.3.2) as a reference, and TD-DFT with differing functionals across Jacob's ladder (subsection 3.1.1) were used as a comparison for the cost and accuracy of TI-DFTB TDM. The molecules used in this benchmarking were pulled from a test set used by Martin Head-Gordon,[122] and selected based on the stipulation that they contain only C, N, O and H atoms. This is simply for ease of comparison to TI-DFTB as the *mio-1-1* Slater-Koster files have been used in all other DFTB calculations for this work. The geometries provided by the Head-Gordon group were determined experimentally, and no geometry optimizations were performed on them. This set was honed based upon which calculations had converged for EOM-CCSD and TD-DFT attempts, as well as what had converged for TI-DFTB. From this a test set of 20 small molecules remained, and the data from a subsection of this list for 10 small molecules is accounted for below.

Each higher level calculation was performed with the cc-pVQZ basis and a def2/J auxilliary basis set where appropriate. This basis was chosen to be reasonably descriptive and compatible with both TD-DFT and WF calculations like EOM-CCSD.

The functionals for the TD-DFT calculations were chosen to represent each rung on Jacob's ladder. The first rung, or local functionals, is represented with PWLDA and the second rung, or generalized gradient approach (GGA) type, with PBE and B97-D. The third rung is comprised of meta-GGAs that include a kinetic energy piece, and are represented with with the functional TPSS. The fourth rung begins to consider exact Hartree-Fock (HF) exchange correlation and are termed hybrid functionals. This class is represented with B3LYP and PBE0. The fifth rung consists of virtual orbital dependant functionals that tout improved accuracy for transition states. This was represented with B2PLYP. $\omega$-B97X was used to represent the range-separated class of functionals which include a long-range HF exchange and short range DFT type exchange.

The EOM-CCSD calculations were performed in QChem 5.0 probing for singlet excitations.[123,124] The TD-DFT calculations in QChem 5.0 were set to define 8 excited states, and the associated TDM were selected by the lowest energy transition with a non-zero oscillator strength. TI-DFTB calculations were performed calling for ground-guess, spin-purified ΔDFTB and TI-TDM for single point energy optimizations. MOM was used in circumstances where the SCC energy did not converge in under 100 iterations. EOM-CCSD values were used as a standard against which the other methods were evaluated.

**Relative Error in Magnitude**

TDM from EOM-CCSD, TD-DFT and TI-DFTB were calculated and compiled in terms of Cartesian coordinates in a.u. from which magnitudes were calculated. The magnitudes ($|\vec{r}|$) of 10 small molecule TDM from TD-DFT and TI-DFTB were compared to to the values calculated by EOM-CCSD to find the absolute relative error (ARE) according to;
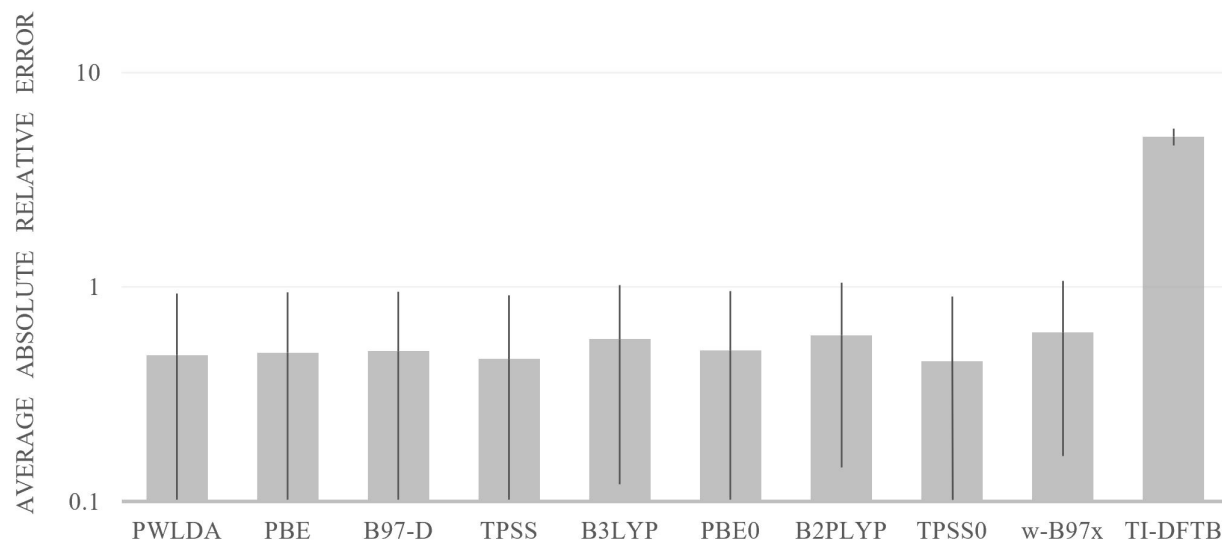


**Figure 6.7** Absolute relative error of single point TDM of small molecule calculations for TD-DFT and TI-DFTB according to Equation 6.10. Logarithmic scale to show orders of magnitude in difference between methods.

$$\left| \frac{|\vec{r}|_{\text{method}} - |\vec{r}|_{\text{EOM-CCSD}}}{|\vec{r}|_{\text{EOM-CCSD}}} \right| \quad\quad\quad (6.10)$$

As shown in Figure 6.7 there was not a strong correlation between higher level functional and minimization of ARE, nor was there a strong tendency to decrease the standard deviation of these calculated errors. In this way, we can suppose that higher level functional do not improve accuracy compared to EOM-CCSD, nor do they improve precision for this test set. The ARE for the TD-DFT calculations hover near 0.5, meaning that these predicted values were often 50% larger than the EOM-CCSD TDM. TI-DFTB calculations had a higher error, averaging near 5 (or 500% larger than the EOM-CCSD values).

It was not hypothesised that all TD-DFT calculations could be considered to have the same ARE compared to EOM-CCSD regardless of functional, but the data here supports that statement. If one can generalize that TD-DFT calculations have an ARE of 0.5, then we can say with the same certainty that TI-DFTB calculations are one order of magnitude less accurate than TD-DFT calculations with an ARE of 5 when compared to EOM-CCSD.

**Directionality of Predicted TDM**

The Cartesian coordinates of predicted TDM vectors were recorded for TD-DFT and TI-DFTB and compared to values calculated with EOM-CCSD. The direction of a TDM vector indicates the spatial location of the transition electron density for TD-DFT, and transition charge density in the case of TI-DFTB. Due to the many approximations in DFTB with regards to representing the electronic density of the system, it was hypothesised that this test is where TI-DFTB would perform the most poorly, and non-normative results were expected as a result.

As shown in Figure 6.8 there was only a small percentage of most methods to predict TDM vectors that pointed the same direction as the EOM-CCSD TDM. The most successful methods in this regard were PWLDA and PBE0, while B3LYP had the worst performance
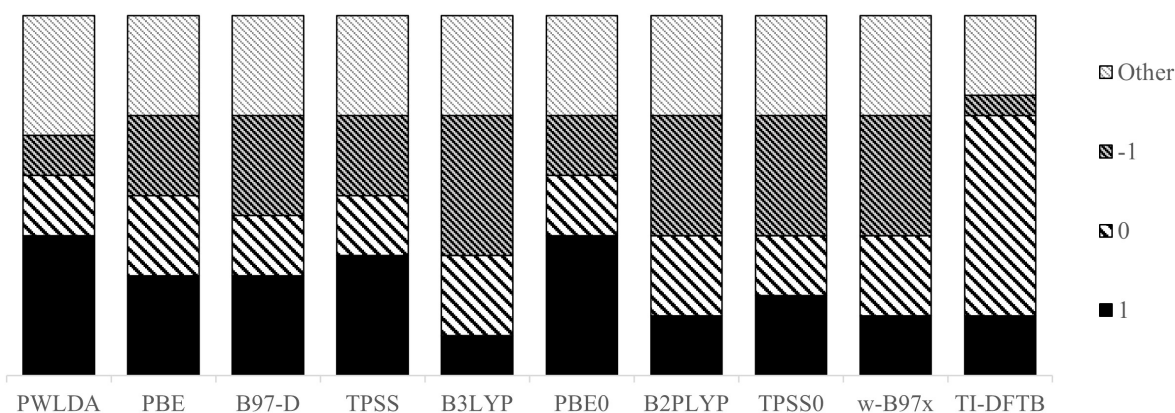
**Figure 6.8** The distribution of normalized dot products between predicted TDM from TD-DFT calculations and TI-DFTB calculations with EOM-CCSD predictions. A normalized dot product of one indicates perfect continuity of direction between the method and EOM-CCSD, zero indicates an orthogonal prediction, and negative one indicates a vector that points in the exact opposite direction. All results labeled "other" were some value between one and negative one that was non-zero.

in this study. TI-DFTB has the same fidelity in direction as B2PLYP and $\omega$B97x compared to EOM-CCSD.

The TDM with non-zero normalized dot products between one and negative one remained fairly consistent across all methods, with TI-DFTB reporting the fewest non-normative values. TI-DFTB also reported the fewest instances of a normalized dot product of negative one, where the TDM vector points in the exact opposite direction as the TDM predicted by EOM-CCSD. TI-DFTB had primarily orthogonal predictions compared to EOM-CCSD TDM.

**Average Calculation Run Time for Methods**

If the continuity of ARE between DFT functionals was surprising, the differentiation of TD-DFT calculations based on increasing functional complexity was found in the computational cost of these calculations. As observed in Figure 6.9, the functionals proportionally ascend in average run times for single point TDM calculations of molecules composed of less than
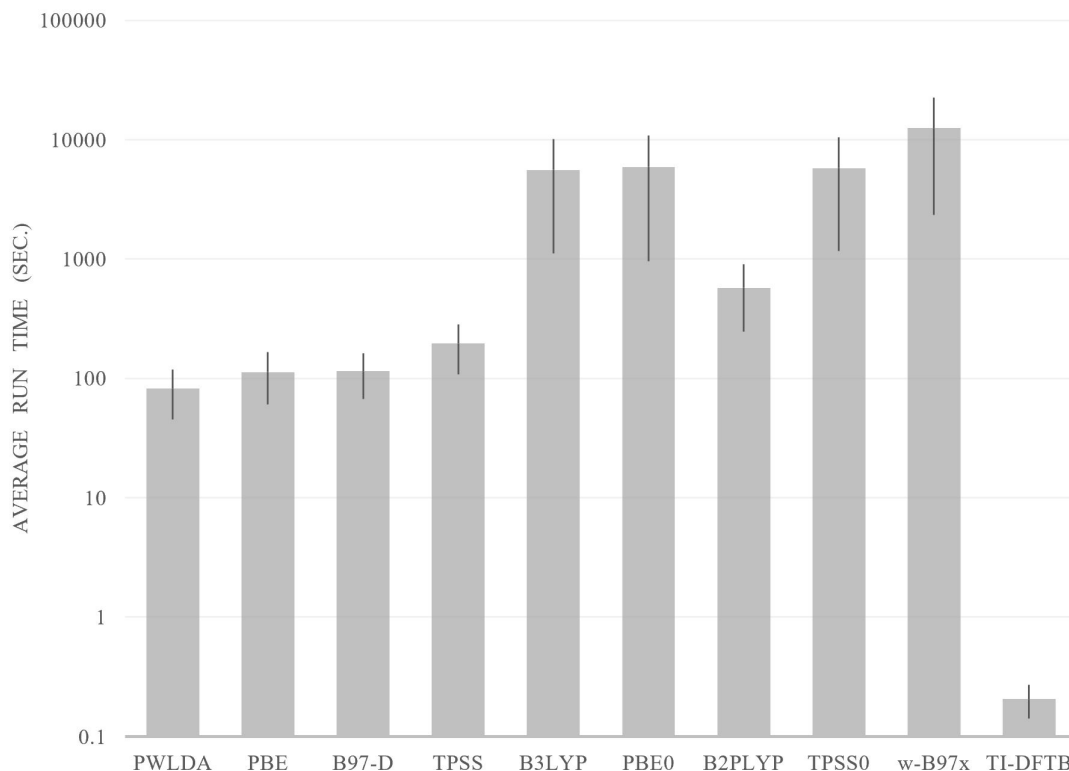
**Figure 6.9** The average run-time of single-point TDM calculations of small molecules for TD-DFT functionals and TI-DFTB. Logarithmic scale to show orders of magnitude in difference between computational speeds.

five atoms for increasing functional complexity. The calculation that ran for a little under two minutes for PWLDA would take nearly three hours using $\omega$-B97x. For these same calculations, TI-DFTB would take a fraction of a second.

If TI-DFTB is one order of magnitude less accurate than all TD-DFT calculations, it is conservatively between three and five orders of magnitude faster. When discussing computational cost it is implied that with any method there will be a certain amount of uncertainty and error compared to experimental data, and so there is always a balancing act between what is feasible and what is the most correct. For small molecules it would not necessarily be in ones best interest to use TI-DFTB as the error is large enough to verge on not useful, however one could say similar things about TD-DFT based on the error calculated there. Where TI-DFTB TDM are useful is when the system is large, and neither TD-DFT nor EOM-CCSD calculations are necessarily feasible. The next case study will explore this idea using acridinium salts.

## 6.3.4   TDM of Acridinium Salts by TD-DFT and TI-DFTB

The ground and excited electronic states resulting from a $\Delta$DFTB calculation are made mutually orthogonal by a corresponding orbital transformation, thereby allowing calculation of transition properties like the transition dipole moment (TDM). This allows for prediction of spectral peak intensity which can be used to derive energy transfer rates for even large photoactive systems.[90,93] Acridinium salts have previously been toted as organic alternatives to precious-metal photoredox catalysts, allowing for comparable excited state lifetimes and attenuated redox potentials within a sustainable framework. Using a time-independent DFTB (TI-DFTB) platform a subset of this class of molecules can be characterized in the ground- and excited-states to infer photophysical information, bolstering the working knowledge of these compounds and benchmarking the proposed method.

The TDM of the six acridinium salts from subsection 6.2.2 were calculated using TD-DFT and TI-DFTB. There was no EOM-CCSD data for this set, as there was not a time period of several months in the budget for this type of calculation. Figure 6.10 shows the average run times for the calculations that converged in under 90 days, and lists for each functional the converged structures associated with it.

The numerical results of this study can be found in Table 6.5, where the average TDM from TD-DFT is compared to the TDM calculated with TI-DFTB and TI-DFTB with MOM. When looking at Table 6.5 it is perhaps useful to notice that for structure E there were five functionals that could not be factored into the standard deviation of the mean TDM, which might explain its precision in average calculated TDM. Notice too that the functional B2PLYP had only calculated one half of the structures' TDM in the allotted time frame, so the relatively low average run time is the result of not including this data in Figure 6.10. TI-DFTB and MOM show run times that are four to six orders of magnitude faster than TD-DFT - so where functionals like TPSS0 took on average 41 days, TI-DFTB performed the same calculation in fewer than 10 seconds.
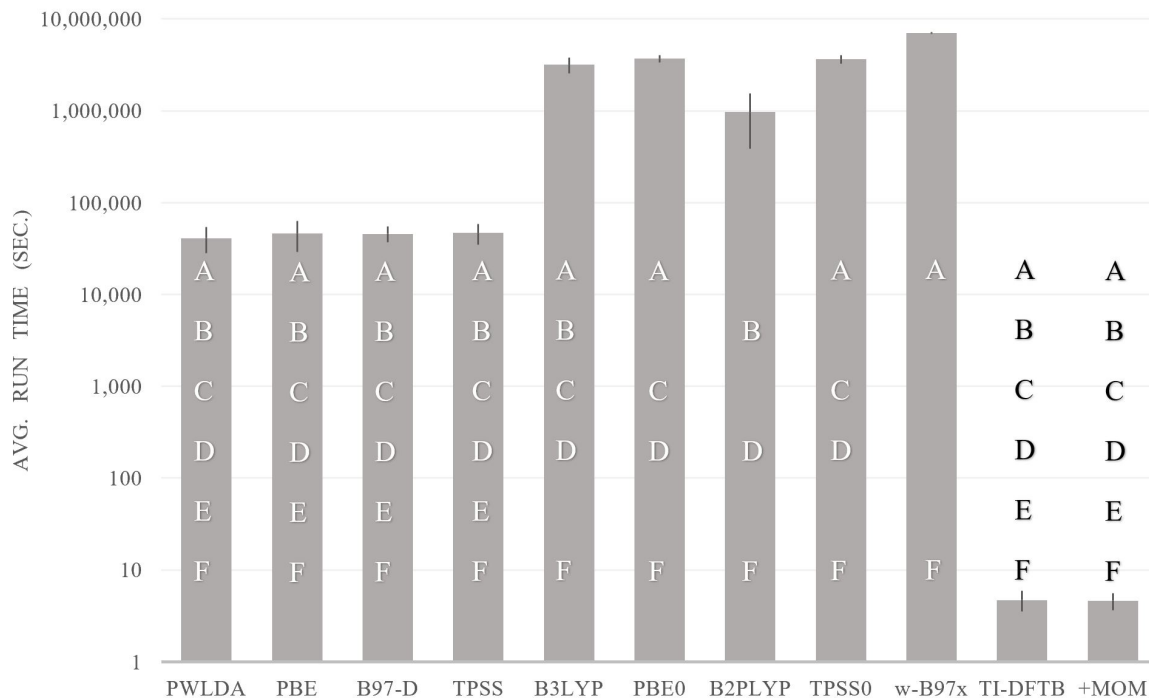
**Figure 6.10** The average run-time of single-point TDM calculations of acridinium salts for TD-DFT functionals and TI-DFTB. Logarithmic scale to show orders of magnitude in difference between computational speeds. Calculations were allowed to run for 90 days, A-E correspond to acridinium salts as described in Table 6.5 that converged in that amount of time.

From the results for structure A, C, D and E, one can see differences in predicted TDM with and without MOM, which is to be expected as the MO spaces of MOM calculations are different than those defined by TI-DFTB alone. Using MOM can allow you to calculate transitions between the HOMO and a virtual orbital that is not the LUMO of the system, which is one explanation of the difference in results from these MOM calculations compared to TD-DFT. It is a shortcoming of MOM that the user cannot tell if this is the case when calculating a TDM, therefore MOM is not currently advised for people using the TI-TDM functionality.

The Cartesian coordinates of these predicted TDM were compiled for all methods, and the direction of both TI-DFTB and MOM predicted TDM were compared to each TDM predicted by the TD-DFT functionals. This data is presented in Figure 6.11, though according to the

| | Functional Group | Average TDM From TD-DFT | | | TI-DFT | *SD from mean* | +MOM | *SD from mean* |
|---|---|---|---|---|---|---|---|---|
| A | naphthalene | 3 | ± | 1 | 11.73 | 9 | 10.28 | 7 |
| B | benzene | 1 | ± | 2 | 10.60 | 5 | 10.60 | 5 |
| C | toluene | 4.37 | ± | 0.07 | 9.43 | 72 | 14.43 | 144 |
| D | mesitylene | 2.8 | ± | 0.4 | 10.79 | 20 | 15.80 | 32 |
| E | anthracene | 3.68 | ± | 0.08 | 8.60 | 62 | 33.55 | 311 |
| F | xylene | 1.2 | ± | 0.2 | 6.51 | 26 | 6.51 | 26 |

**Table 6.5** Magnitudes of calculated TDM from TD-DFT and TI-DFTB with and without MOM. TD-DFT TDM magnitudes were averaged across the nine functionals from Figure 6.11 that were able to complete the calculation in less than 90 days. A reference for which structures converged in the 90 days can be found in Figure 6.10.
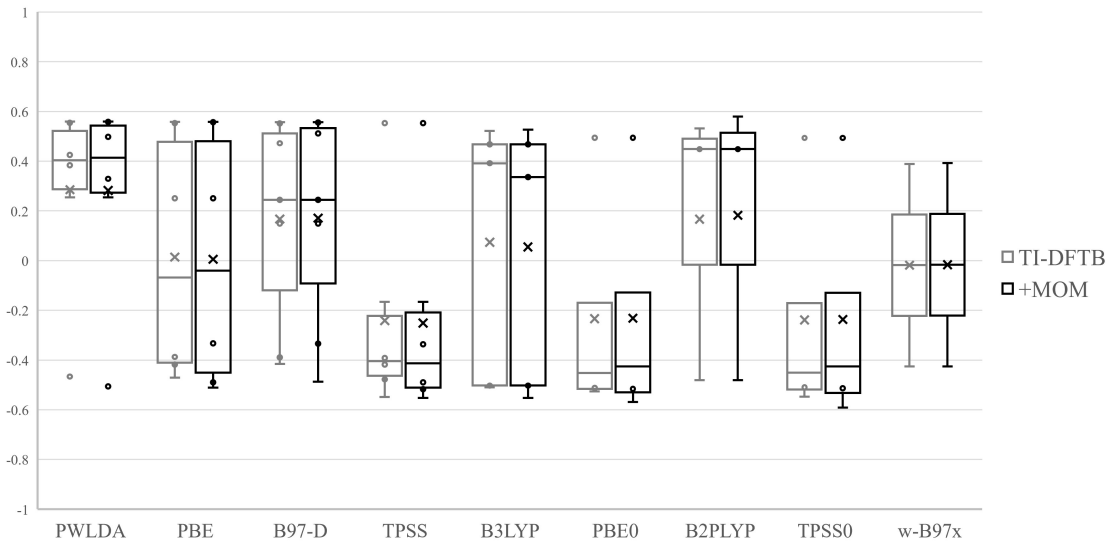


**Figure 6.11** Box and whisker plots showing the normalized dot products of TI-DFTB and MOM TDM with each TD-DFT value. These values are grouped by TD-DFT functional for both TI-DFTB and MOM data sets. These plots represent the inclusive median of these values, and the mean is indicated by an **x** for each comparison. All data points are represented.

data in Figure 6.8 values near one are not necessarily to be trusted.

The accuracy of TI-DFTB calculated TDM may raise some questions as to the use of such a method if the values are so different than what is predicted by more expensive methods. As TI-DFTB inherits all of the approximations of the parent method DFTB, we predict a certain amount of systematic error in our calculations. This can be investigated in the future by attempting to create better basis sets for the method, or replicating these results in DFTB3, the third-order Taylor expansion of the DFTB energy. As this method stands presented in this work there is the possibility of ranking potential target molecules based on the approximate TDM, using these values to spot trends and speculate as to the optimal functionalization of the target. As this method is not inherently high resolution, and is useful primarily in high-throughput molecular screening, this possibility to see trends at such a low cost is precisely the outcome we hoped to produce. The accuracy of this trend prediction falls under future work for this lab, as well as compiling a data set of EOM-CCSD results for acridinium salt TDM so that these comparisons can be made to a standard, and then performing a cost to accuracy analysis of TI-DFTB.

# Chapter Seven

# CONCLUDING REMARKS

We have developed a time-independent excited state method within the electronic structure package, DFTB+. TI-DFTB as implemented in DFTB+ 19.1 consists of $\Delta$DFTB for non-Aufbau electronic orbital populations to probe time-independent excited states, maximum overlap method options that aid in energy convergence, and the corresponding orbital transformation to probe transition dipole moments. These methods have been preliminary tested and show good agreement between algorithmic behavior and mathematical formalism. $\Delta$DFTB has been updated and shows clean and predictable convergence behavior, as evidenced by the gradient analysis as well as geometry optimizations of several organic molecules. The maximum overlap methods have proven useful tools for evaluating the excited states of conjugated molecules, systems which can often be plagued with variational collapse. The corresponding orbital transformation has been given a strong mathematical foundation, and proof. As it is implemented in DFTB, the corresponding orbital transformation shows early success as a rapid transition dipole moment method.

$\Delta$DFTB in DFTB+ 19.1 has been merged upstream with the master branch of the DFTB+ repository. Successful merging of $\Delta$DFTB with the publicly available DFTB+ codebase occurred on October 23, 2020. The $\Delta$DFTB method developed by this lab will be included in the publicly available DFTB+ 20.2 electronic structure package which is to be released by the end of 2020.

# REFERENCES

(1) Ledley, T. S.; Sundquist, E. T.; Schwartz, S. E.; Hall, D. K.; Fellows, J. D.; Killeen, T. L. *Eos, Transactions American Geophysical Union* **1999**, *80*, 453–458.

(2) Skjærseth, J. B.; Skodvin, T Climate change and the oil industry: Common problem, varying strategies, \url{manchesteropenhive.com}, 2018.

(3) Nerem, R. S.; Beckley, B. D.; Fasullo, J. T.; Hamlington, B. D.; Masters, D; Mitchum, G. T. *Proceedings of the National Academy of Sciences* **2018**, *115*, 2022–2025.

(4) Poole, J. A.; Barnes, C. S.; Demain, J. G.; Bernstein, J. A.; Padukudru, M. A.; Sheehan, W; Guidos, G; Wedner, J; Codina, R; Levetin, E; Cohn, J. R. *Journal of Allergy and Clinical Immunology* **2019**.

(5) Nolan, C; Overpeck, J. T.; Allen, J. R.; Anderson, P. M.; Betancourt, J. L.; Binney, H. A.; Brewer, S; Bush, M. B.; Chase, B. M.; Cheddadi, R; Djamali, M *Science* **2018**, *361*, 920–923.

(6) Xu, J.; Grumbine, R. E.; Shrestha, A.; Eriksson, M.; Yang, X.; Wang, Y.; Wilkes, A. *Conservation Biology* **2009**, *23*, 520–530.

(7) Rosenzweig, C.; Iglesias, A.; Yang, X.; Epstein, P. R.; Chivian, E. *Global Change and Human Health* **2001**, *2*, 90–104.

(8) Flannigan, M. D.; Amiro, B. D.; Logan, K. A.; Stocks, B. J.; Wotton, B. M. *Mitigation and Adaptation Strategies for Global Change* **2006**, *11*, 847–859.

(9) Hall, C. M. et al. *Tourism Management* **2015**, DOI: 10.1016/j.tourman.2014.08.009.

(10) Howlett, M. *Global Environmental Change* **2014**, *29*, 395–403.

(11) Quaschning, V. V., *Renewable energy and climate change*; John Wiley & Sons: 2019.

(12) Janssen, R. A.; Nelson, J. *Advanced Materials* **2013**, *25*, 1847–1858.

(13) Br/'edas, J. L.; Norton, J. E.; Cornil, J; Coropceanu, V *Accounts of Chemical Research* **2009**, *42*, 1691–1699.

(14) Xu, J et al. *Nature Nanotechnology* **2018**, *13*, 456.

(15) De Brito, M. A.; Sampaio, L. P.; Junior, L. G.; Canesin, C. A. *COBEP 2011 - 11th Brazilian Power Electronics Conference* **2011**, 531–537.

(16) Lizin, S.; Van Passel, S.; De Schepper, E.; Maes, W.; Lutsen, L.; Manca, J.; Vanderzande, D. *Energy and Environmental Science* **2013**, *6*, 3136–3149.

(17) Mazzio, K. A.; Luscombe, C. K. *Chemical Society Reviews* **2015**, *44*, 78–90.

(18) Munir, S.; Begum, M. *Asian Journal of Green Chemistry* **2019**, *3*, 91–102.

(19) Wahadoszamen, M; Margalit, I; Ara, A. M.; van Grondelle, R; Noy, D *Nature Communications* **2014**, *5*, 5287.

(20) Ganesh, I *Renewable Sustainable Energy Review* **2014**, *44*, 904–932.

(21) Sun C., W. C. B. R. *ChemPhotoChem* **2019**, *3*, DOI: 10.1002/cptc.201900030.

(22) Barnham, K. W. J.; Duggan, G *Journal of Applied Physics* **1990**, *67*, 3490–3493.

(23) Karani, A; Yang, L; Bai, S; Futscher, M. H.; Snaith, H. J.; Ehrler, B; Greenham, N. C.; Di, D *ACS Energy Letters* **2018**, *3*, 869–874.

(24) Shi, X. Computational Study Of Transition Metal Complexes For Solar Energy Conversion And Molecular Interaction With Strong Laser Fields, 2018.

(25) Krylov, A. I.; Gill, P. M *Wiley Interdisciplinary Reviews: Computational Molecular Science* **2012**, *2012*, 317–316.

(26) Hachmann, J.; Olivares-Amaya, R.; Atahan-Evrenk, S.; Amador-Bedolla, C.; Sánchez-Carrera, R. S.; Gold-Parker, A.; Vogt, L.; Brockway, A. M.; Aspuru-Guzik, A. *Journl of Physical Chemistry Letters* **2011**, *2*, 2241–2251.

(27) Liu, Y; Grossman, J. C. *Nano Letters* **2014**, *14*, 7046–7050.

(28) Gong, S.; Xie, T.; Zhu, T.; Wang, S.; Fadel, E. R.; Li, Y.; Grossman, J. C. *Physical Review B* **2019**, *100*, 1–9.

(29) Kowalczyk, T.; Lin, Z.; Van Voorhis, T. *Journal of Physical Chemistry A* **2010**, *114*, 10427–10434.

(30) Herbert, J. M.; Zhang, X; Morrison, A. F.; Liu, J *Accounts of Chemical Research* **2016**, *49*, 931–941.

(31) Saini, P.; Banerjee, M.; Chattopadhyay, A. *Journal of Physical Chemistry A* **2016**, *120*, 396–406.

(32) Thom, A. J.; Head-Gordon, M. *Journal of Chemical Physics* **2009**, *131*, 1–6.

(33)  Korovyanko, O. J.; Österbacka, R.; Jiang, X. M.; Vardeny, Z. V.; Janssen, R. A. *Physical Review B - Condensed Matter and Materials Physics* **2001**, *64*, 2351221–2351226.

(34)  Aradi, B; Hourahine, B; Frauenheim, T *The Journal of Physical Chemistry A* **2007**, *111*, 5678–5684.

(35)  Bodrog, Z; Aradi, B *physica status solidi* **2012**, *249*, 259–269.

(36)  Aradi, B.; Hourahine, B.; et al. DFTB+, github.com/dftbplus, 2020.

(37)  Kowalczyk, T.; Yost, S. R.; Voorhis, T. V. *The Journal of Chemical Physics* **2011**, *134*, 54128.

(38)  Kowalczyk, T.; Le, K.; Irle, S. *Journal of Chemical Theory and Computation* **2015**, *12*, 313–323.

(39)  Szabo, A.; Ostlund, N. S., *Modern quantum chemistry: introduction to advanced electronic structure theory*; Courier Corporation: 2012.

(40)  Garavelli, M.; Bernardi, F.; Cembran, A.; Castaño, O.; Frutos, L. M.; Merchán, M.; Olivucci, M. *Journal of the American Chemical Society* **2002**, *124*, 13770–13789.

(41)  Slater, J. C. *Physical Review (2)* **1929**, *34*, 1293–1322.

(42)  Echenique, P.; Alonso, J. L. *Molecular Physics* **2007**, *105*, 3057–3098.

(43)  Deng, J.; Gilbert, A. T.; Gill, P. M. *Physical Chemistry Chemical Physics* **2010**, *12*, 10759–10765.

(44)  Crawford, T. D.; Schaefer III, H. F. In *Reviews in Computational Chemistry*; John Wiley Sons, Ltd: 2000, pp 33–136.

(45)  Fihey, A.; Jacquemin, D. *Journal of Chemical Theory and Computation* **2019**, *15*, 6267–6276.

(46)  Wolfsberg, M.; Helmholz, L. *The Journal of Chemical Physics* **1952**, *20*, 837–843.

(47)  Burke, K. *Journal of Chemical Physics* **2012**, *136*, DOI: 10.1063/1.4704546.

(48)  Pribram-Jones, A.; Gross, D. A.; Burke, K. *Annual Review of Physical Chemistry* **2015**, *66*, PMID: 25830374, 283–304.

(49)  Amusia, M. Y.; Msezane, A. Z.; Shaginyan, V. R. *Physica Scripta* **2003**, *68*, C133–C140.

(50)  McArdle, S.; Endo, S.; Aspuru-Guzik, A.; Benjamin, S. C.; Yuan, X. *Reviews of Modern Physics* **2020**, *92*, 15003.

(51)  Smith, C. D.; Karton, A. *Journal of Computational Chemistry* **2020**, *41*, 328–339.

(52)  Koopmans, T *Physica* **1934**, *1*, 104 –113.

(53)  Yang, K.; Peverati, R.; Truhlar, D. G.; Valero, R. *Journal of Chemical Physics* **2011**, *135*, DOI: 10.1063/1.3607312.

(54)  Song, J.-W.; Yamashita, K.; Hirao, K. *The Journal of Chemical Physics* **2011**, *135*, 071103.

(55)  Zhao, Y.; Truhlar, D. G. *The Journal of Physical Chemistry A* **2004**, *108*, 6908–6918.

(56)  Korth, M.; Grimme, S. *Journal of Chemical Theory and Computation* **2009**, *5*, 993–1003.

(57)  Gerber, I. C.; Ángyán, J. G. *Chemical Physics Letters* **2005**, *415*, 100–105.

(58)  Rohrdanz, M. A.; Martins, K. M.; Herbert, J. M. *Journal of Chemical Physics* **2009**, *130*, DOI: 10.1063/1.3073302.

(59)  Zhang, Z.; Si, Y.; Sun, G. *ACS Sustainable Chemistry and Engineering* **2019**, *7*, 18493–18504.

(60)  Escudero, D.; Jacquemin, D. *Dalton Transactions* **2015**, *44*, 8346–8355.

(61)  Domratcheva, T.; Hartmann, E.; Schlichting, I.; Kottke, T. *Scientific Reports* **2016**, *6*, 1–14.

(62)  Cheung, P. M.; Burns, K. T.; Kwon, Y. M.; Deshaye, M. Y.; Aguayo, K. J.; Oswald, V. F.; Seda, T.; Zakharov, L. N.; Kowalczyk, T.; Gilbertson, J. D. *Journal of the American Chemical Society* **2018**, *140*, 17040–17050.

(63)  Ramos, P.; Pavanello, M. *Journal of Chemical Theory and Computation* **2014**, *10*, 2546–2556.

(64)  Li, W.; Kotsis, K.; Manzhos, S. *Physical Chemistry Chemical Physics* **2016**, *18*, 19902–19917.

(65)  Hourahine, B. et al. *Journal of Chemical Physics* **2020**, *152*, DOI: 10.1063/1.5143190.

(66)  Elstner, M.; Seifert, G. *Philosophical Transactions of the Royal Society A: Mathematical, Physical and Engineering Sciences* **2014**, *372*, DOI: 10.1098/rsta.2012.0483.

(67)  Spiegelman, F.; Tarrat, N.; Cuny, J.; Dontot, L.; Posenitskiy, E.; Martí, C.; Simon, A.; Rapacioli, M. Density-functional tight-binding: basic concepts and applications to molecules and clusters, 2020.

(68)  Frauenheim, T.; Seifert, G; Elsterner, M; Hajnal, Z; Jungnickel, G; Porezag, D; Suhai, S; Scholz, R *physica status solidi* **2000**, *217*, 41–62.

129

(69) Majid, A.; Munir, M.; Khan, S. U. D.; Almutairi, Z. *Journal of Electronic Materials* **2020**, *49*, 3659–3667.

(70) Piskorz, W.; Zasada, F.; Wójtowicz, G.; Morawski, A.; Macyk, W.; Sojka, Z. *Journal of Physics Condensed Matter* **2019**, *31*, DOI: 10.1088/1361-648X/ab2bc8.

(71) Müller, M; Binder, K; Trautmann ; Forschungszentrum, A; Gmbh, J., *John von Neumann Institute for Computing (NIC), Schriften des Forschungszentrums Jülich*; Vol. 50, p 75.

(72) Timsorn, K.; Wongchoosuk, C. *Materials Research Express* **2020**, *7*, 055005.

(73) Sanachai, K.; Mahalapbutr, P.; Choowongkomon, K.; Poo-Arporn, R. P.; Wolschann, P.; Rungrotmongkol, T. *ACS Omega* **2020**, *5*, 369–377.

(74) Bold, B. M.; Sokolov, M.; Maity, S.; Wanko, M.; Dohmen, P. M.; Kranz, J. J.; Kleinekathöfer, U.; Höfener, S.; Elstner, M. *Physical Chemistry Chemical Physics* **2020**, DOI: 10.1039/c9cp05753f.

(75) Luo, M.; Yu, Y.; Jin, Z.; Dong, H.; Li, Y. *Applied Surface Science* **2020**, *517*, DOI: 10.1016/j.apsusc.2020.146181.

(76) Bold, B. M. Spectroscopic Properties of Light-Activated Proteins Resolved by Multiscale-Simulations, PhD Thesis, Karlsruhe Institute of Technology: Eggenstein-Leopoldshafen, 2019.

(77) Tyler, B. The Atomic and Electronic Structure and Tunability of Ruddlesden-Popper Phases for Photovoltaic Applications, Master's Thesis, Western Washington University: Bellingham, Washington, 2019.

(78) Manzhos, S. *Molecules* **2020**, *25*, DOI: 10.3390/molecules25092233.

(79) Uratani, H.; Nakai, H. *The Journal of Physical Chemistry Letters* **2020**, DOI: 10.1021/acs.jpclett.0c01028.

(80) Komoto, N.; Yoshikawa, T.; Nishimura, Y.; Nakai, H. *Journal of Chemical Theory and Computation* **2020**, *16*, 2369–2378.

(81) Seth, M.; Ziegler, T. *The Journal of Chemical Physics* **2005**, *123*, 144105.

(82) Harris, R. A.; Mathies, R; Myers, A *Chemical Physics Letters* **1983**, *94*, 327–330.

(83) Evangelista, F. A.; Shushkov, P; Tully, J. C. *Journal of Physical Chemistry A* **2013**, *117*, 7378–7892.

(84) Ziegler, T; Rauk, A; Baerends, E. J. *Theoretical Chemistry Accounts* **1977**, *43*, 261–271.

(85)     Ziegler, T.; Krykunov, M.; Cullen, J. *Journal of Chemical Physics* **2012**, *136*, DOI: 10.1063/1.3696967.

(86)     Gaus, M.; Cui, Q.; Elstner, M. *Journal of Chemical Theory and Computation* **2011**, *7*, 931–948.

(87)     Gilbert, A. T.; Besley, N. A.; Gill, P. M. *Journal of Physical Chemistry A* **2008**, *112*, 13164–13171.

(88)     Besley, N. A.; Gilbert, A. T.; Gill, P. M. *Journal of Chemical Physics* **2009**, *130*, DOI: 10.1063/1.3092928.

(89)     Barca, G. M.; Gilbert, A. T.; Gill, P. M. *Journal of Chemical Theory and Computation* **2018**, *14*, 1501–1509.

(90)     Petit, A. S.; Subotnik, J. E. *The Journal of Chemical Physics* **2014**, *141*, 014107(14).

(91)     Baym, G.; Beck, D. H. *Proceedings of the National Academy of Sciences of the United States of America* **2016**, *113*, 7438–7442.

(92)     Caricato, M.; Trucks, G. W.; Frisch, M. J.; Wiberg, K. B. *J. Chem. Theory Comput.* **2010**, *7*, 456–466.

(93)     Karaveli, S.; Zia, R. *Physical Review Letters* **2011**, *106*, 193004(4).

(94)     Davies, R. W.; Tipping, R. H.; Clough, S. A. *Physical Review A* **1982**, *26*, 3378–3394.

(95)     Shao, Y. *Physical Chemistry Chemical Physics* **2006**, *8*, 3172 –3191.

(96)     Zhang, Y.; Xu, G., *Encyclopedia of Database Systems*, 2016; Chapter : Singular Value Decomposition, pp 1–3.

(97)     Brunton, S. L.; Kutz, J. N. *Data-Driven Science and Engineering* **2019**, 3–46.

(98)     Zaiontz, C. Singular Value Decomposition, 2015, (accessed: 04.28.2020).

(99)     Lay, D. C., *Linear Algebra and Its Applications*, 3rd ed.; Pearson Education, Inc.: 2003, pp 474–481/492.

(100)    Department of Mathematics, O. S. U. Eigenvalues and Eigenvectors (accessed: 04.28.2020).

(101)    Szabo, F. E., *Unitary Matrix Ensables*, 1st ed.; Academic Press: 2015, pp 385–392/438.

(102)    Amos, A. T.; Hall, G. G. *Proceedings of the Royal Society of London. Series A. Mathematical and Physical Sciences* **1961**, *263*, 483–493.

(103)    Broer, R. *International Journal of Quantum Chemistry* **1993**, *45*, 587–590.

(104)    Masip, J.; Rubio, J.; Illias, F. *Chemical Physics Letters* **1985**, *120*, 513–516.

(105)  Neese, F. *Journal of Physics and Chemistry of Solids* **2004**, *65*, 781–785.

(106)  Burton, H. G.; Thom, A. J. *Journal of Chemical Theory and Computation* **2016**, *12*, 167–173.

(107)  Martin, R. L. *Journal of Chemical Physics* **2003**, *118*, 4775–4777.

(108)  Morrison, A. F.; You, Z. Q.; Herbert, J. M. *Journal of Chemical Theory and Computation* **2014**, *10*, 5366–5376.

(109)  Jensen, K. T.; Benson, R. L.; Cardamone, S.; Thom, A. J. *Journal of Chemical Theory and Computation* **2018**, *14*, 4629–4639.

(110)  Dupuis, M.; Nallapu, M. *Journal of Computational Chemistry* **2019**, *40*, 39–50.

(111)  King, H. F.; Stanton, R. E.; Kim, H.; Wyatt, R. E.; Parr, R. G. *The Journal of Chemical Physics* **1967**, *47*, 1936–1941.

(112)  Dirac, P., *The Principles of Quantum Mechanics*, Third; Oxford University Press: Clarendon, Oxford UK, 1947, p 248.

(113)  Anderson, E.; Bai, Z.; Bischof, C.; Blackford, S.; Demmel, J.; Dongarra, J.; Du Croz, J.; Greenbaum, A.; Hammarling, S.; McKenney, A.; Sorensen, D., *LAPACK Users' Guide*, Third; Society for Industrial and Applied Mathematics: Philadelphia, PA, 1999.

(114)  Natrajan, A.; Wen, D. *Green Chemistry Letters and Reviews* **2013**, *6*, 237–248.

(115)  Nakazono, M.; Oshikawa, Y.; Nakamura, M.; Kubota, H.; Nanbu, S. *Journal of Organic Chemistry* **2017**, *82*, 2450–2461.

(116)  Komoto, N.; Yoshikawa, T.; Ono, J.; Nishimura, Y.; Nakai, H. *Journal of Chemical Theory and Computation* **2019**, *15*, 1719–1727.

(117)  Rohwedder, T; Schneider, R *Journal of mathematical chemistry* **2011**, *49*, 1889.

(118)  Ionova, I. V.; Carter, E. A. *Journal of computational chemistry* **1996**, *17*, 1836–1847.

(119)  Kamencek, T.; Wieser, S.; Kojima, H.; Bedoya-Martínez, N.; Dürholt, J. P.; Schmid, R.; Zojer, E. *Journal of Chemical Theory and Computation* **2020**, *16*, 2716–2735.

(120)  Posenitskiy, E.; Rapacioli, M.; Lemoine, D.; Spiegelman, F. *Journal of Chemical Physics* **2020**, *152*, DOI: 10.1063/1.5135369.

(121)  Kistler, K. A.; Spano, F. C.; Matsika, S. *The Journal of Physical Chemistry B* **2013**, *117*, PMID: 23391106, 2032–2044.

(122)  Hait, D.; Head-Gordon, M. *Journal of Chemical Theory and Computation* **2018**, *14*, PMID: 29562129, 1969–1981.

(123)   Krylov, A. I.; Gill, P. M. *Wiley Interdisciplinary Reviews: Computational Molecular Science* **2013**, *3*, 317–326.

(124)   Shao, Y. et al. *Molecular Physics* **2015**, *113*, 184–215.